A Study of Compatible Radiating Elements for MMIC / MHMIC Applications

By

David J. Roscoe

A Thesis

Submitted to the Faculty of Graduate Studies

In Partial Fulfillment of the Requirements

for the Degree of Master of Science

University of Manitoba

Department of Electrical Engineering

Winnipeg, Manitoba

Canada

May, 1989

(c) Copyright by David John Roscoe

National Library of Canada
Bibliothèque nationale du Canada

Canadian Theses Service
Service des thèses canadiennes

Ottawa, Canada
K1A 0N4

The author has granted an irrevocable non-exclusive licence allowing the National Library of Canada to reproduce, loan, distribute or sell copies of his/her thesis by any means and in any form or format, making this thesis available to interested persons.

The author retains ownership of the copyright in his/her thesis. Neither the thesis nor substantial extracts from it may be printed or otherwise reproduced without his/her permission.

L'auteur a accordé une licence irrévocable et non exclusive permettant à la Bibliothèque nationale du Canada de reproduire, prêter, distribuer ou vendre des copies de sa thèse de quelque manière et sous quelque forme que ce soit pour mettre des exemplaires de cette thèse à la disposition des personnes intéressées.

L'auteur conserve la propriété du droit d'auteur qui protège sa thèse. Ni la thèse ni des extraits substantiels de celle-ci ne doivent être imprimés ou autrement reproduits sans son autorisation.

ISBN 0-315-54829-0

Canada

A STUDY OF COMPATIBLE RADIATING ELEMENTS FOR MMIC / MHMIC APPLICATIONS

BY

DAVID J. ROSCOE

A thesis submitted to the Faculty of Graduate Studies of the University of Manitoba in partial fulfillment of the requirements of the degree of

MASTER OF SCIENCE

© 1989

Permission has been granted to the LIBRARY OF THE UNIVERSITY OF MANITOBA to lend or sell copies of this thesis, to the NATIONAL LIBRARY OF CANADA to microfilm this thesis and to lend or sell copies of the film, and UNIVERSITY MICROFILMS to publish an abstract of this thesis.

The author reserves other publication rights, and neither the thesis nor extensive extracts from it may be printed or otherwise reproduced without the author's written permission.

Abstract

A study of the problem of devising a suitable radiating element which would be compatible with MMIC / MHMIC technology has been undertaken. The application of the element would be an active phased array antenna.

MMIC / MHMIC technology uses thin substrates with high relative permittivities. These characteristics are suitable for the circuitry but undesirable for radiating elements because they result in narrow input impedance bandwidths. A review of existing techniques to broaden the bandwidth was completed. This showed that the broadest bandwidths were achieved from structures which had stacked radiators or parasitically coupled radiators. The stacked structure is not ideal because fabrication cannot be achieved in a single batch process. The parasitic coupled structure is not ideal either because of the large area it occupies. However, this structure can be fabricated in a single batch process.

A traveling wave antenna was designed and investigated numerically and experimentally. A 4-arm microstrip antenna was fabricated to verify the theoretical design. The experimental results were in good agreement with the numerical results. This structure produced a broadside, circular polarized pattern with a single feed. The resulting operating bandwidth was 15 % on a thin substrate with a high relative permittivity. Unfortunately, the radiation efficiency was determined to be very low at 4.1 %. Recommendations are presented to improve the radiation efficiency.

Two other structures were investigated experimentally: a conically depressed patch and a concentrically shorted patch. Both structures prove to be difficult to fabricate with MMIC / MHMIC technology but yield an improved bandwidth with high radiation

efficiency. The conically depressed patch was investigated with a substrate having a high relative permittivity. The result was an impedance bandwidth of 3.8 % having a 3 dB ripple in the main beam. This can be compared to a circular patch on the same substrate with a 1.6 % bandwidth. The disadvantage of this structure is the complexity of its fabrication.

The structures investigated show bandwidth improvements, along with some undesirable traits which require further consideration. However, the information presented may be used in determining a design approach toward realizing the long term goal of an active phased array antenna.

Acknowledgements

I wish to express my sincere thanks and appreciation to Dr. L. Shafai and Dr. A. Ittipiboon for their guidance and advice throughout this project.

Special thanks to Brian Clarke and Brad Tabachnik for their help with the fabrication and measurements of the antennas designed in this thesis. As well, I would like to thank all those at the Department of Components and Subsystems, Communications Research Centre, who assisted with this project.

Finally, I would like to thank the Department of Components and Subsystems for the opportunity provided to carry out the research for this thesis in a cooperative environment between them and the University of Manitoba.

Table of Contents

List of Figures

List of Tables

CHAPTER 1 : Introduction

1.1 Purpose and Application

Since the technology of monolithic microwave integrated circuits (MMICs) and miniature hybrid microwave integrated circuits (MHMICs) was introduced in the 1960s, it has advanced steadily, and has been used in microwave applications of many kinds. It has been particularly useful in devices which must be reproduced in large numbers, and has resulted in very significant cost reductions. Consequently, it is a technology of great interest for application to active phased array antennas, which require circuit replication in the hundreds or thousands.

While the ultimate goal is to use MMIC technology for implementation, MHMIC technology may be used as a stepping stone toward this end. MHMICs have many similarities with MMICs and are less expensive and easier to implement in the small quantities required for experimental verification of theoretical design. One similarity is that both technologies use substrates which are thin and have high relative permittivity. These characteristics are well suited for the active circuitry, but are undesirable for antenna applications because they result in very narrow input impedance bandwidths. This thesis undertakes a study of the problem of devising a suitable radiating antenna element which would be compatible with MMIC / MHMIC technology.

1.2 Scope

Background information pertaining to MMIC / MHMIC technology is presented in Chapter 2. Also included in this chapter are the basic theory and the problems associated with phased array antennas and how MMICs can be applied.

Chapter 3 presents various techniques used to increase the impedance bandwidth of microstrip antennas. A traveling wave antenna design is presented in Chapter 4. The design is presented first, followed by an analytical study and then concluded with experimental results. Chapter 5 also presents a radiating structure which may be identified as a resonating type antenna. This chapter describes an experimental study also.

The final chapter of this thesis presents some conclusions concerning the antenna structures studied, and recommendations for future work.

CHAPTER 2: Background Information

2.1 Introduction

This chapter describes some of the underlying technologies used in the construction of phased array antennas and the attributes of these technologies. It also describes some physical and electrical characteristics of phased array antennas as they relate to the implementation techniques. Finally, it discusses some of the problems that arise, and which must be addressed in attempts to realize practical devices.

2.2 MMIC/MHMIC Technology

A monolithic microwave integrated circuit (MMIC) is a circuit which has all passive and active elements and interconnections implanted into the body, or onto the surface of a semi-insulating substrate, [2]. A miniature hybrid microwave integrated circuit (MHMIC) is a circuit which has only its passive elements implanted onto the surface of a substrate with the active devices connected to the circuit separately by wire bonds.

The monolithic microwave integrated circuit was first introduced in the mid sixties [2]. At that time, semi-insulating silicon was used as the substrate material. The fabrication of the circuit involved a diffusion process at high temperatures which resulted in the substrate losing the semi-insulating properties and becoming very lossy. As this is undesirable for microwave circuits, an operational MMIC was not attained until further developments in the area of material technology. Semi-insulating gallium arsenide (GaAs) was found to maintain its properties through high temperature processing and thus was suitable for MMIC technology because it exhibited low microwave losses. In addition, GaAs was found to have an electron mobility six times greater then that of silicon.

In GaAs MMIC fabrication, the passive components are produced on the semi-insulating substrate and the active devices are produced on an n-type layer which is formed by either epitaxial or ion-implantion techniques. The active and passive components are fabricated using a technique known as lift-off [5]. This involves defining a pattern in a layer of photoresist which is deposited on the GaAs wafer. Metal atoms are then evaporated and condensed on the wafer. Due to the pattern in the photoresistent layer, the metalization on the GaAs is separated from that on the photoresist as shown in figure 2.1. Thus, when the photoresist is dissolved, the metalization on the photoresist is removed leaving only a metalized pattern on the GaAs. This technique is also used to fabricate air bridges. An air bridge is a strip of metal suspended above the substrate, and is used to form interconnections. The air gap results in low capacitive coupling.

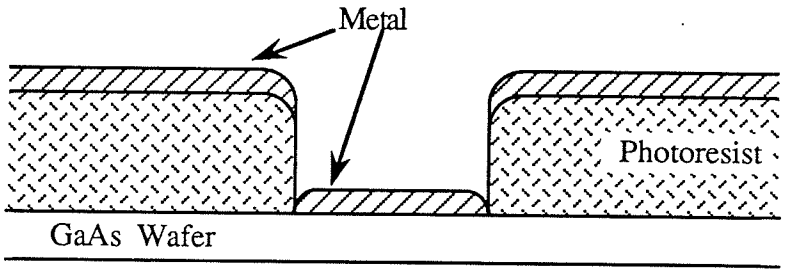

Fig. 2.1: Lift-off technique

Figure 2.2 shows a portion of a typical MMIC [5]. A field effective transistor (FET) and capacitor are shown with their respective dimensions. Note that grounding to the backside RF ground plane is achieved with a via hole. Via holes are holes through the substrate produced with either a sonic drill or chemical etching.

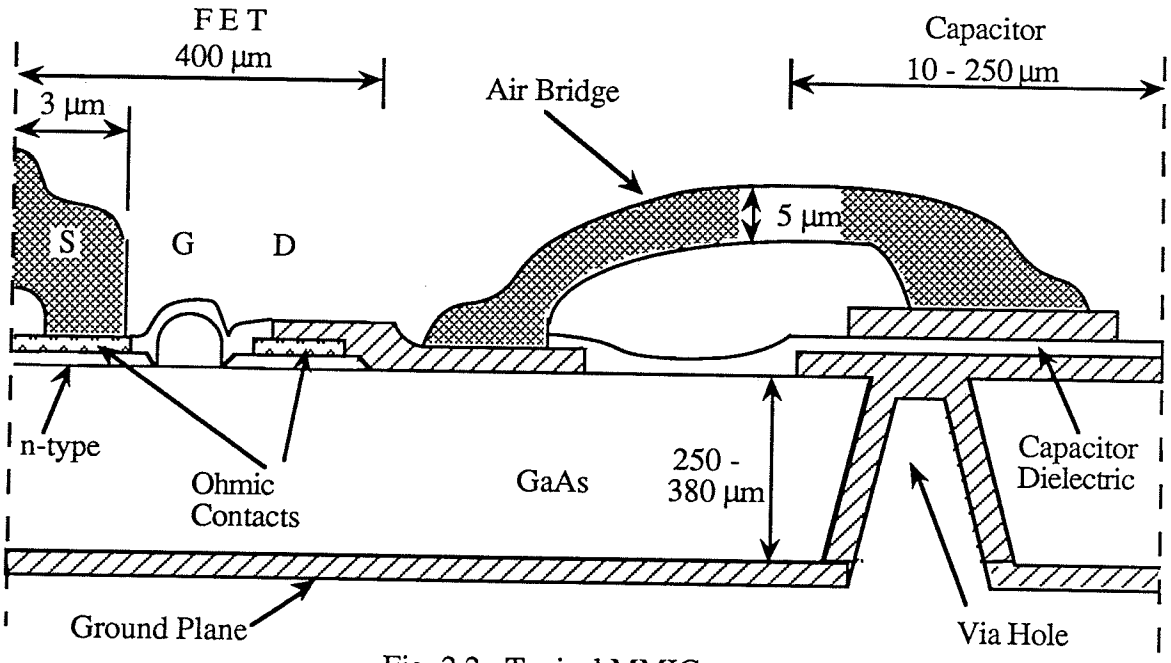

Fig. 2.2 : Typical MMIC

A miniature hybrid microwave integrated circuit differs from an MMIC in that its active devices are connected to the circuit separately with wire bonds. Since the active devices are not formed into or on the substrate, an n-type layer does not have to be formed. This allows the use of alternate substrates. The most commonly used substrate for MHMICs is Alumina because it has very low microwave losses. The passive components are fabricated in the same manner as in MMICs. With respect to both technologies, passive components could be in the form of lumped elements or distributed transmission lines.For frequencies less than 12.4 GHz, lumped elements are preferred because they occupy less area than transmission lines. For frequencies greater than 12.4 GHz, transmission lines provide better thermal dissipation [3] and are preferred. The associated wire bonding with MHMICs results in this technology being more labour intensive and tends to reduce its reliability and reproducibility. However, for applications in which many identical circuits are not required, this technology can be used to provide circuits more quickly and is very desirable.

Between the two technologies, MMICs would be the more ideal to apply to a phased array antenna. An antenna of this nature requires many identical components, up to hundreds and thousands. An MMIC approach would be favorable for the following reasons.

1. low cost

2. small size and light weight

3. improved reliability and reproducibility

Batch fabrication of a entire circuit many times over yields a low cost process. In addition, the wire bonding associated with MHMIC is labour intensive and hence costly. The wire bonding also introduces reduction in reliability and reproducibility. As can be seen in Figure 2.2, the size of a MMIC is very small and hence it is light weight. Thus the potential of MMIC technology for active phased array antennas is high.

2.3 Phased Array Antennas

An antenna may contain one or more radiating elements in its structure. The number of elements required is dependent on the desired performance. Some of the performance criteria are pattern directivity, power gain and scanning ripple. If an antenna with one radiating element does not satisfy the criteria, then more elements may be added until the desired specifications are obtained. The resultant is an array of radiating elements whose performance depends on the element configuration and excitation amplitude and phase. An antenna whose main beam of radiated power is steered by element excitation phase changes is called a phased array. With an electronically steered main beam, the antenna can be secured in a fixed position and can scan at rates unattainable by mechanically scanned

antennas. The antenna elements may appear in various configurations, such as linear, planar and circular arrays. When addressing the issues of large phased arrays containing hundreds or thousands of elements, some sort of planar array would most likely be utilized. Thus the basic theory of operation and associated problems of planar arrays follow [13], [14].

The main beam of an array may be characterized by the product of the element factor and the array factor. A phased array antenna will typically be constructed of N identical radiating elements having certain characteristics. The element excitation and orientation dictate the type of radiation pattern obtained. This is known as the element pattern and represented by $F_n(\theta,\phi)$. In an array, each element is fed by currents having amplitude and phase. The sum of contributions from all these element currents is known as the array factor and is a function of element location and their complex excitation. A planar array with arbitrary element locations is given in Figure 2.3

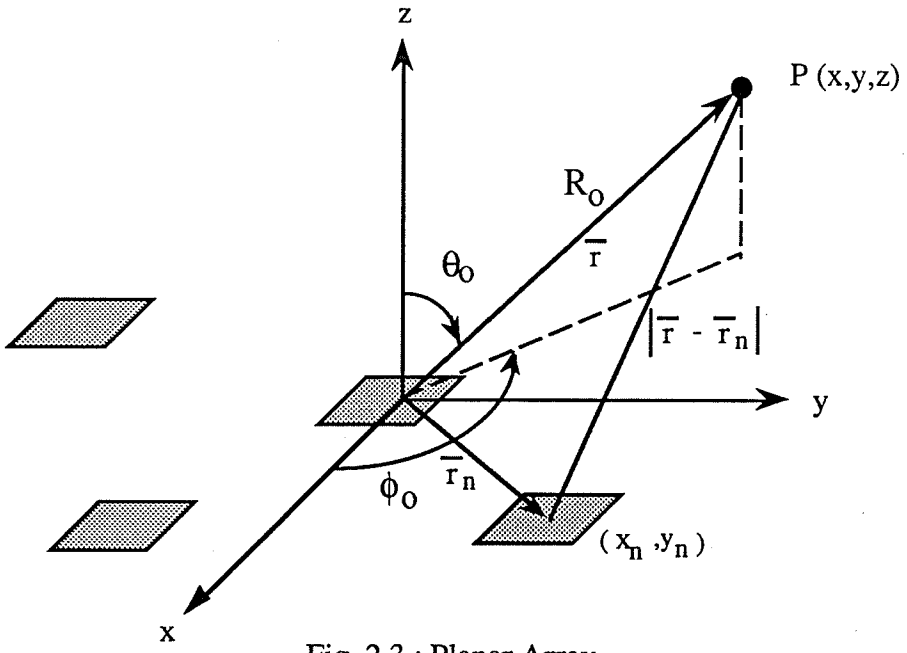

Fig. 2.3 : Planar Array

If mutual coupling between radiating elements is neglected, the total radiated field may be given as

$$\bar{E}(\theta,\phi) = A\sum_{n} \bar{F}_n(\theta,\phi)\, I_n \frac{e^{-jk|\bar{r}-\bar{r}_n|}}{|\bar{r}-\bar{r}_n|} \tag{2.1}$$

where $F_n(\theta,\phi)$ is the element pattern

I_n is the complex excitation

A is a constant

k is the wave number, $k = 2\pi/\lambda$

where the wave length, $\lambda = c/f$

c is the velocity of light in free space

f is frequency

$$|\bar{r} - \bar{r}_n| = [\,(x-x_n)^2 + (y-y_n)^2 + z^2\,]^{1/2}$$

for the far field case, let the distance for the origin of the array to the observation point be represented by R_o and approximate $|\bar{r} - \bar{r}_n|$ with

$$|\bar{r} - \bar{r}_n| \cong R_o - \bar{r}_n \cdot \hat{\rho}$$

where $\hat{\rho} = u\hat{x} + v\hat{y} + \cos\theta\,\hat{z}$

and u and v are the directional cosines; $u = \sin\theta\cos\phi$

$v = \sin\theta\sin\phi$

Thus, equation (2.1) may be written as

$$\bar{E}(\theta,\phi) = A\sum_{n} \bar{F}_n(\theta,\phi) I_n \frac{e^{-jk(R_o - \bar{r}_n\cdot\hat{\rho})}}{(R_o - \bar{r}_n\cdot\hat{\rho})}$$

$$\bar{E}(\theta,\phi) = A\frac{e^{-jkR_o}}{R_o}\sum_{n} \bar{F}_n(\theta,\phi) I_n e^{jk\bar{r}_n\cdot\hat{\rho}} \tag{2.2}$$

where $r_n\cdot\hat{\rho}$ may be neglected in the denominator since its magnitude is $<< R_o$

A main beam can be formed and steered to any location in space specified by the angle (θ_o,ϕ_o). This may be accomplished by selecting appropriate excitation currents. Two methods of steering may be utilized, time delay steering or phase steering. As can be seen in equation (2.2), the projected distance of each element to the selected point in space varies for each element. Time delay steering incorporates an excitation phase which compensates for these differences, resulting in co-phasal addition of their contributions thus

$$I_n = |I_n| e^{-jk\bar{r}_n \cdot \hat{\rho}_o} \tag{2.3}$$

substituting into equation (2.2) for a point specified by $(\theta o,\phi o)$ yields

$$\bar{E}(\theta_o,\phi_o) = A \frac{e^{-jkR_o}}{R_o} \sum_n \bar{F}_n(\theta_o,\phi_o) |I_n| e^{-jk\bar{r}_n \cdot \hat{\rho}_o} e^{jk\bar{r}_n \cdot \hat{\rho}_o}$$

$$\bar{E}(\theta_o,\phi_o) = A \frac{e^{-jkR_o}}{R_o} \sum_n \bar{F}_n(\theta_o,\phi_o) |I_n| \tag{2.4}$$

Equation (2.4) shows that time delay steering can be used to control beam steering over a wide range of frequencies. However, time delay devices are costly and hence phase steering becomes a desirable method. Phase steering is accomplished by utilizing phase shifters at each element designed to operate at a specific frequency, f_o. Thus the excitation current becomes

$$I_n = |I_n| e^{-jk_o \bar{r}_n \cdot \hat{\rho}_o}$$

where $k_o = 2\pi/\lambda_o$, $\lambda_o = c/f$

substituting into equation (2.2) yields

$$\overline{E}(\theta,\phi) = A\,\frac{e^{-jkR_o}}{R_o}\sum_n \overline{F}_n(\theta,\phi)\,|I_n|\,e^{-jk_o\bar{r}_n\cdot\hat{\rho}_o}\,e^{jk\bar{r}_n\cdot\hat{\rho}}$$

$$\overline{E}(\theta,\phi) = A\,\frac{e^{-jkR_o}}{R_o}\sum_n \overline{F}_n(\theta,\phi)\,|I_n|\,e^{j\bar{r}_n\cdot(k\hat{\rho}-k_o\hat{\rho}_o)} \qquad (2.5)$$

Equation (2.5) shows that at a specified point (θ_o,ϕ_o), there is a frequency dependence. Thus the operational bandwidth of a phase steered array becomes quite small because it is limited by the bandwidth of the phase shifters. Other problems associated with phased arrays are grating lobes, and scan blindness.

Grating lobes are radiation patterns equivalent to the main beam but at other angular positions. This is generally undesirable and may be avoided by keeping the element spacing fairly small. Mailloux [14] has examined this problem thoroughly and has shown that element spacing less than one-half wavelength will generally suppress grating lobes. In addition, one could select an element type which has a null in its radiation pattern corresponding to a grating lobe location.

Scan blindness is a condition when the antenna array does not radiate any power at a certain scan angle. This phenomenon is related to the impedance of each element of the array as the beam is scanned. Thus mutual coupling must be addressed. The voltage at each element is the excitation voltage and the contribution from all other elements;

$$V_1 = I_1 Z_{11} + I_2 Z_{12} + I_3 Z_{13} + \ldots + I_n Z_{1n}$$

$$V_2 = I_1 Z_{21} + I_2 Z_{22} + I_3 Z_{23} + \ldots + I_n Z_{2n}$$

$$\vdots$$

$$V_n = I_1 Z_{n1} + I_2 Z_{n2} + I_3 Z_{n3} + \ldots + I_n Z_{nn}$$

$$\text{but } Z_1 = \frac{V_1}{I_1}$$

$$\therefore Z_1 = Z_{11} + Z_{12}\frac{I_2}{I_1} + Z_{13}\frac{I_3}{I_1} + \ldots + Z_{1n}\frac{I_n}{I_1}$$

$$Z_2 = Z_{22} + Z_{21}\frac{I_1}{I_2} + Z_{23}\frac{I_3}{I_2} + \ldots + Z_{2n}\frac{I_n}{I_2}$$

$$\vdots$$

$$Z_n = Z_{nn} + \ldots + Z_{n3}\frac{I_3}{I_n} + Z_{n2}\frac{I_2}{I_n} + Z_{n1}\frac{I_1}{I_n}$$

Note that the impedance of each element is the sum of its self-impedance and the mutual impedances weighted by a current ratio. The currents are functions of scan angle and hence these ratios vary with scan angle. Thus it is conceivable that at a certain scan angle, the element impedance could become quite large, creating a large reflection coefficient and preventing energy from radiating.

In addition, Pozar [12], determined that scan blindness is also related to the resonance of a trapped surface wave mode. He also studied the effects of substrate thickness, relative permittivity and element spacing with respect to the scan blindness angle. The normal operating condition is to contain the beam in the broadside direction. Pozar found that the scan blindness angle approaches broadside as substrate thickness, relative permittivity and element spacing decrease. These parameters should be taken into consideration when applying MMIC technology to phased array antennas.

2.3.1 MMIC Phased Arrays

The application of MMICs to phased array antennas is a relatively new field and many problems are associated with it. However, the promising characteristics of the resulting antenna structure warrants research in this area. MMIC phased array antennas

have been addressed in the literature [6]-[12], [15]. Application of MMICs can result in the fabrication of an active phased array antenna which is very compact, light weight, conformal and cost effective. It is now possible to fabricate phase shifters and amplifiers at the element level, enabling control of the amplitude and phase at each element. Thus each element in the array may be considered as being active. Adjusting the excitation current amplitudes results in shaping the beam and having some control over the side lobe levels. Over all, an active phased array antenna has improved performance which results in the reduction of the number of elements and hence cost. For the transmitting case, the amplifiers at each element are sufficient to replace a high power source with one of lower power. This would again reduce cost and size and at the same time increase reliability. The general architecture of a MMIC phased array antenna must now be considered.

Two general architectures which have been reported are the brick and tile configuration as shown in Figure 2.4. The brick configuration contains modules perpendicular to the aperture plane while the tile configuration has the circuitry and radiating elements parallel to the aperture plane. The tile structure yields a conformal array while the brick structure does not.

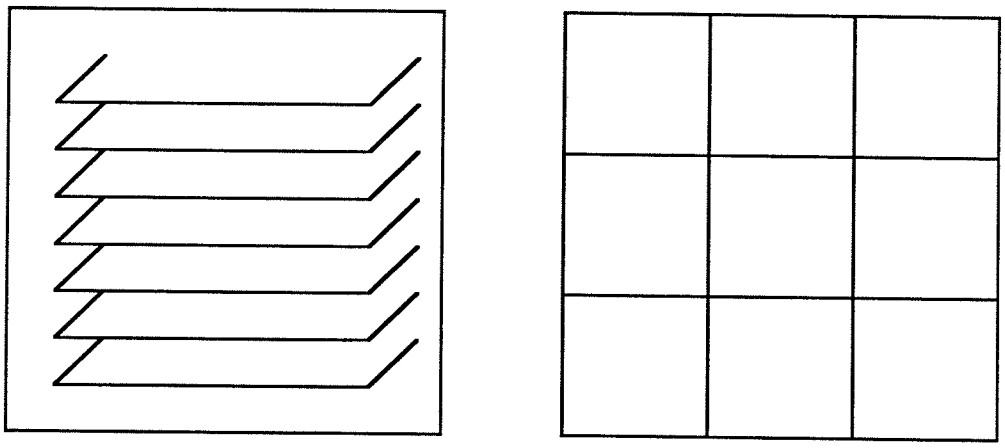

Brick Tile

Fig. 2.4 : Basic Architectures

The brick structure has depth which is a function of the circuitry required. As the number of circuits increases, the depth increases, while the area increases in the tile structure. It should be noted that the brick structure is considerably better then the tile structure for heat dissipation. This is an important factor to consider with MMICs, since GaAs is a poor thermal conductor. This results in the tile structure having an increased thermal resistance. Selection between these two architectures is dependent upon the application. For conformal array applications, the tile structure would be used and this is the type considered throughout this thesis.

Three basic tile architectures are shown in Figure 2.5 which illustrate a single layer and double layer structure, each characterized by different feeding schemes.

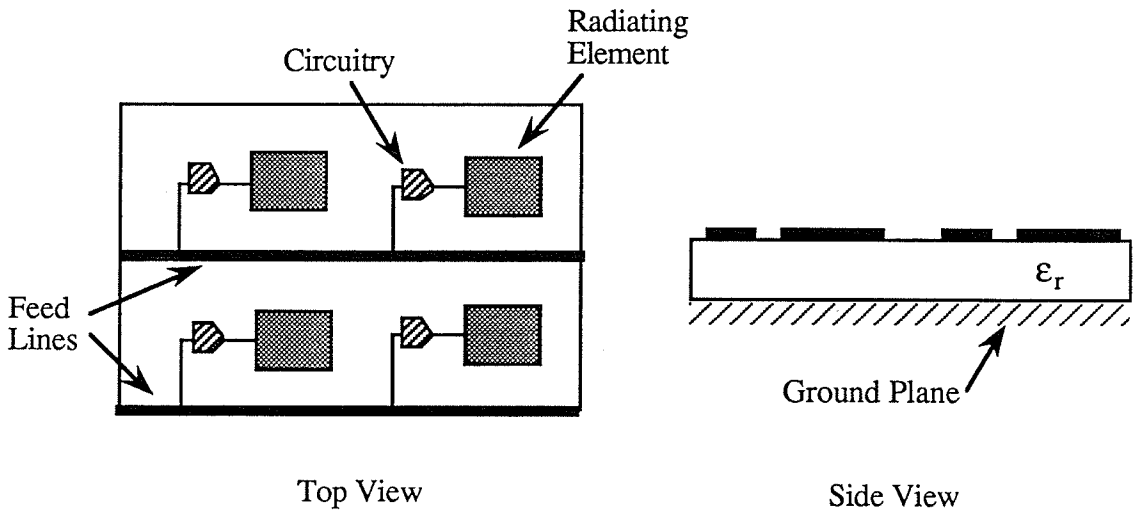

(a) Single Layer: Direct Feed

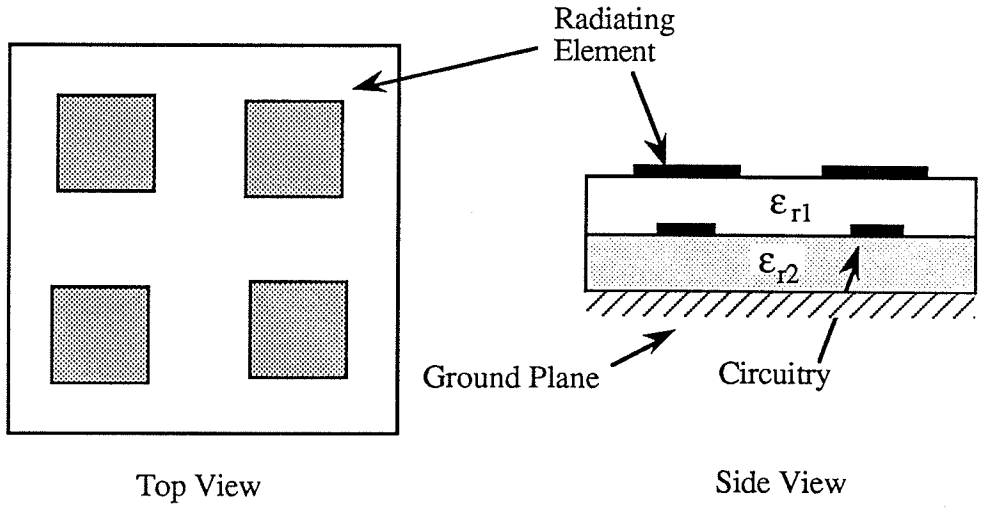

(b) Double layer:Proximity Coupling

Fig. 2.5 : Tile architectures

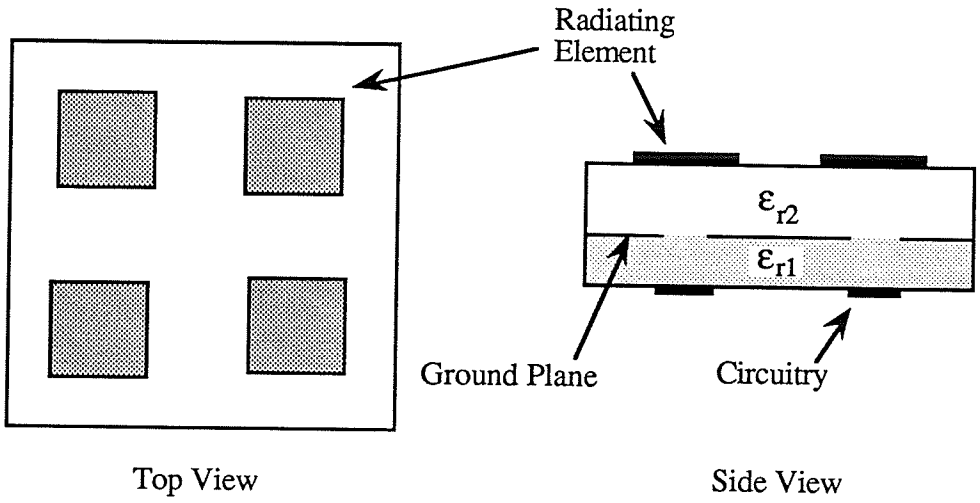

(c) Double layer : Aperture coupling

Fig. 2.5 (cont.)

The single layer structure shown in Figure 2.5 (a) would be ideal since it is the only truly monolithic structure. That is, all the circuitry, feed lines and radiating elements could be fabricated in a one batch process. With hundreds to thousands of identical units required, this becomes very desirable and feasible. However, there are many problems associated with a single layer structure because all components of the array are placed on a GaAs substrate. A fundamental problem is that the GaAs substrate used for the circuitry is not very suitable for radiating elements. The GaAs substrate is very thin, varying from h = .254 mm to h = 1.27 mm, and has a relative permittivity (ε_r) close to thirteen. These properties are not desirable for radiating elements and are discussed further in Chapter 3. In general, radiating elements demonstrate improved performance on thicker dielectric substrates having low relative permittivities. This is the rationale behind the multi-layered structures shown in figure 2.5. The structure in figure 2.5 (b) has a high relative permittivity substrate layer, ε_{r1}, for the circuitry and a low relative permittivity dielectric

layer, ε_{r2}, for the radiating elements. Excitation of the radiating elements is accomplished with proximity coupling. However, this structure is susceptible to undesirable circuit element coupling to the radiating elements. The structure in Figure 2.5 (c) eliminates this problem by feeding with aperture coupling . The multiple dielectric layers are for circuitry and antenna as before. However, a ground plane is situated in between the two layers, hence eliminating unwanted coupling.

When utilizing these tile structures for phased array antennas, it would be desirable to steer the main beam with a combination of phase and time delay steering. This would be a compromise between the cost of the time delay steering and the limited bandwidth of phase steering. In addition, the antenna could be built in a subarray module approach to further reduce the cost and complexity as illustrated in figure 2.6. This involves dividing the array into smaller subarrays which could then be constructed as plug-in units to form the total array. Each element would be phase steered and each module timed delayed steered. This concept of plug-in units has advantages in trouble shooting and repairing an array. Each unit could be tested for proper operation and a malfunctioning unit could be replaced with an operating unit. This is advantageous because MMICs cannot be altered or repaired after they are fabricated.

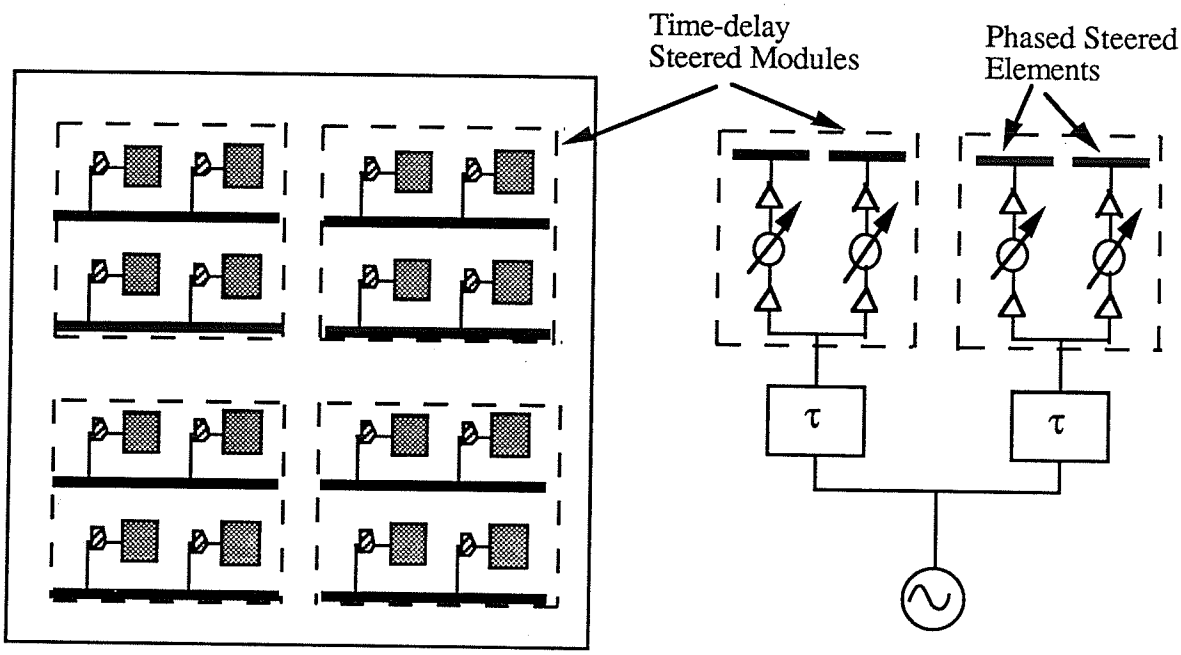

Fig. 2.6 : Modular Phased Array

The single layer tile architecture has been chosen for further study because of its monolithic nature. An MMIC phased array of this type can be expected to exhibit all the basic problems of phased arrays mentioned previously as well as new ones. The mutual coupling equations showed that the impedance of each element changes as scan angle changes, hence radiating elements with large input impedance bandwidths are desired. A major problem arises here, as printed microstrip antennas have, by nature, small input impedance bandwidths. This is further complicated by the fact that the bandwidth decreases as substrates with high relative permittivities, such as GaAs, are used. In addition, the bandwidth decreases when thin substrates are used, such as those for MMICs. Thus the problem of limited input impedance bandwidth on thin, high dielectric substrates was studied. This prompted the review of existing techniques to increase bandwidth.

CHAPTER 3 : Review of Bandwidth Improvement Techniques

There are several bandwidths associated with the operating characteristics of an antenna. The bandwidths of interest in this study are the input impedance bandwidth, BW_{Zin}, and the pattern bandwidth, BW_{pat}. BW_{Zin} has been defined differently by various authors and hence is defined here for clarity. The input impedance bandwidth, BW_{Zin}, is taken as, " the frequency range over which the input voltage standing wave ratio (VSWR) is less then a specified value" [16]. Usually a VSWR of two is used to determine BW_{Zin}, which corresponds to a return loss of -10 dB. At frequencies throughout this bandwidth, it is usually desired to maintain a relatively constant radiation pattern, thus one should be aware of the pattern bandwidth, BW_{pat} . This may be defined as "the frequency range over which the radiated power is within 3 dB of the incident power and the radiation pattern is essentially the same" [16]. A suitable radiating element for MMIC application should be based on the size of the operating bandwidth. An operational bandwidth, BW_{op}, is defined as the frequency range in which both the input impedance and radiation pattern are within the design criteria, in other words, the intersection between BW_{Zin} and BW_{pat}.

Broadbanding techniques have been reviewed in the literature, [16]-[30], most recently by Gupta [16]. In general, there are two approaches to increase the input impedance bandwidth of a microstrip antenna, either modifying the radiating element itself or improving the impedance matching network .

It was noted previously that thin, high dielectric substrates used in MMICs reduce the bandwidth of a resonating patch structure. A microstrip patch is a thin layer of metal bonded to a grounded substrate as shown in figure 3.1. The principal radiating mechanism of this structure is the fringing fields at the edges of the patch. The energy fed to the patch occupies the region under it. A boundary of this region is the patch's edge where there is a large amount of reflection due to the open circuit conditions seen at the edge. Thus, the

actual amount of energy radiated is not very high and this structure is considered to behave more as a cavity.

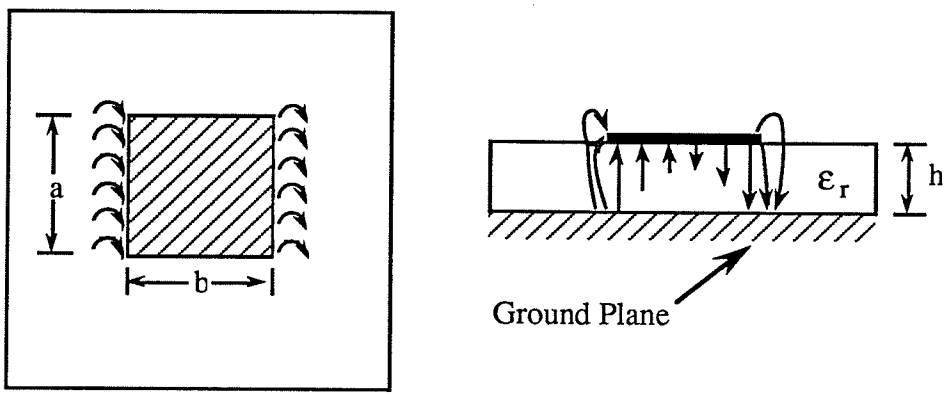

Top View Side View

Fig. 3.1 : Rectangular Microstrip Patch

This structure was analyzed in [31] using a variety of models and the input impedance bandwidth for a rectangular patch was determined to be

$$BW_{Zin} = \frac{VSWR - 1}{Q_t \sqrt{VSWR}} \tag{3.1}$$

where $\frac{1}{Q_t} = \frac{1}{Q_r} + \frac{1}{Q_c} + \frac{1}{Q_d}$

Q_t is the total quality factor consisting of the losses due to radiation (Q_r), the conductor (Q_c), and the dielectric (Q_d). These losses have been defined in [31] and [35] by

$$Q_d = \frac{1}{\tan \delta} \tag{3.2 a}$$

where $\tan \delta$ is the tangent loss defined by $\tan \delta = \frac{Re \{ \varepsilon_r \}}{Im \{ \varepsilon_r \}}$

$$Q_c = h \sqrt{\mu_o \pi f_r \sigma_c} \tag{3.2 b}$$

where μ_o is the permeability of free space

σ_o is the bulk conductivity

f_r is the resonant frequency and is approximately given by

$$f_r = \frac{1}{2\sqrt{\mu_o \varepsilon_o \varepsilon_r}} \sqrt{\left(\frac{m}{a}\right)^2 + \left(\frac{n}{b}\right)^2}$$

for the dominant mode ; m = 0, n = 1

$$f_r = \frac{1}{2b\sqrt{\mu_o \varepsilon_o \varepsilon_r}}$$

where ε_o is the permittivity of free space

b is the width

$$Q_r = \frac{c\sqrt{\varepsilon_{eff}}}{4 f_r h} \qquad (3.2\ c)$$

where ε_{eff} is the effective permittivity defined by

$$\varepsilon_{eff} = \frac{\varepsilon_r + 1}{2} + \frac{\varepsilon_r - 1}{2}\left(1 + \frac{12h}{w}\right)^{-0.5}$$

Equation (3.1) shows that the bandwidth is inversely proportional to the quality factor. An efficient antenna would have large losses due to radiation and if these losses could be increased, thus lowering the total Q, the bandwidth would increase. Equations (3.2 a, b, and c) show the effects of substrate thickness, h, and relative permittivity, ε_r, on each individual Q-factor which can then be related to the bandwidth, BW_{Zin}.

The effects of using a thin, high relative permittivity substrate as in MMICs are now considered. Equation (3.2 a) shows that Q_d is only dependent on ε_r. It has been found that as ε_r increases, the loss tangent decreases, thus Q_d increases resulting in decreasing BW_{Zin}. Equations (3.2 b and c) are strongly dependent on the thickness, h. As h

decreases, Q_r increases and an increase in ε_r creates an increase in ε_{eff} and a decrease in f_r which again increases Q_r. This causes Q_t to increase and hence decreases BW_{Zin}. These variations of h and ε_r have the opposite effect on Q_c, thus generating a decrease in Q_c. This means higher conductor losses which are not desirable since the dominant factor should be the radiation loss. These effects were experimentally determined in [27]. Two rectangular patches with f_r = 10 GHz were constructed on Alumina, ε_r = 9.8, h = .625 mm, and Polyguide, ε_r = 2.32, h =1.59 mm. The thicker substrate with low relative permittivity had a bandwidth of 6.6 % while the thinner, high ε_r substrate had a bandwidth of 1.1 %.

A variation of the microstrip patch was studied at the Communications Research Center (CRC), [19]. The solid patch structure was replaced with a mesh structure. The rectangular mesh patch shown in Figure 3.2 was constructed with air bridges and formed on a GaAs substrate.

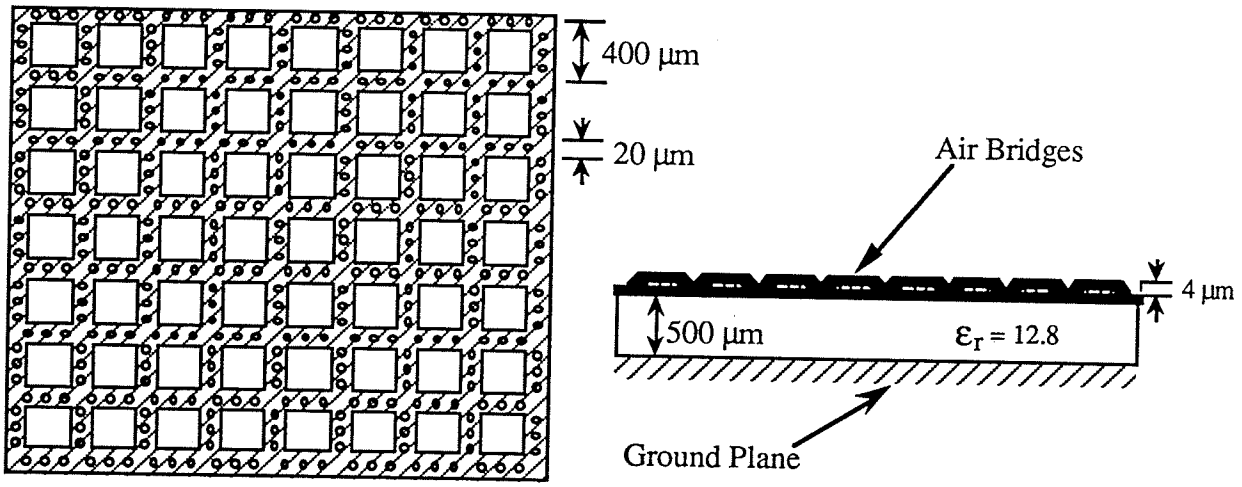

Fig. 3.2 : Mesh microstrip patches.

Improvement in bandwidth over a conventional solid patch was expected due to the air gaps created by the bridging. The introduction of these air gaps lowers the effective

permittivity thus improving the bandwidth. However, the maximum bridge height attainable is 4 μm. Thus the improvement in bandwidth was not significant. A circular solid patch and a rectangular solid and mesh patch were fabricated on GaAs substrate (ε_r =12.8, h = 0.5 mm, f_0 = 14 GHz) and evaluated. Both the solid circular and rectangular patches reported an impedance bandwidth of 1.7 % with resonant frequencies of 14.78 GHz and 13.5 GHz respectively. The mesh rectangular patch had a reported bandwidth of 2.1 % at f_0 = 13.86 GHz.

Attempting to lower the effective permittivity leads to a multi-layered structure in which the radiating element is on a different substrate from the circuit substrate. The radiating element is formed on a thicker substrate of low relative permittivity suitable for enhancing the bandwidth. Several of these structures are shown in figure 3.3

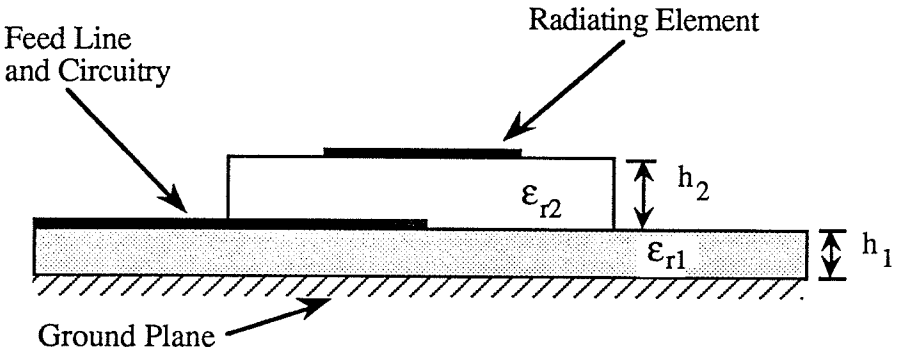

(a)

Fig. 3.3 : Various multi-layered structures

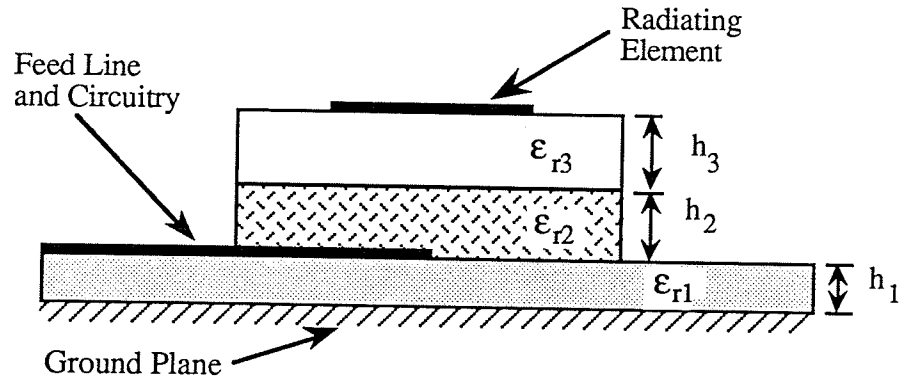

(b)

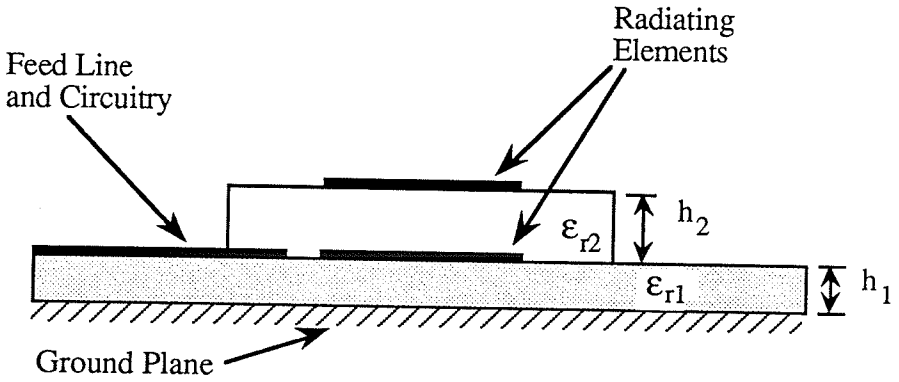

(c)

Fig. 3.3 (cont.)

In order to compare the merits of various configurations, the bandwidths of rectangular patchs on high and low relative permittivities will be taken as a basis. It has been reported [27] that the bandwidth of a rectangular patch on a substrate with $\varepsilon_r = 2.32$, h =1.59 mm, f_o = 10 GHz is 6.6 %. The same patch on a substrate with $\varepsilon_r = 9.8$, h = .625 mm is reported to have a BW_{Zin} = 1.1 %. The notable decrease is again due to the thin, high

relative permittivity substrate. The two layered structure shown in figure 3.3(a) has a reported BW_{Zin} =13%, [27] (ε_{r1} = 9.8, h_1 = .625 mm, ε_{r2} = 2.32, h_2 = 2.34 mm, f_o = 10.6 GHz). This was further improved to 18% by inserting another layer as shown in figure 3.3(b). Figure 3.3(c) shows a multi-resonating structure. This structure involves two radiators vertically stacked. The size of the top patch in relation to the bottom patch could be smaller, larger or the same. The radiation mechanism with a smaller top patch is a combination of both of the fringing fields due to the edges of each patch. A larger top patch utilizes the bottom patch as a feed patch and the radiation is at the boundary of the top patch. When the top and bottom are identical, there is a combined effect of the two fringing fields. The case of having a larger element on top was studied in [22] and a bandwidth of 24.9 % was reported (ε_{r1} = 10.5, h_1 = .635 mm, f_1 = 10.06 GHz, ε_{r2} = 2.2, h_2 = 2.34 mm, f_2 = 8.56 GHz). These structures show a large improvement in bandwidth at the expense of increasing total height and complicating the fabrication process. In addition, the multi-layered substrate structures are not yet fully understood and final designs are achieved by experimental iterations. These structures could be used for an MMIC phased array antenna. However, it would be desirable to keep the radiating element and circuitry on the same substrate to enable a one batch fabrication process.

A variation of the multi-layered structures discussed is an element with a superstrate as shown in figure 3.4. Bhattacharyya [29] studied the effects of superstrates on resonant frequencies, input impedance and corresponding bandwidth.

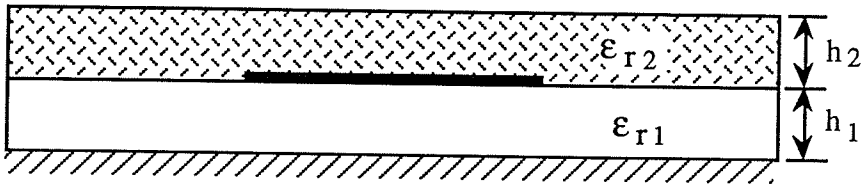

Fig. 3.4 : Element with superstrate

Experimental work was done using rectangular patches on substrates with $\varepsilon_{r1} = 2.32$, $h_1 = 3.18$ mm. The superstrate varied in thickness but had the same relative permittivity as the substrate. It was reported that as the superstrate thickness increased, the resonant frequency decreased. The decrease in resonant frequency modified the input impedance, but the impedance bandwidth remained relatively constant. The measurements performed have been listed in Table 3.1.

Substrate Thickness (mm)	$BW_{Z_{in}}$ (%)	f_r (GHz)
0.0	5.6	2.845
3.18	5.7	2.749
6.36	4.6	2.704
9.54	4.6	2.682
12.72	4.6	2.670

Table 3.1 : Effects of Superstrate on Impedance Bandwidth

The effects of the superstrate on gain or efficiency were not reported, nor were the effects due to superstrates of different relative permittivities. These factors were studied in [28] where it was determined that very high gain patterns are produced as the superstrate permittivity increases. This is a result of the superstrate acting as an impedance transformer to free space. It was found that the bandwidth varied inversely to gain and improvements in radiation efficiency were noted. In addition, the radiation patterns were found to be narrow beams without side lobes. Thus a superstrate could be selected to enhance the gain, at some cost to the bandwidth, and at the same time provide protection against environmental factors. Due to the degradation in bandwidth, it is unlikely that a superstrate would be applied to MMIC phased arrays.

Another method noted to increase the bandwidth is the parasitic coupling. This incorporates an active element and several passive elements which are either capacitively coupled by narrow gaps or directly coupled. A configuration reported in [16] is shown in figure 3.5.

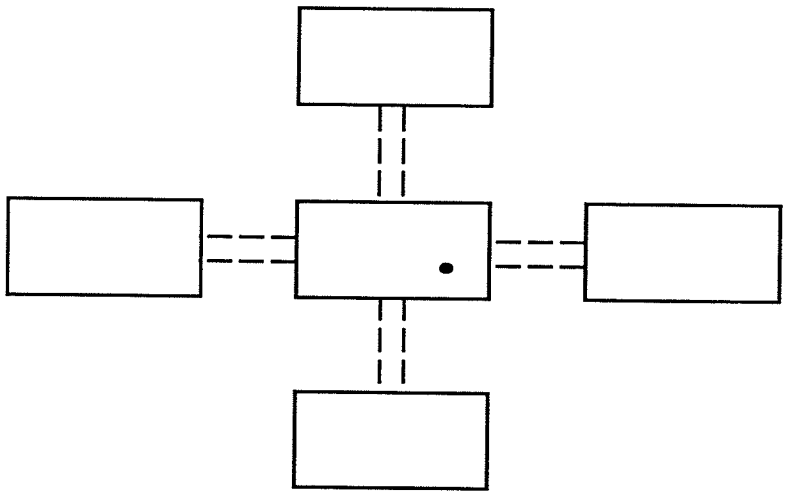

Fig. 3.5 : Parasitic coupled structure

Each patch in figure 3.5 has a slightly different length, resulting in various resonating frequencies. This broadens the frequency response and a bandwidth of 25.8 % and 24 % (ε_r = 2.55, h = 3.18 mm, f_0 = 3.16 GHz) have been reported for the case of gap coupling and direct coupling respectively. Two problems associated with this type of structure are the large area occupied and radiation pattern variation within the impedance bandwidth. Nevertheless, parasitic coupled elements would be suitable for a one-batch fabrication process. However, the cost increases because a large amount of chip area must be allocated to the radiating structure.

An alternate approach to improve bandwidth by the matching network has a similar disadvantage. The impedance bandwidth has been found to increase by using an improved matching network, [17]. A bandwidth of 10 % has been reported with the use of such a network (ε_r = 2.2, h = 1.5 mm, f_0 = 3 GHz). This approach is not particularly desirable because it occupies more of the chip area.

Modifications to the standard rectangular microstrip patch antenna, which produce improved bandwidth performance have been presented thus far. Different geometries of microstrip antennas should be considered also, since some have inherently larger bandwidths. A folded dipole is reported in [23] to have an impedance bandwidth of 7.2 % (ε_r = 2.55, h = 3.2 mm, f_0 = 8.3 GHz). Other structures are annular rings and conically depressed circular patches as shown in Figure 3.6.

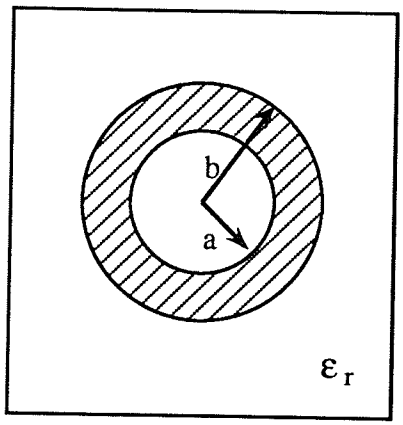

Top View

Fig. 3.6 a) : Annular ring microstrip patch

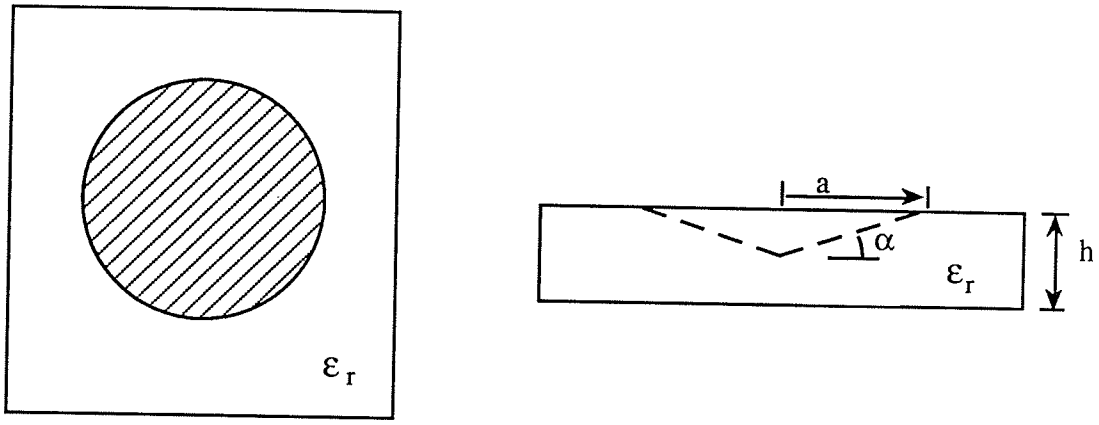

Top View

Side View

Fig. 3.6 b) : Conically depressed circular microstrip patch

Annular rings operating in the TM_{11} and TM_{12} modes generate a broadside radiation pattern. The TM_{12} mode has a reported bandwidth two times larger than a circular disk having an equivalent substrate thickness and resonant frequency [46]. An interesting structure shown in figure 3.6(b) was studied in [43]. A bandwidth of 28.7 % was

claimed for an angular depression, α, of five degrees (ε_r = 2.5, h = 6 mm, f_o = 2.98 GHz). This structure is discussed in detail in Chapter 5.

The radiating elements presented thus far have all been resonating type structures. An alternate radiating structure is a traveling wave antenna which is further discussed in Chapter 4. An example is the spiral antenna as shown in figure 3.7. This structure is frequency independent and exhibits large impedance and pattern bandwidths. The spiral is frequency independent because it is constructed entirely of angles, thus the shape does not change as frequency changes, only the active area of radiation shifts.

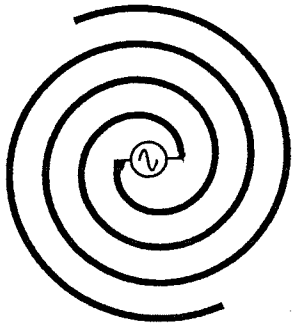

Figure 3.7: 2-arm spiral Antenna

The active area of radiation described in [32] is at a circumference of one wavelength. The two currents fed out-of-phase at the center of the spiral become in-phase at this point, resulting in maximum radiation. Thus the operational bandwidth is dependent upon the size of the spiral. Higher frequencies will utilize the inner portion of the antenna while lower frequencies the outer portion. Nakano [30], [33], [34] has thoroughly studied spirals and

has indicated two conditions in which circular polarization can be attained with a four-arm spiral. Circular polarization in the broadside will be present, provided the outer circumference is either 1.4 or three wavelengths. An outer circumference of 3λ is preferable since an improved axial ratio is generated [34]. It has recently been reported [30] that selective phasing at the inputs can generate a circular polarized wave in the opposite direction of the windings. Reported experimental data of a two arm spiral with outer circumference of 1.4λ show an impedance bandwidth of 20 % and a pattern bandwidth of 16 % where the limiting factor was the axial ratio ($\varepsilon_r = 1$, h = 1.25 cm, $f_o = 6$ GHz). The large bandwidth is appealing for MMIC application, thus a traveling wave structure was selected and studied as a possible compatible element for an MMIC phased array.

Most of the structures which have been reviewed have been deposited on substrates with low relative permittivity. The structures on substrates with high dielectric constants achieve improved bandwidth performance utilizing a multi-layered scheme. Little attention has been given to developing an antenna element with a relatively large impedance bandwidth on a high dielectric substrate. This is the design goal, since a radiating element of this nature is ideally suited for an MMIC phased array antenna. As a stepping stone to MMIC applications, MHMIC technology will be used due to the substrate similarities and the simpler fabrication process involved for a small number of elements. The relative permittivity of GaAs used in MMICs and alumina used in MHMICs is 12.8 and 9.8 respectively. Thus an antenna developed on alumina could then be transferred to an MMIC.

Variations of a circular patch have been selected as resonating structures which might generate a relatively large impedance bandwidth on high dielectric substrates. In addition, a traveling wave structure was designed, fabricated on an alumina substrate, and studied as a possible candidate for MMIC applications.

CHAPTER 4 : Traveling Wave Antenna

4.1 General Theory

A traveling wave antenna, as defined in [36], is "an antenna for which the fields and currents that produce the antenna pattern may be represented by one or more traveling waves, usually in the same direction". Traveling waves are waves which propagate with a uniform phase progression. A traveling wave antenna is match terminated to absorb any energy at the end of this structure. The purpose of this is to create zero reflection at the end, resulting in the set-up of a traveling wave distribution on the structure. Removal of the load would result in a total reflection at the end of the structure and create a traveling wave in the direction opposite to the initial wave. The combination of waves would produce a standing wave which would then exist on the structure. The operation of a traveling wave antenna is further explained with an example of a straight wire above a ground plane which is match loaded. This structure is illustrated in figure 4.1.

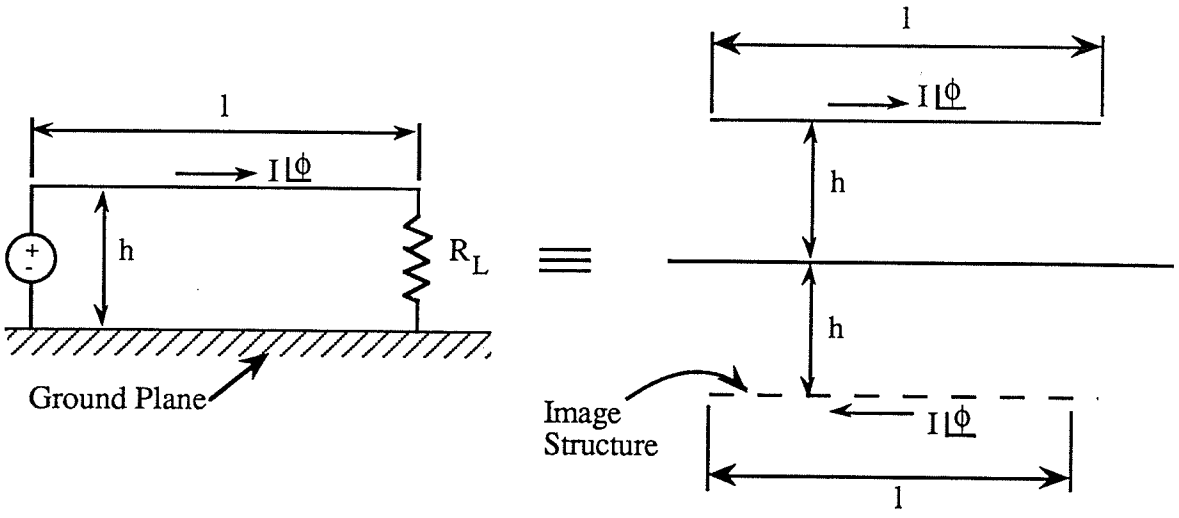

Fig. 4.1 : Straight wire traveling wave antenna

As current travels along the wire from the source to the load, it is attenuated due to radiation. The remaining current at the end of the wire is absorbed by the load to prevent any reflections back toward the source. The ground plane causes an image of the wire to appear below the ground plane at a distance h. Thus the total pattern will be due to that of the wire and the pattern reflected in the ground plane. The height of the wire above the ground plane may be selected to have the two patterns add in phase.

These concepts are now applied to microstrip line antennas. The radiating mechanism of this type of structure are the discontinuities along the line. Unlike the wire, a straight microstrip line has minimal radiation due to its field distribution. The field distribution is transverse electromagnetic (TEM) meaning that both the electric, E, and magnetic, H, fields are perpendicular to the direction of propagation. These are illustrated in figure 4.2 where the direction of propagation is in the x-direction.

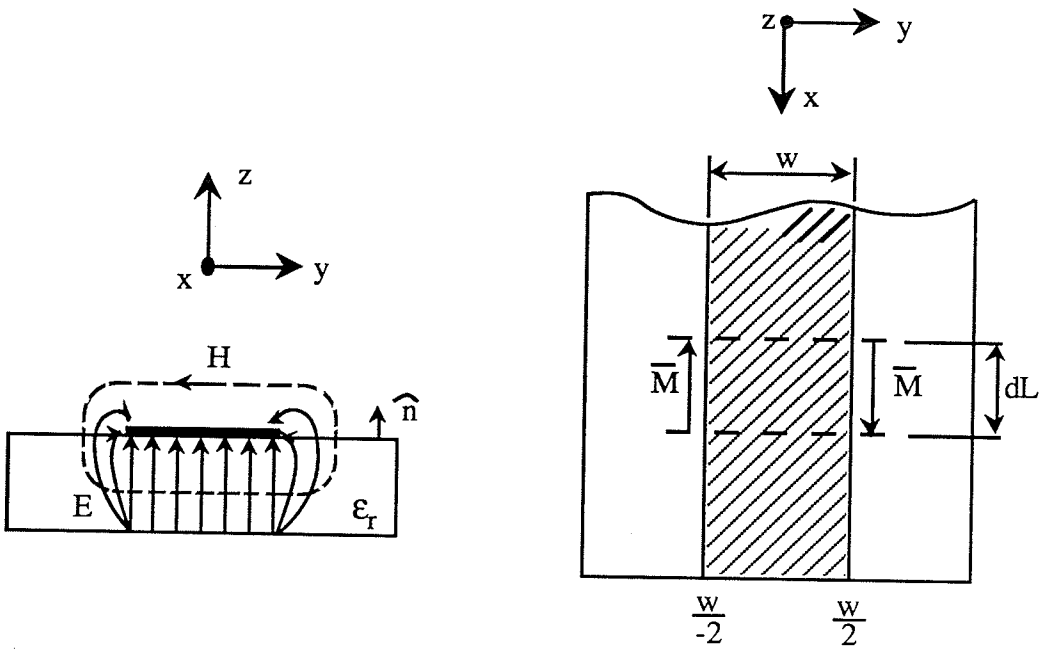

(a) Field distribution

(b) Straight line

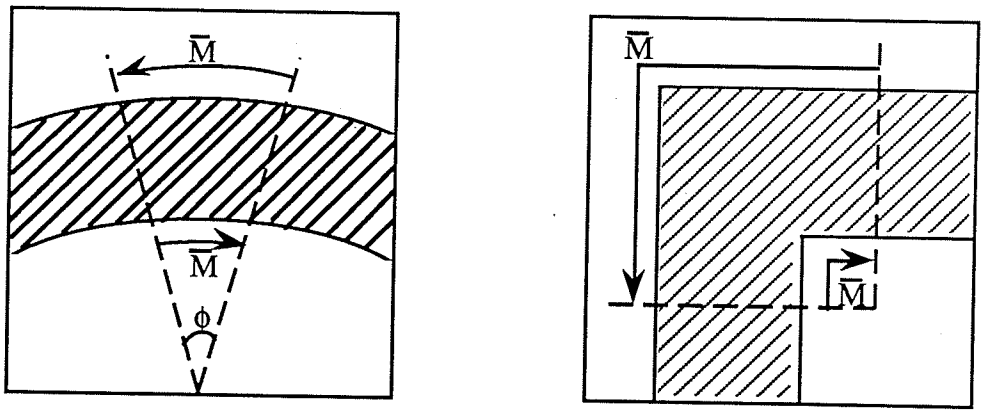

(c) Curved line

(d) Right-angle bend

Fig. 4.2 : Magnetic current distributions of microstrip lines.

The TEM mode field distribution may be represented in terms of current sources by equations 4.1(a) and (b)

$$\overline{M} = \overline{E} \times \hat{n} \tag{4.1 a}$$

$$\overline{I} = \hat{n} \times \overline{H} \tag{4.1 b}$$

where $\overline{M}$ is the magnetic current source

$\overline{I}$ is the electric current source

$\hat{n}$ is a unit vector normal to the surface

Thus a microstrip line may be represented by two current sources. However, the uniqueness theorem implies that only one source is necessary to observe the effects on the radiation field. Applying equation 4.1(a) to a portion of a straight microstrip line as shown in figure 4.2(a) yields magnetic currents of

$$\overline{M} = \overline{E} \times \hat{n}$$

where $\hat{n} = 1\,\hat{z}$ and

$$\overline{E} = E_z \hat{z} \quad , \quad -\frac{w}{2} \le x \le \frac{w}{2}$$

$$\overline{E} = -E_y \hat{y} + E_z \hat{z} \quad , \quad x > \frac{w}{2}$$

$$\overline{E} = E_y \hat{y} + E_z \hat{z} \quad , \quad x < \frac{-w}{2}$$

$$\therefore \overline{M} = 0 \quad , \quad -\frac{w}{2} \le x \le \frac{w}{2}$$

$$\overline{M} = -E_y \hat{x} \quad , \quad x > \frac{w}{2}$$

$$\overline{M} = E_y \hat{x} \quad , \quad x < \frac{-w}{2}$$

These are shown in figure 4.2(a) for a portion of the line dL. As can be seen, the fringing fields create magnetic currents on each side of the microstrip line, equal in magnitude but 180^{o} out of phase. This causes field cancellations and thus radiation is minimal for straight

microstrip lines. Figures 4.2(b) and (c) show two microstrip discontinuities which are used in the antenna design to follow. Here it can be seen that the curve and right angle bend produce a longer magnetic current on the outside edge of the line then the current on the inside. This imbalance permits radiation at these areas since there is not complete cancellation. The large impedance bandwidth associated with a traveling wave antenna was the major factor in selecting this type of structure as a MMIC compatible radiating element. The design goals were to develop a unit on a thin Alumina substrate that would operate with a large bandwidth and generate a circular polarized radiation pattern.

4.2 Traveling Wave Antenna Design

The design goal first considered was the aspect of circular polarization. This may be achieved by using two excitation feeds on a linearly polarized antenna [38] or by shaping the microstrip line. A single feed mechanism is preferred because it is less complex then a dual feed system. The microstrip line is shaped such that the components of the radiated field will be equal in magnitude and 90^{o} out of phase. If this condition is satisfied, then circular polarization will result. (see Appendix A.) An approach is outlined in [38] and has been applied to a travelling wave structure. A circular loop was studied in [38] using a continuous radiating current of the form

$$I_n = a_n \cos n\phi' + b_n \sin n\phi' \ \hat{\phi} \quad , \qquad n > 0 \tag{4.2}$$

which produce the following far field patterns;

$$E_\theta = f_n(\theta) \left[a_n \sin n\phi - b_n \cos n\phi \right] \tag{4.3 a}$$

where

$$f_n(\theta) = \frac{-\omega \mu a}{4} \frac{e^{-jkr}}{r} j^n \cos\theta \left[J_{n+1}(k a \sin\theta) + J_{n-1}(k a \sin\theta) \right] \tag{4.3 b}$$

and

$$E_\phi = g_n(\theta)\,[\,a_n \cos n\phi + b_n \sin n\phi\,] \tag{4.4 a}$$

where

$$g_n(\theta) = \frac{-\omega\mu a}{4}\frac{e^{-jkr}}{r} j^n\left[J_{n+1}(k a \sin\theta) - J_{n-1}(k a \sin\theta)\right] \tag{4.4 b}$$

See Appendix B for derivation of these equations

It was found that selecting $a_n = 1$ and $b_n = j$ equation (4.2) produced conditions suitable for obtaining circular polarization. Substituting these values into equation (4.2), (4.3 a) and (4.4 a) reduces the current to

$$I_n = e^{jn\phi'} \tag{4.5}$$

and the far fields to

$$E_\theta = f_n(\theta)\, e^{j\left(n\phi - \frac{\pi}{2}\right)} \tag{4.6}$$

$$E_\phi = g_n(\theta)\, e^{jn\phi} \tag{4.7}$$

Thus, equations (4.6) and (4.7) show the two field components 90° out of phase, but with unequal magnitudes. This condition would result in elliptically polarized waves, however, circular polarization can be attained if the magnitudes are equal. Examining equation (4.3 b) and (4.4 b) show that the two field magnitudes are dependent upon n and a. Proper selection of n will produce a broadside pattern, i.e. maximum radiation on loop axis, $\theta = 0^\circ$. The argument of the bessel function at $\theta = 0^\circ$ is zero. Thus, only n=1, which produces a zero order bessel function, will generate a broadside pattern since

$$J_m(0) = 1 \qquad \text{for } m = 0$$

$$J_m(0) = 0 \qquad \text{for } m \geq 1$$

All other values of n produce higher order bessel functions resulting in $f_n(0^o) = gn(0^o) = 0$, i.e. producing a pattern null on the loop axis. With the selection of n=1, it can be seen that the two magnitudes are dependent only upon the loop radius. Equating (4.3 b) to (4.4 b) yields

$$f_n(\theta) = g_n(\theta)$$

$$\frac{-\omega \mu a}{4} \frac{e^{-jkr}}{r} j^n \cos\theta \left[J_2(k a \sin\theta) + J_0(k a \sin\theta)\right] =$$

$$\frac{-\omega \mu a}{4} \frac{e^{-jkr}}{r} j^n \left[J_2(k a \sin\theta) - J_0(k a \sin\theta)\right]$$

which simplifies to

$$\cos\theta \left[J_2(k a \sin\theta) + J_0(k a \sin\theta)\right] = \left[J_2(k a \sin\theta) - J_0(k a \sin\theta)\right] \qquad (4.8)$$

Selecting a loop radius to satisfy equation (4.8) will generate equivalent field magnitudes. Therefore the radiation pattern will be circular polarized with an appropriate loop radius and the excitation previously indicated.

To obtain circular polarization, a radiating current in the form of equation (4.5) is required. Breaking up the radiating current into discrete elements is one variation [38]. This is shown in equation (4.9).

$$I_n = I \Delta l \sum_{m=1}^{M} e^{j\delta_m} \qquad (4.9)$$

with $\sum_{m=1}^{M} \delta_m = n\, 2\pi$

where $I\Delta l$ is the discrete current element

M is the total number of elements

δ_m is the phase of each element

Equations (4.6) and (4.7) show that the phase progresses as $n2\pi$, hence the condition of $\sum_{m=1}^{M} \delta_m = n\,2\,\pi$ was stipulated in order to satisfy the conditions of a loop. For broadside radiation, $n = 1$ is required, thus the total phase progression due to all discrete radiating current sources must be 2π. Deviations from 2π will result in a pattern with a null at the loop axis. Thus a circularly polarized broadside pattern may be obtained by placing discrete radiating current elements in a loop with an appropriate radius as discussed previously.

Note that the gain of this antenna is also a function of the loop radius. The maximum possible gain of this circular loop would occur when all the energy uniformly illuminates the circular aperture area. The equation relating these is given in [40] as

$$G_{max} = \frac{4\pi A}{\lambda^2} \tag{4.10}$$

where A is the aperture area

Equation (4.10) clearly shows that as the loop radius increases, the gain increases as well.

An antenna with discrete radiating currents can be realized with a traveling wave microstrip antenna. The segment lengths are selected such that the radiated pattern will be broadside. This may be accomplished by using segment lengths which have a total phase progression of 2π. Each segment placed in a circular array can be connected with a line which is one wavelength long. This line acts as a delay between each element , thus there will be a progressive phase change along the radiating circumference. A general structure based upon this theory is illustrated in figure 4.3.

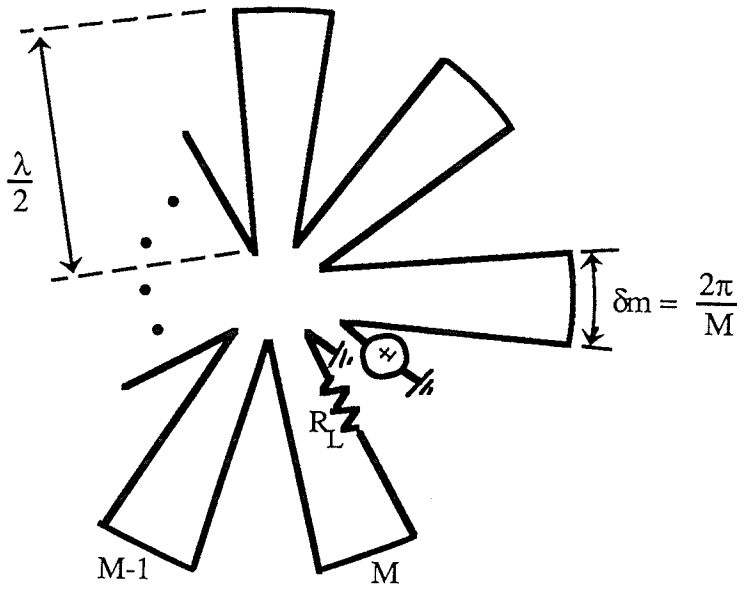

Fig. 4.3 : Circular polarized traveling wave antenna

Three structures were analyzed using the computer modelling program NEC (Numerical Electromagnetic Code) [14]. The antenna was modelled as a wire structure and the moment method technique was applied to the electric field integral equation which describes the antenna. The antenna can be divided into small segments on which the unknown current is expanded in a sum of basis functions with unknown coefficients. The current on each segment is represented by three functions as shown.

$$I = a_1 \sin k(s-s_j) + a_2 \cos k(s-s_j) + a_3$$

where s_j is the value of s at the centre of segment j

An impulse-type weighting function is applied to create a system of linear equations from which the unknown current coefficients a_1, a_2, and a_3 can be determined for each segment. The far field radiation pattern was determined based upon the calculated current distribution.

4.3 Analysis of Traveling wave Antenna

Three, four and eight arm traveling wave antenna structures were studied. Wire models were constructed and analyzed using NEC. These structures were located in free space above a ground plane. The effects of high relative permittivities could not be included in the analysis since NEC is limited to the case of free space, $\varepsilon_r = 1$. However, the absence of a dielectric substrate does not effect the relative current distributions on the structure nor the radiation pattern generated. In addition, the radiation efficiency can be observed due to the geometry of the antenna. Thus an analysis in free space can provide accurate information on the properties of each antenna.

4.3.1 3-Arm Antenna

The first traveling wave antenna studied is illustrated in figure 4.4. This structure has three radiating current segments along the outer circumference of the loop. Each segment is $\lambda/3$ in length and connected to each other by a line one wavelength long. The height above the ground plane is $\lambda/156$, which is the actual height when fabricated on a 10 mil thick alumina substrate. This height was chosen since MMICs are constructed on substrates with thicknesses of 10 to 25 mils. The structure is excited by a voltage source and terminated in a matched load along the last line length as shown. In reference to figure 4.3, the radiating current segments are indicated as A-B, C-D and E-F. The line lengths between each segment being 1λ result in the phase at point B being equal to the phase at point C, and likewise at points D and E. Thus the phase progression along these segments starting at point A with ϕ will end at point F with $\phi + 1\lambda$. This satisfies the condition for a broadside pattern.

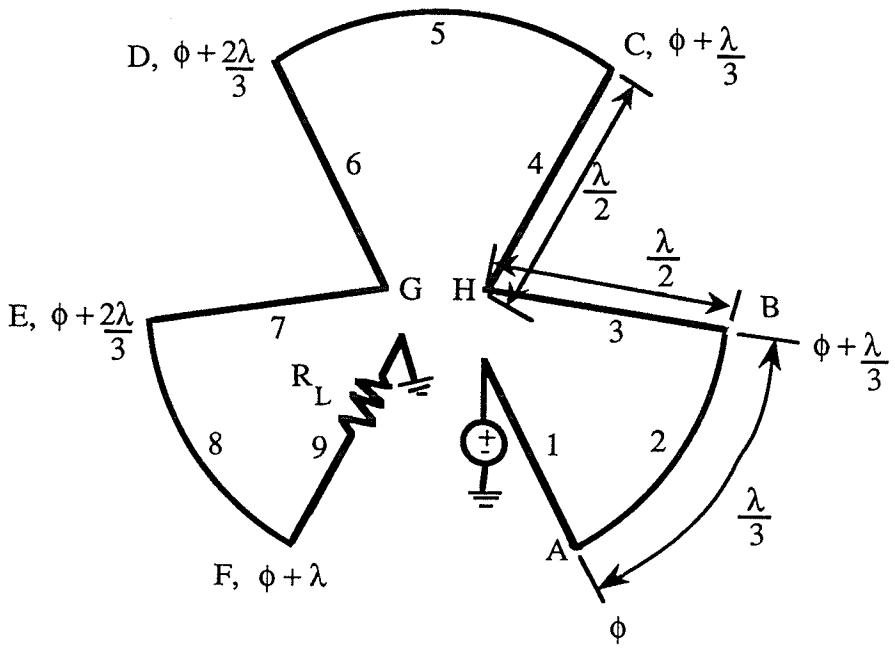

Fig. 4.4 : 3-arm traveling wave antenna

The radiation mechanisms are the discontinuities of the line. The dominant sources are the corners A, B, C, D, E and F and the outer circumference of the antenna. These form the primary aperture. A secondary aperture does exist at the center of the structure due to the corners G and H. However, the aperture is quite small in comparison to the outer circumference and hence has minimal influence on the performance of the antenna.

The loop radius was determined by satisfying equation (4.8). A loop radius of .208λ yields $f_n(\theta) \cong g_n(\theta)$ for $-40^o \leq \theta \leq 40^o$, at theta equal to $\pm 40^o$, $f_n = 1.04 g_n$. This would produce circular polarization over the range of theta. As illustrated in figure 4.4, the 1λ delay line is bent into two lengths connecting each outer segment. A radius of .208λ would require a major modification of this delay line such as shown in figure 4.5

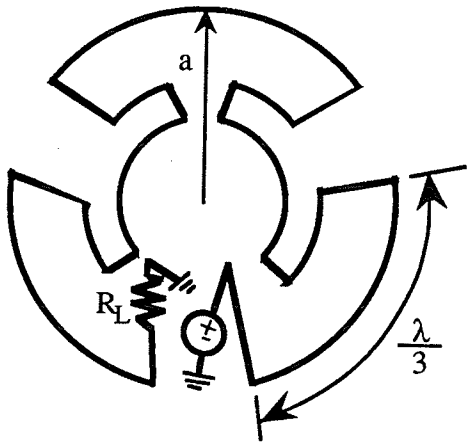

Fig. 4.5 : Possible geometry when $a < \lambda/2$

However, this type of configuration is more complex and increases the number of radiation mechanisms at the inner aperture. In addition, the separation distance between the two apertures decreases. Both these factors cause the inner aperture to have a stronger influence on the properties of the antenna, conceivably destructive. Thus a loop radius greater then $\lambda/2$ is preferred. However, the quality of circular polarization will degrade due to the deviation from satisfying equation (4.8). A loop radius approximately 0.6λ yields $f_n(\theta) \cong g_n(\theta)$ for $-15^o < \theta < 15^o$. The outer limits of this range have $f_n = 1.4g_n$. It is expected that the larger loop radius will generate circular polarization, but over a narrower beam width. The added advantage of a larger loop radius is the increase in gain due to the increased aperture size.

The structure in figure 4.4 was analyzed by the NEC computer program. The wire lengths were all determined for an operating frequency of 3 GHz , hence this was the first observation frequency. The current distribution of this structure is shown in figure 4.6 (a). The oscillations in the current distribution are accounted for by the abrupt geometrical

variations of the structure. It can be seen that the current attenuation along the structure is minimal. Due to the marginal attenuation, a low radiation efficiency of 8.9% existed. The phase of the current along the structure shows a progression of 2π along the outer segments from point A to F indicated in figure 4.4. The actual phase progression was 339.5^{o}. Nevertheless, it can be seen that the current characteristics indicate this to be a traveling wave structure. The radiation pattern and axial ratio were determined and are given in figures 4.6 (c) and (d). These plots indicate that a broadside pattern is generated which is circularly polarized having an axial ratio less than 3 dB for $-40^{o} < \theta < 28^{o}$. The 3 dB beamwidth for this antenna is 40^{o}. The computer analysis confirmed the expected characteristics of this type of antenna. A frequency sweep was performed to determine the variations in the pattern and input impedance such that these bandwidths could be evaluated. The radiated patterns for various frequencies between 2.25 GHz and 3.25 GHz are illustrated in figure 4.7. The pattern at f = 2.25 GHz shows a null at the center. This is expected as the phase progression is no longer 2π. At frequencies below f_o, the phase progression will be less than 2π while at higher frequencies the phase progression will be greater than 2π . It has been shown that progressions other than 2π cause a null at the center of the pattern. It can also be seen that the radiated main beam squints towards $\theta > 0^{o}$ for lower frequencies and tracks to $\theta < 0^{o}$ for higher frequencies. This phenomenon is associated with traveling wave antennas. The upper and lower frequencies used to determine the bandwidth are identified by f_U and f_L respectively. The structures modelled using NEC have the E-plane pattern taken at $\phi = 90^{o}$, where the source lies in this plane. It should be mentioned at this point that this corresponds to an experimental pattern measurement taken at $\phi = 0^{o}$, with respect to the experimental coordinate system.

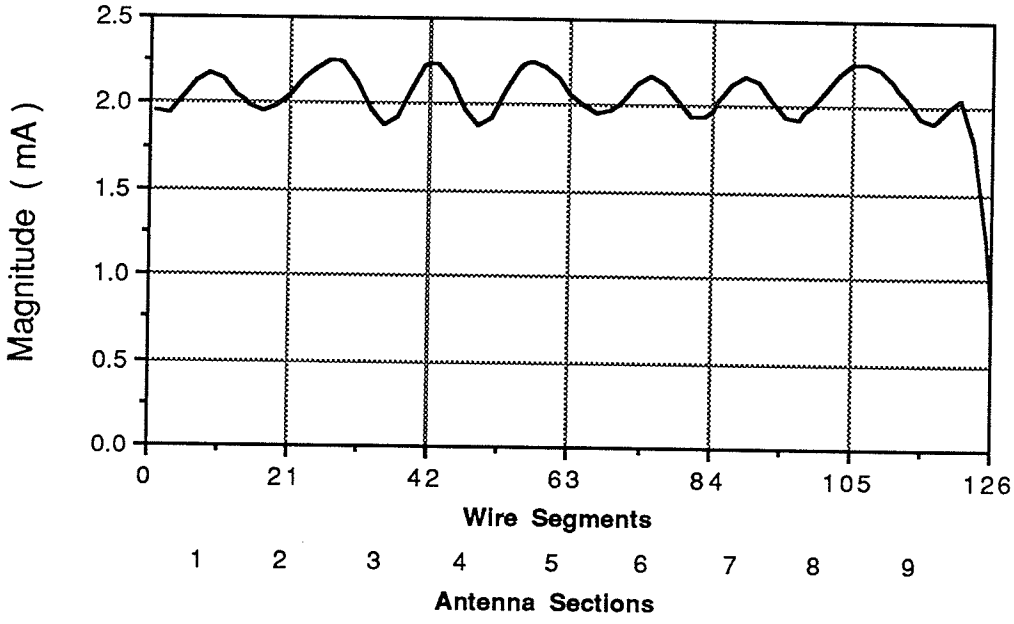

Fig. 4.6 a) : Current magnitude distribution of a 3-arm antenna, f_o = 3 GHz.

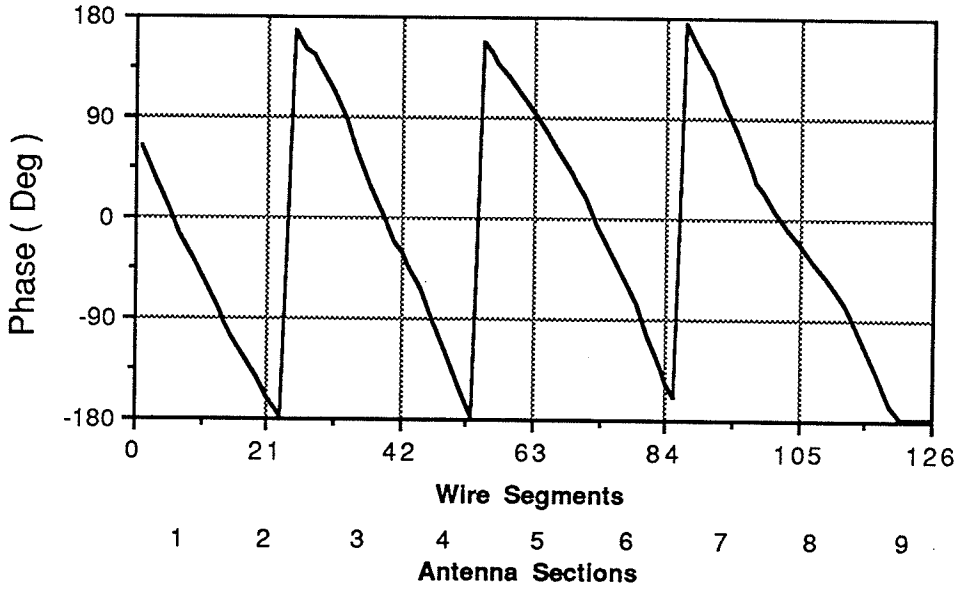

Fig. 4.6 b) : Current phase distribution of a 3-arm antenna, f_o = 3 GHz

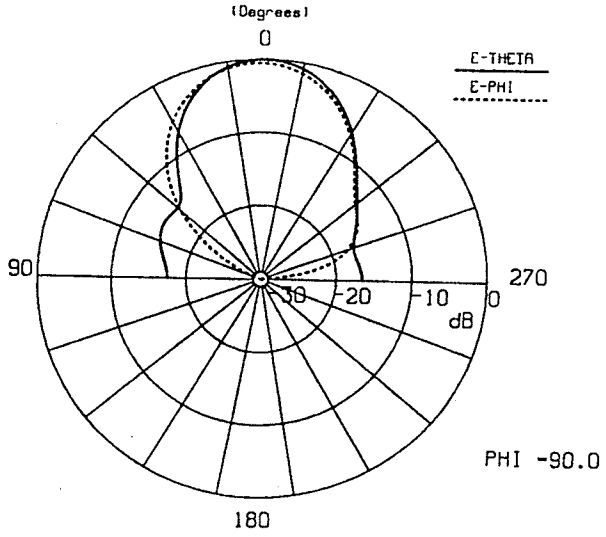

Fig. 4.6 c) : Radiation pattern of 3-arm antenna, $f_o = 3$ GHz, E–plane

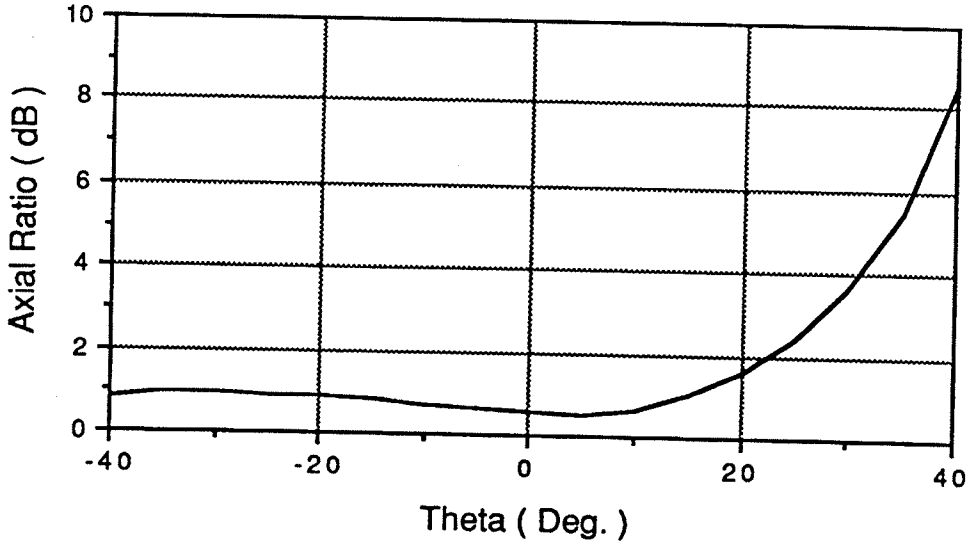

Fig. 4.6 d) : Axial ratio of 3-arm antenna, $f_o = 3$ GHz

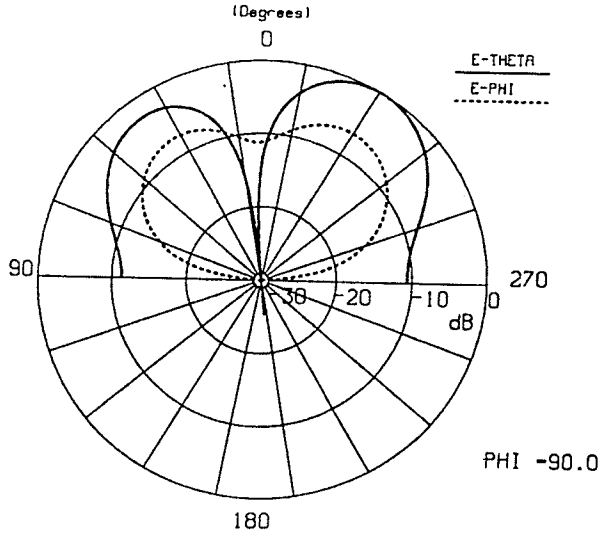

(a) f = 2.25 GHz

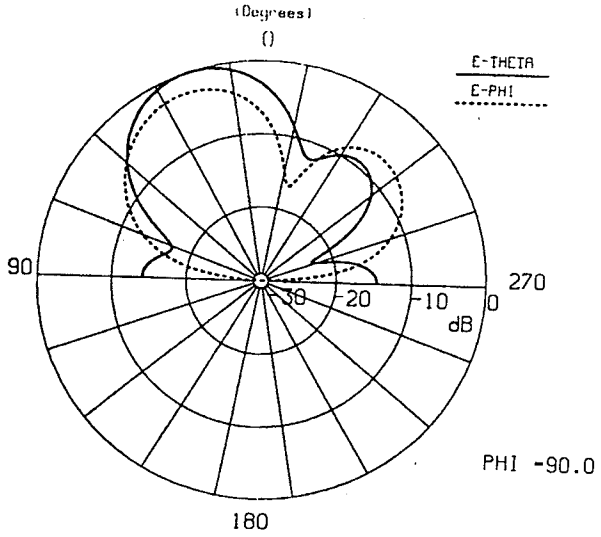

(b) f = 2.5 GHz = f_L

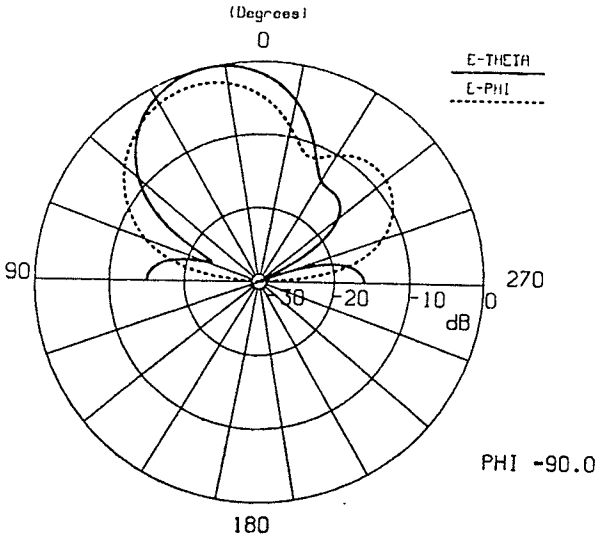

(c) f = 2.6 GHz

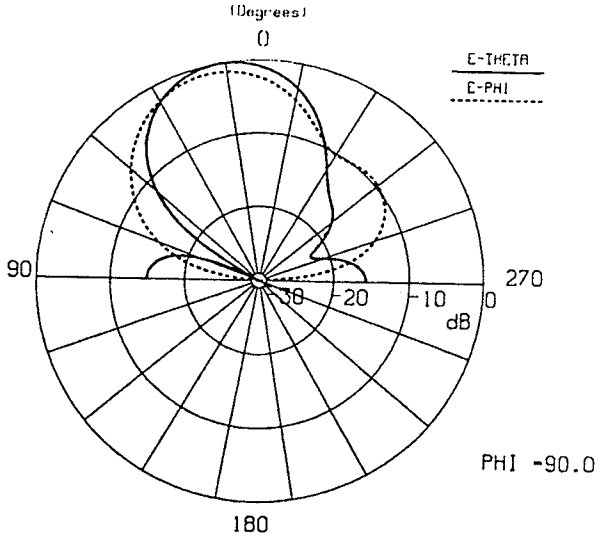

(d) f = 2.7 GHz

Fig. 4.7 : Frequency sweep of 3-arm antenna, E-plane

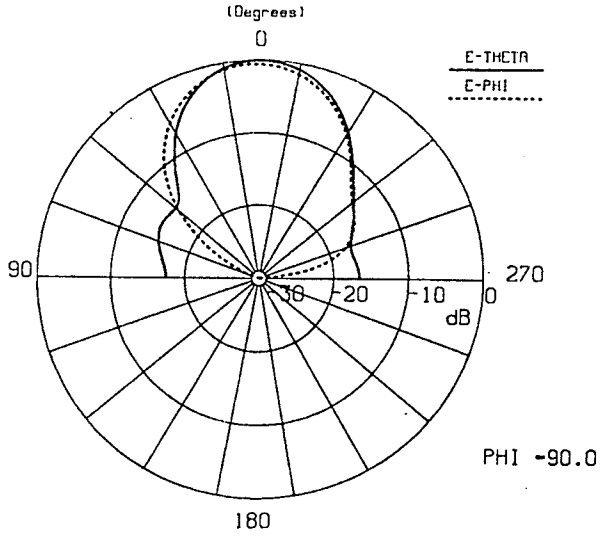

(e) $f = f_o = 3.0$ GHz

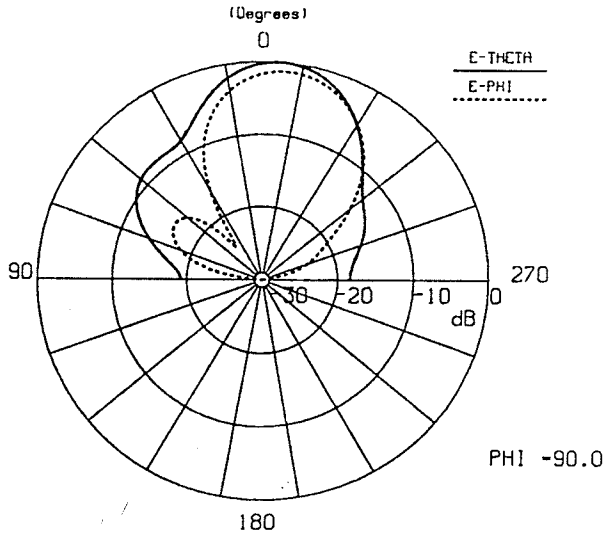

(f) $f = 3.2$ GHz

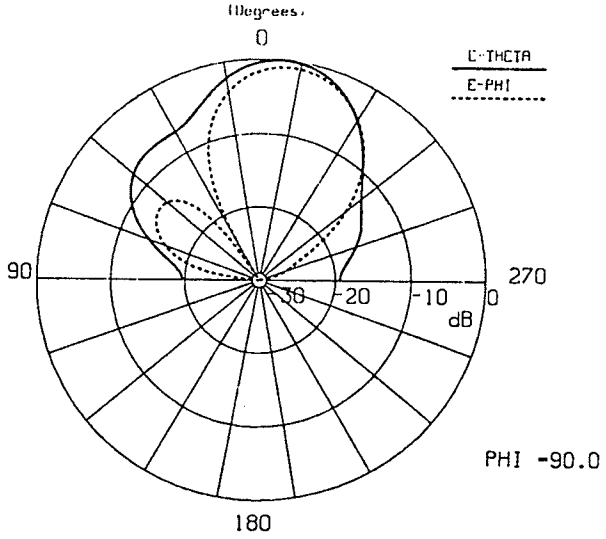

(g) $f = 3.25$ GHz $= f_U$

Fig. 4.7 (cont.)

The input impedance was also observed over the frequency sweep. This is plotted in figure 4.8 (a) and shows that the impedance remains constant over this range of

frequencies. This yields a BW_{Zin} of 30 %. Figure 4.7 shows that the pattern bandwidth will be the limiting factor of operation over a frequency range. For this structure, BW_{pat} = 25 %. The radiation efficiency and peak gain has also been plotted over this frequency range. Figure 4.8(b) shows relatively constant efficiency over the frequency range but with a maximum gain at f = 3 GHz.

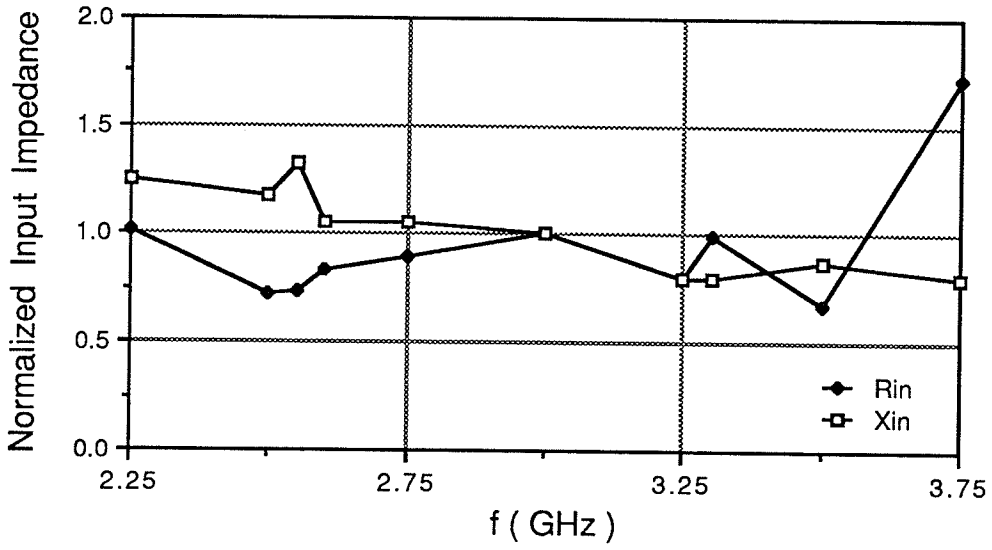

Fig. 4.8 a) : Input impedance of 3-arm antenna normalized to Z_{in} at f = 3 GHz

$Z_{in_{3\ GHz}}$ = 133-j454 Ω

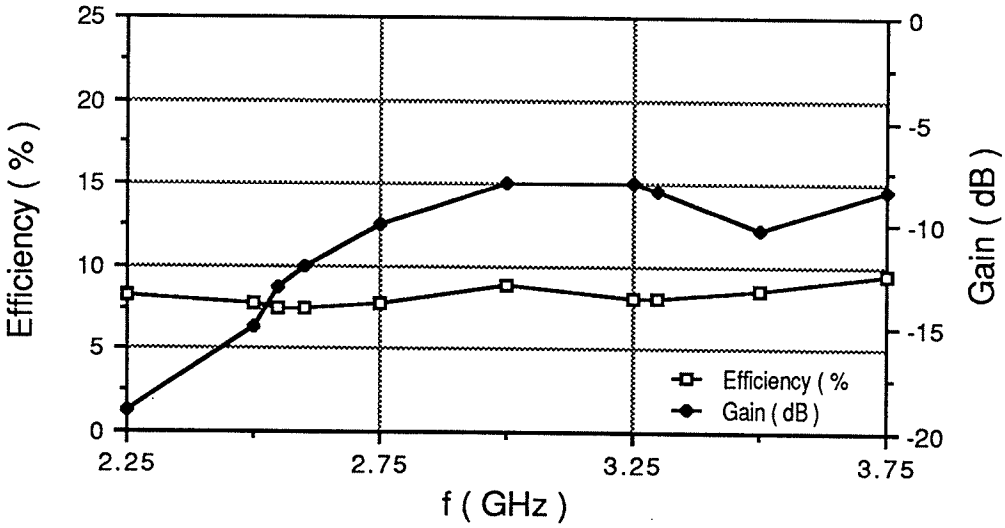

Fig. 4.8 b) : Radiation efficiency and gain of the 3-arm antenna

This structure has many favorable characteristics except for its low radiation efficiency and hence gain. The number of arms was increased to eight in order to improve these factors.

4.3.2 8-arm antenna

To improve the efficiency, the structure shown in figure 4.9 was analyzed.The increased number of discontinuities should increase the amount of radiated energy. Setting the lengths of the outer segments to $\lambda/8$ will provide the necessary phase progression for a broadside pattern. The outer radius remained the same as the 3-arm antenna.

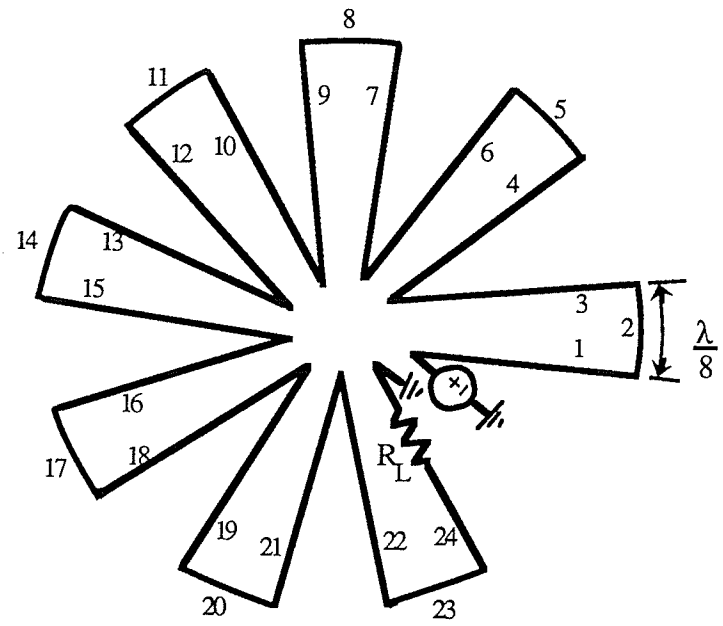

Fig. 4.9 : 8-arm traveling wave antenna

At the operating frequency of 3 GHz , the current distribution was seen to attenuate more so than the 3-arm case. This resulted in a radiation efficiency of 15.5 %, an

improvement over the 3-arm case by a factor of 1.74. In addition, the magnitude of the current oscillations increased due to the increased discontinuities. Both these characteristics can be seen in figure 4.10 (a). The computed radiation pattern and axial ratio are given in figures 4.10 (b) and (c). They show a broadside pattern with an axial ratio less than 3 dB for $-12^{o} < \theta < 21^{o}$ and a 3 dB beamwidth of 40^{o}.

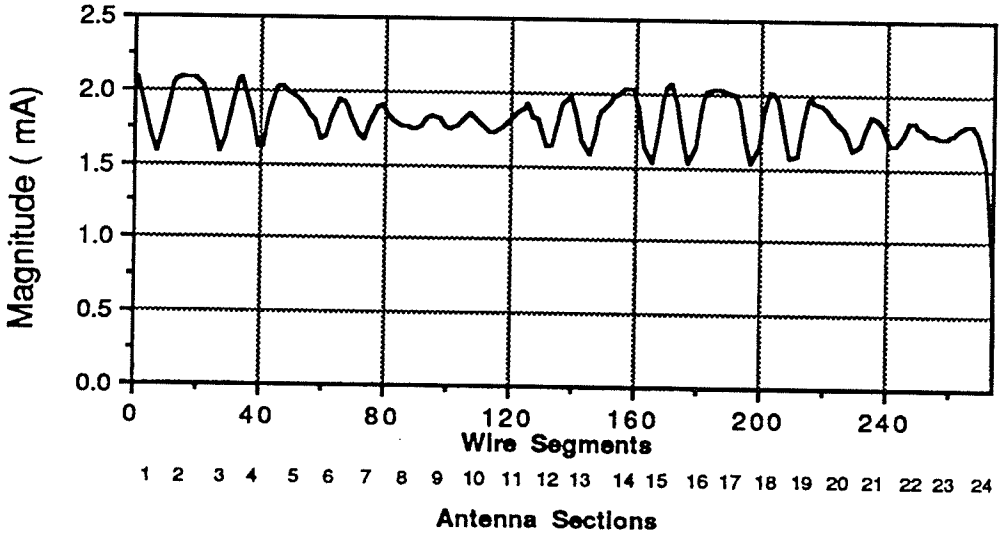

Fig. 4.10 a) : Current magnitude distribution of an 8-arm antenna, f_o = 3 GHz

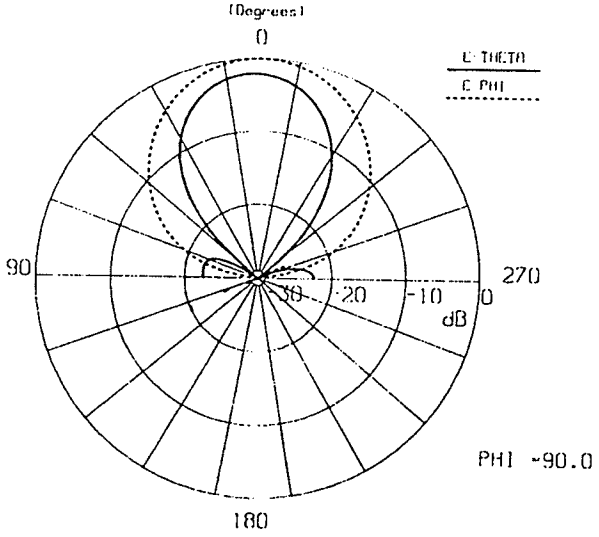

Fig. 4.10 b) : Radiation pattern of 8-arm antenna, f_o = 3 GHz, E–plane

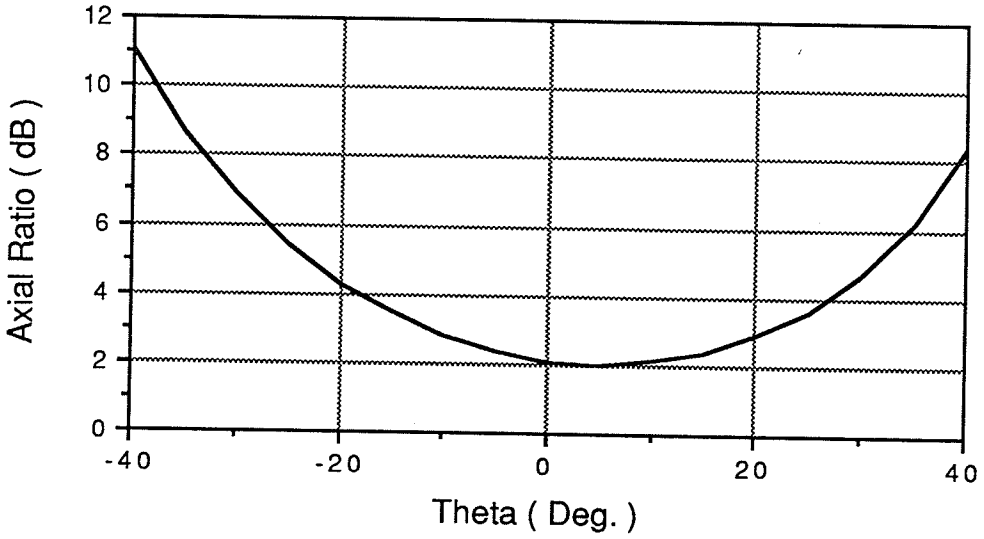

Fig. 4.10 c) : Axial ratio of 8-arm antenna, f_o = 3 GHz.

A frequency sweep from 2.75 GHz to 3.75 GHz was performed to determine the bandwidth of this structure. The impedance remained fairly constant while the patterns varied over this range. Figure 4.11 shows the progression from a null centered pattern to broadside and then back to a null centered pattern as the frequency approaches and exceeds the operating frequency. This yields a pattern bandwidth of 11.7 %. Figures 4.12(a) and (b) show the variations in impedance, efficiency and gain over this frequency range. The input impedance bandwidth has been determined to be approximately 28.0 %.

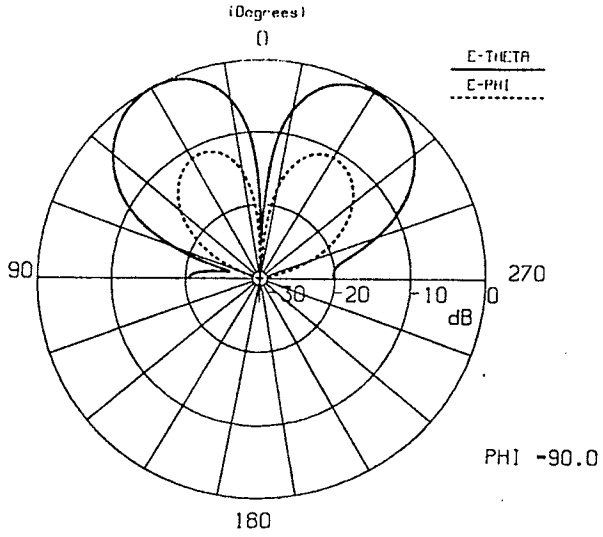

(a) f = 2.75 GHz

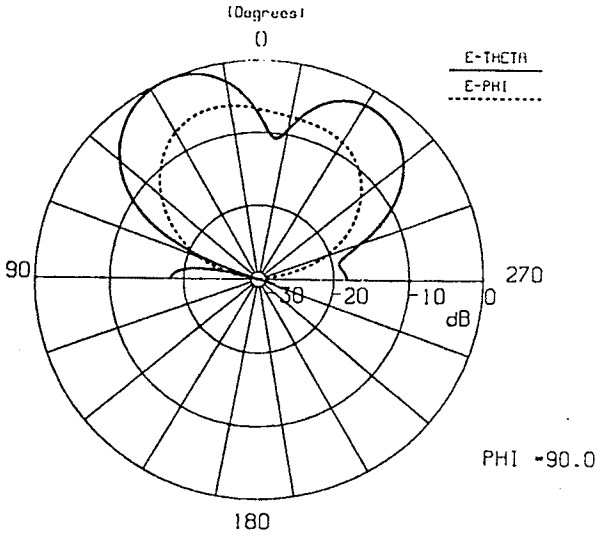

(b) f = 2.8 GHz

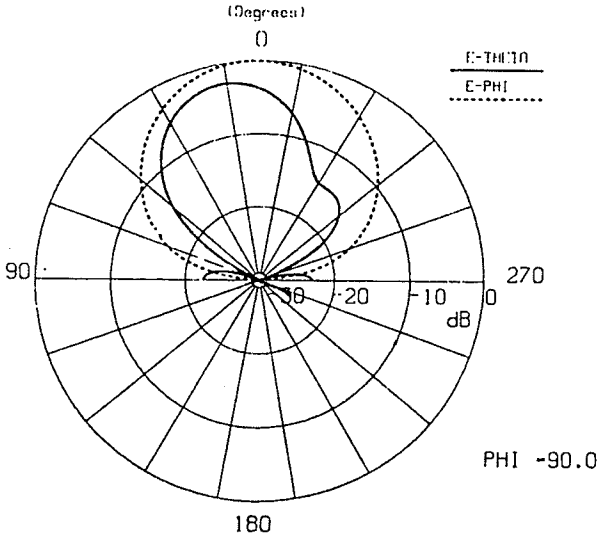

(c) f = 2.9 GHz = f_L

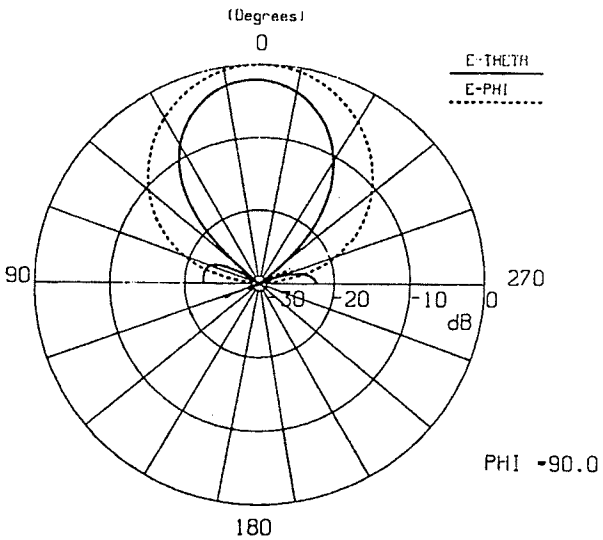

(d) f = f_o = 3.0 GHz

Fig. 4.11 : Frequency sweep of 8-arm antenna

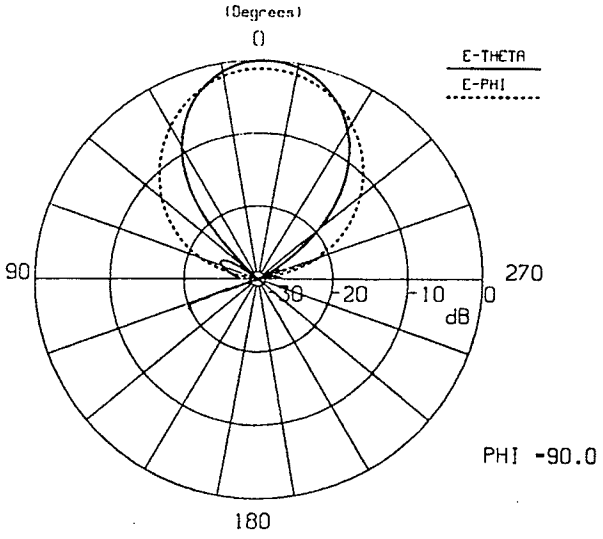

(e) f = 3.1 GHz

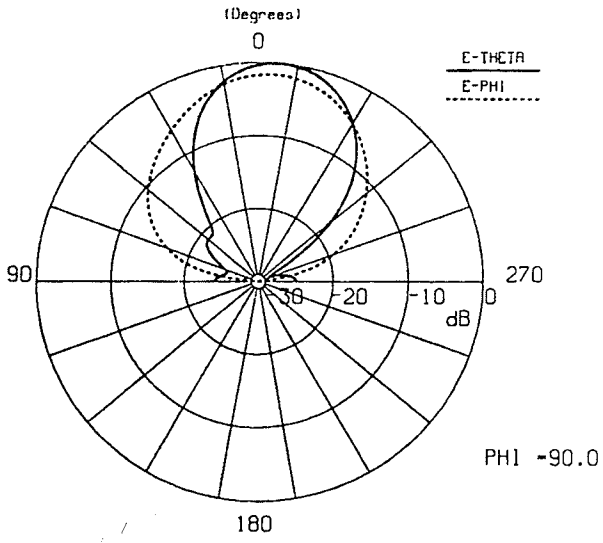

(f) f = 3.2 GHz

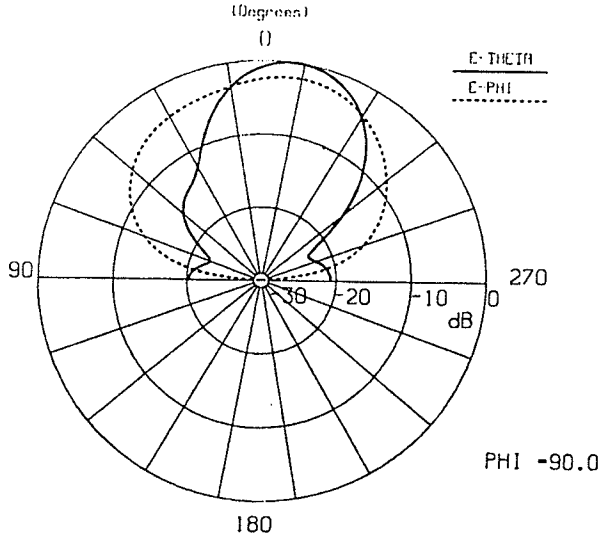

(g) f = 3.25 GHz = f_U

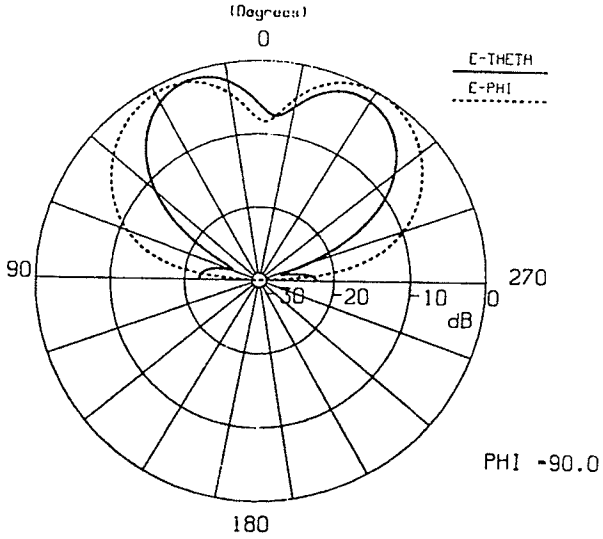

(h) f = 3.5 GHz

Fig. 4.11 (cont.)

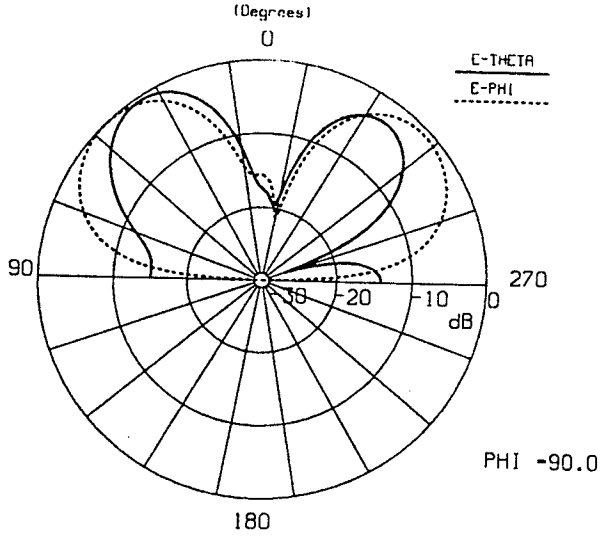

(i) f = 3.75 GHz

Fig. 4.11 (cont.)

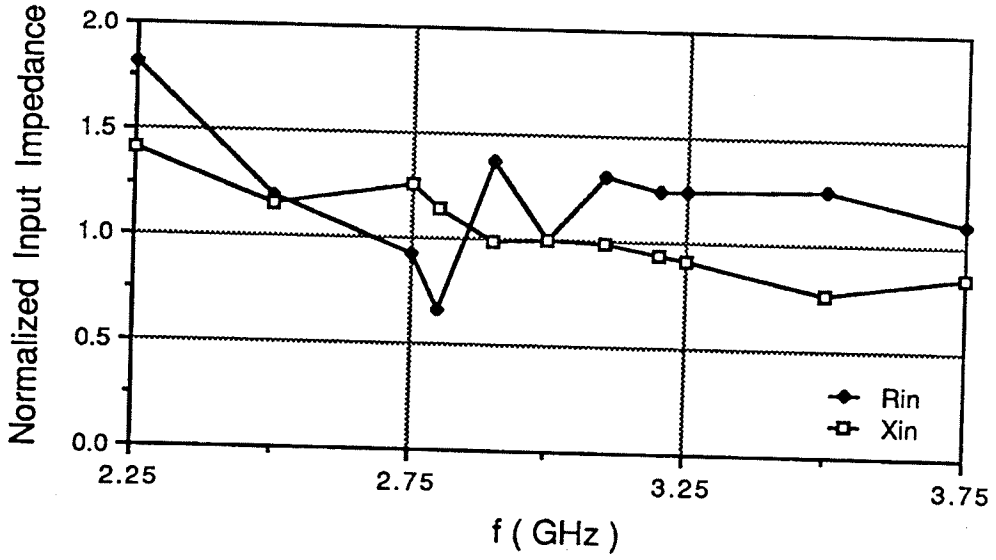

Fig. 4.12 a) : Input impedance of the 8-arm antenna normalized to Z_{in} at f = 3 GHz
Zin3 GHz = 94.3-j439 Ω

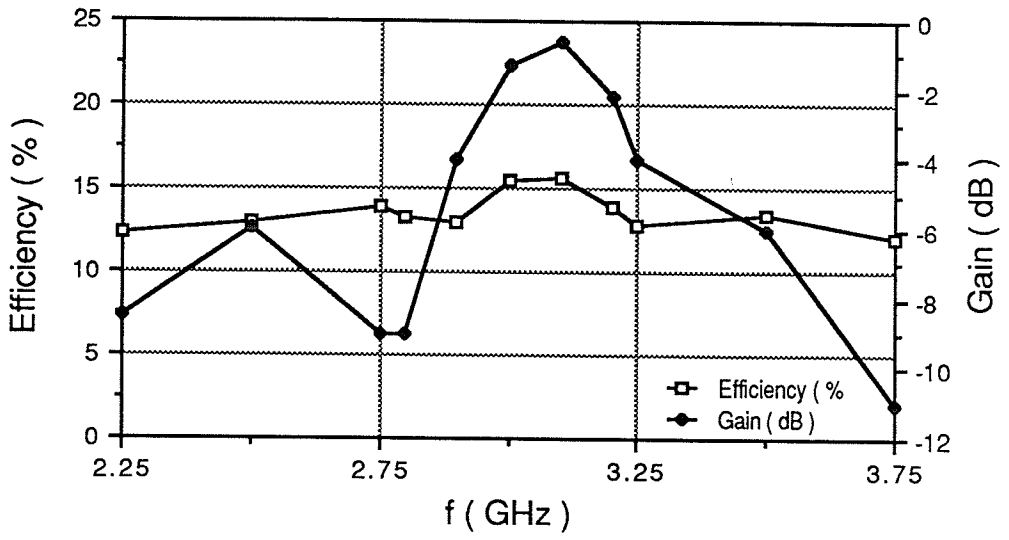

Fig. 4.12 b) : Radiation efficiency and gain of the 8-arm antenna

It is important to note that although the efficiency has been improved, the cost has been that the pattern bandwidth has been reduced significantly. This reduction is due to the increase in the total wire length. As frequency changes, the electrical lengths of each arm vary, thus changing the progressive phase. This phase error is cumulative, hence the 3-arm structure has less of a phase error than the 8-arm structure at each frequency. A significant error occurs when a center-null begins to occur in the pattern. This results in structures with few arms being less frequency sensitive than structures with more arms. A compromise between the efficiency and bandwidth was a structure with four arms.

4.3.3 4-arm antenna

The 4-arm structure shown in figure 4.13 was designed using the same principles as before. The current distribution, radiated pattern, and axial ratio are given in figure 4.14 for $f = f_0 = 3$ GHz.

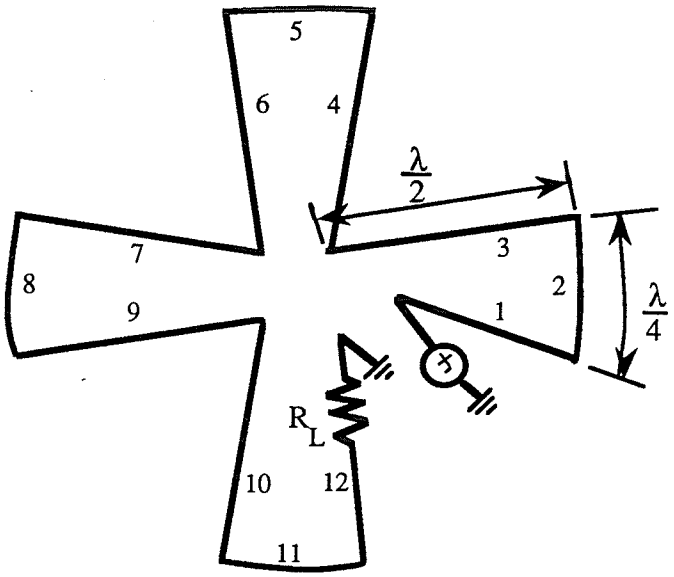

Fig. 4.13 : 4-arm traveling wave antenna

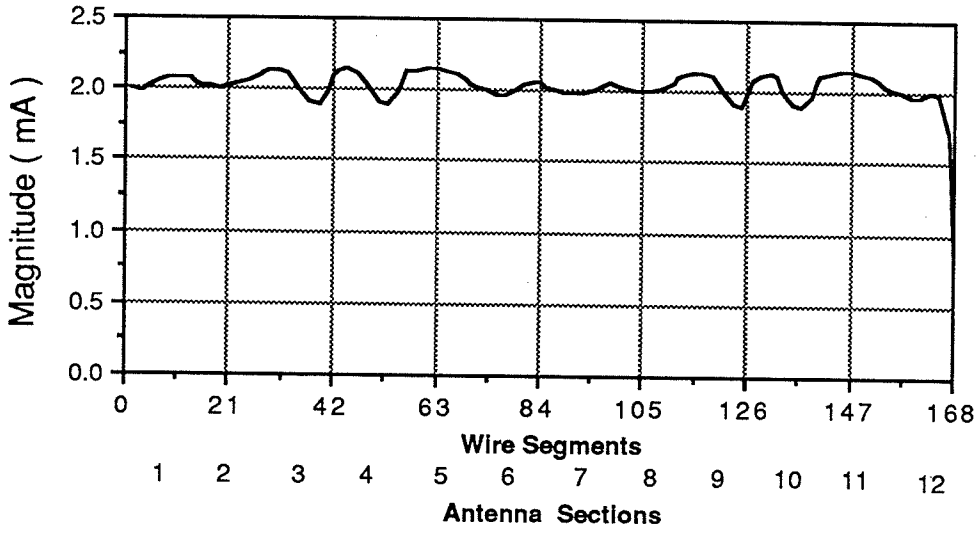

Fig. 4.14 a) : Current magnitude distribution of a 4-arm antenna, $f_o = 3$ GHz

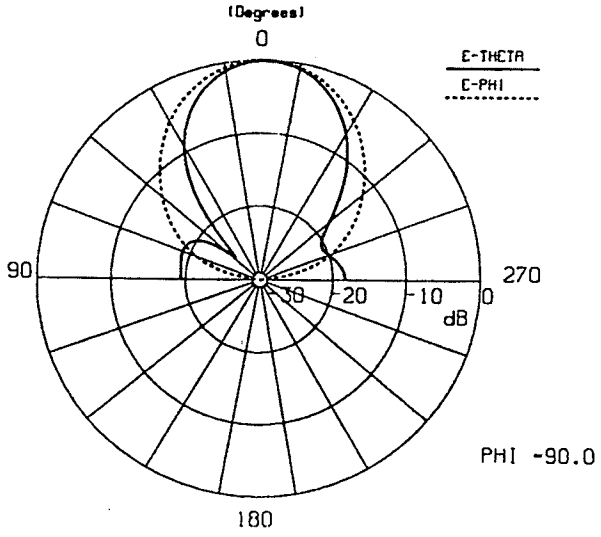

Fig. 4.14 b) : Radiation pattern of a 4-arm antenna, f_o = 3 GHz, E-plane

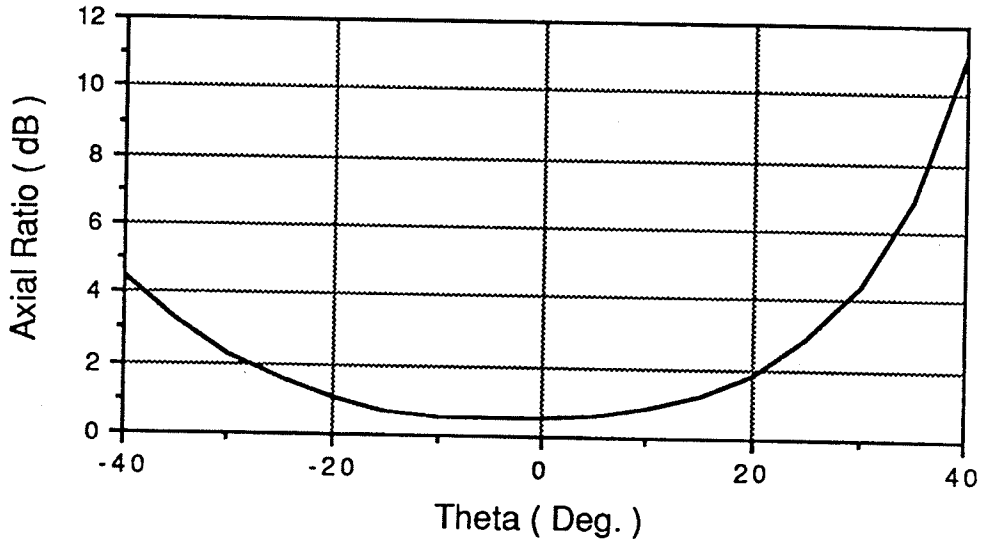

Fig. 4.14 c) : Axial ratio of 4-arm antenna f_o = 3 GHz

This structure had a radiation efficiency of 9.5%. The pattern had an axial ratio less than 3 dB for $-34^{o} < \theta < 25^{o}$ and a 3 dB beamwidth of 40^{o} . A frequency sweep from 2.5 GHz to 3.5 GHz yielded $BW_{Zin} \cong 20$ % and $BW_{pat} = 23.3\%$. These were determined from the results shown in figures 4.15 and 4.16.

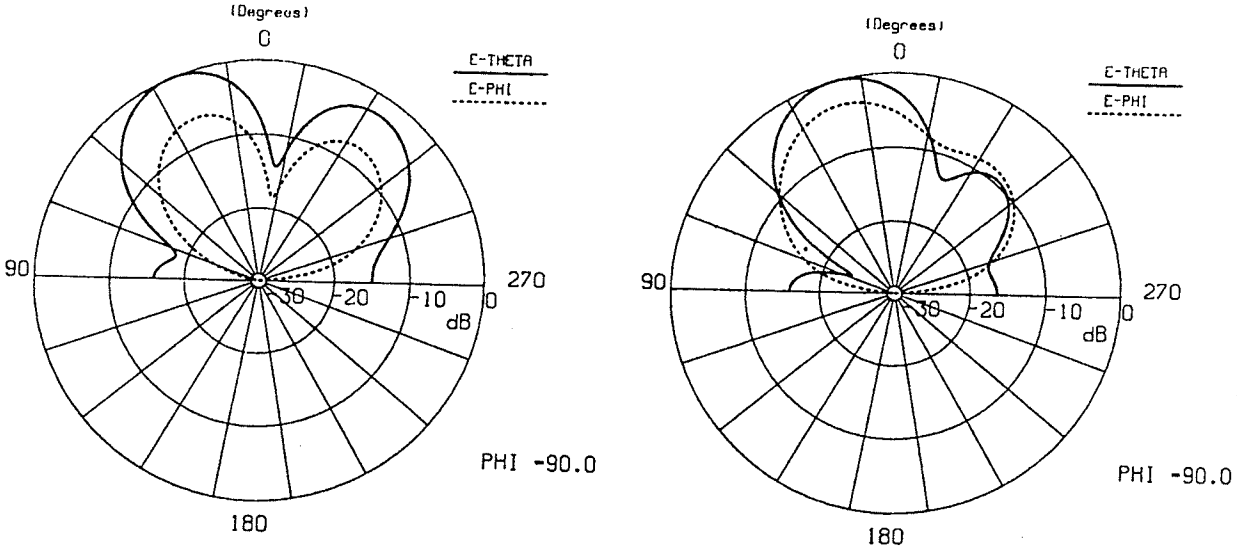

(a) f = 2.5 GHz

(b) f = 2.6 GHz = f_L

Fig. 4.15 : Frequency sweep of 4-arm antenna, E-plane

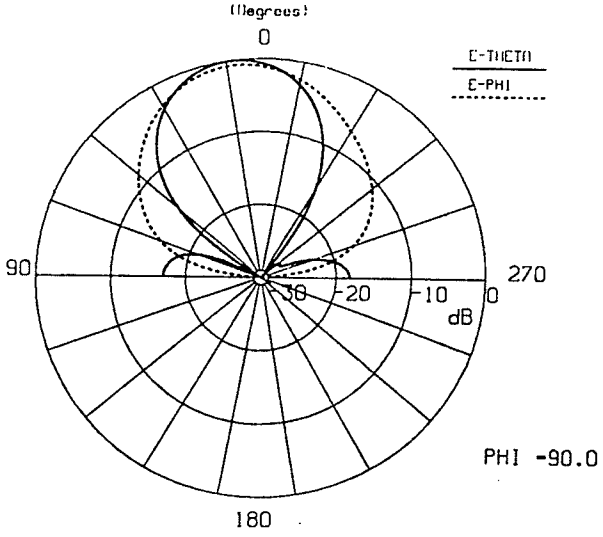

(c) f = 2.75 GHz

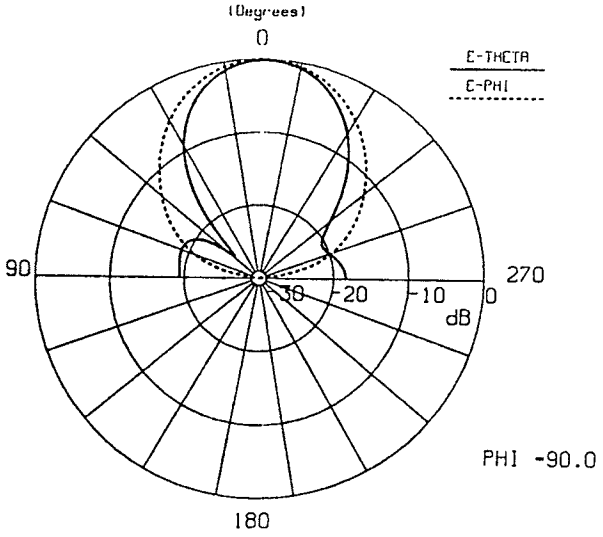

(d) $f = f_o = 3.0$ GHz

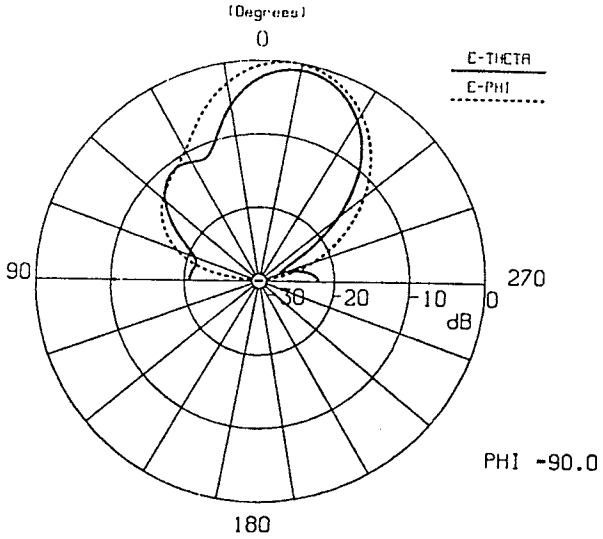

(e) f = 3.25 GHz

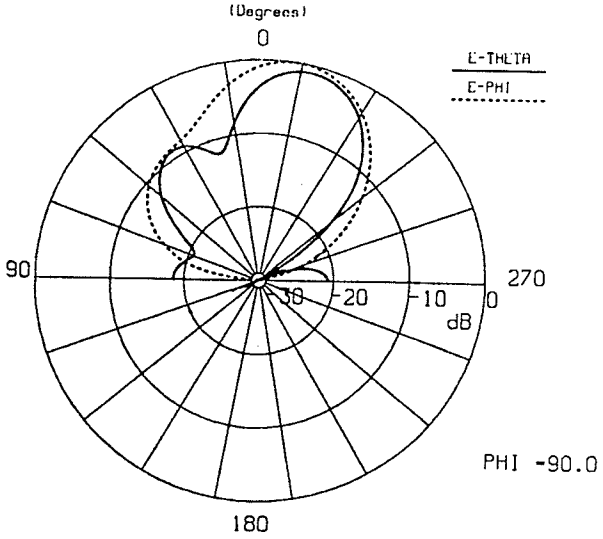

(f) $f = 3.3 \text{ GHz} = f_U$

Fig. 4.15 (cont.)

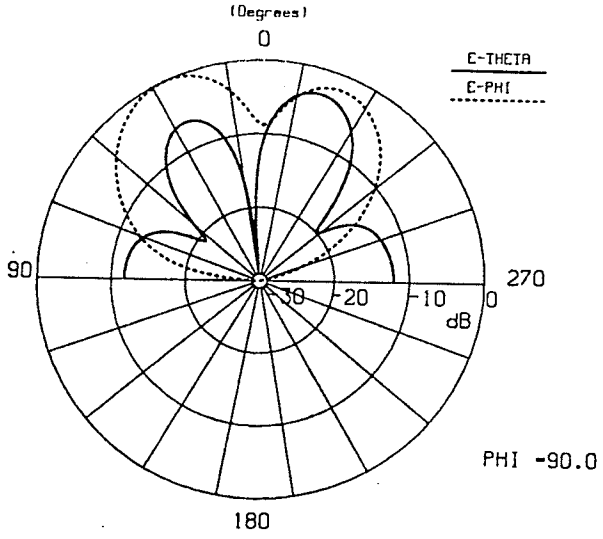

(g) f = 3.5 GHz

Fig. 4.15 (cont.)

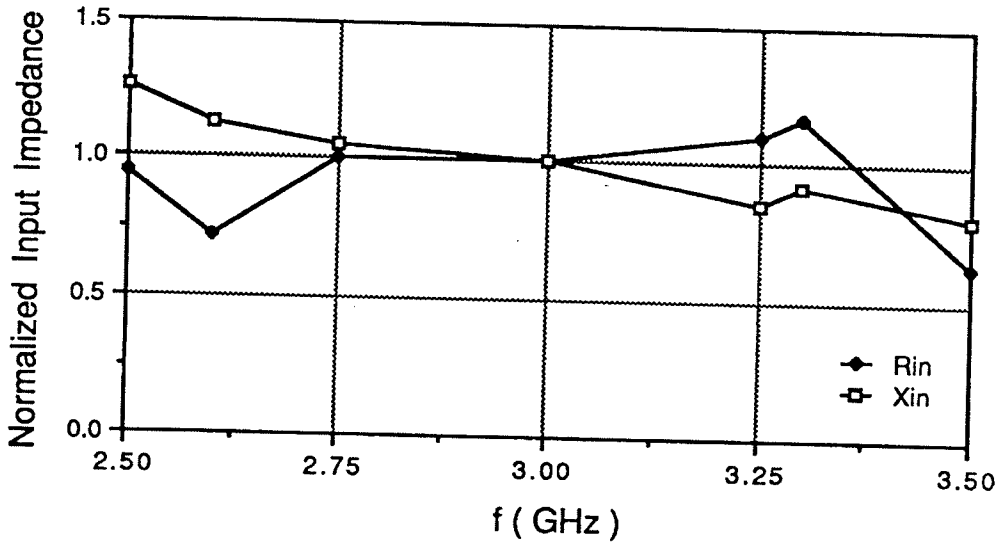

Fig. 4.16 a) : Input impedance of 4-arm antenna normalized to Z_{in} at f = 3 GHz

$Z_{in_{3\ GHz}} = 127\text{-}j450\ \Omega$

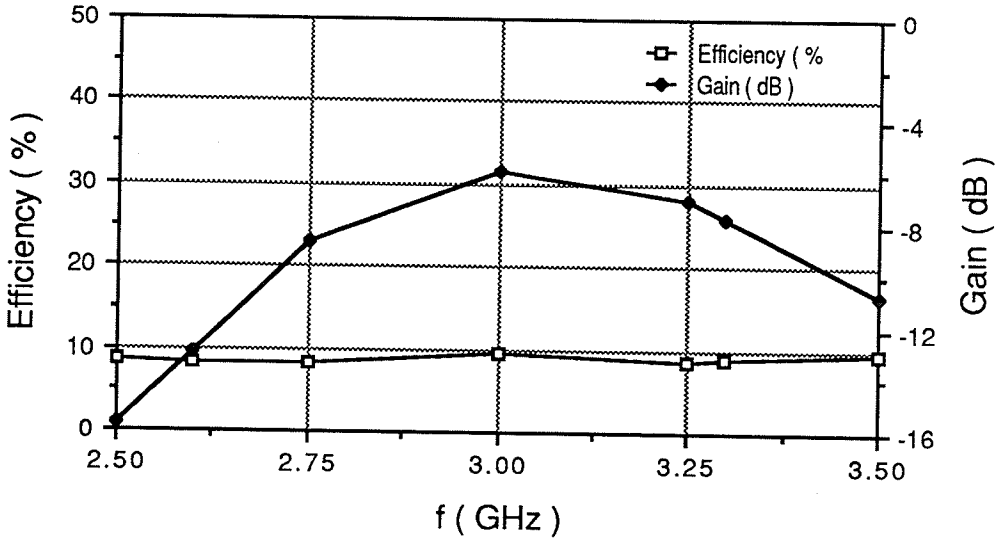

Fig. 4.16 b) : Radiation efficiency and gain of the 4-arm antenna

This antenna was further studied with the matched load removed. The end of the antenna was left open circuit and then shorted. Under both these terminating conditions, a standing wave current distribution was present. Figure 4.17 (a) shows this for the open circuit condition. In addition, the radiation pattern and axial ratio are shown for f = 3 GHz. These show a broadside pattern which is linearly polarized. Both field magnitudes are equal, but in-phase, thus the resultant linear vector is at 45^{o} as shown in 4.18 (a). The same characteristics were observed for the short circuit condition.

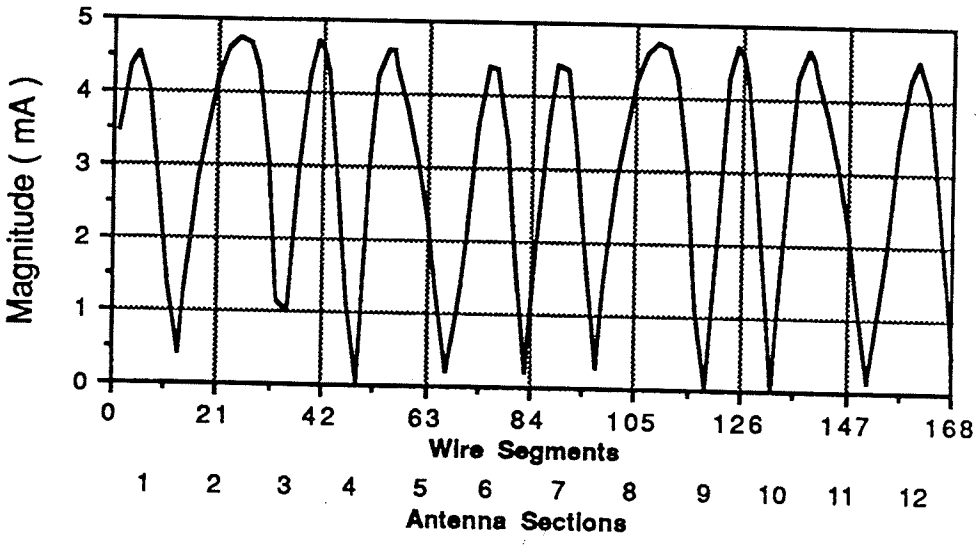

Fig. 4.17 a) : Current distribution of open circuit 4-arm antenna, $f_o = 3$ GHz

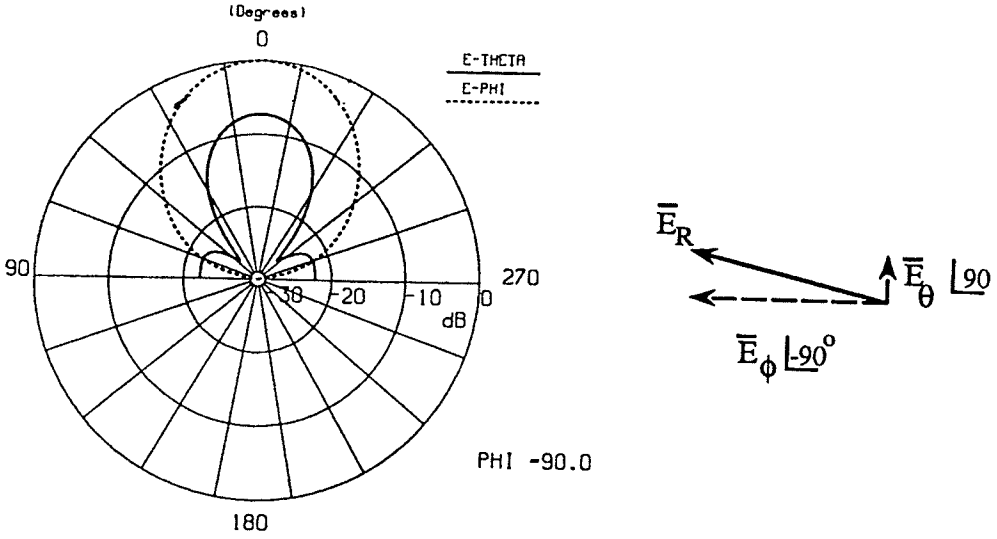

Fig. 4.17 b) : Radiation pattern and vector representation of open 4-arm antenna, $f_o = 3$ GHz

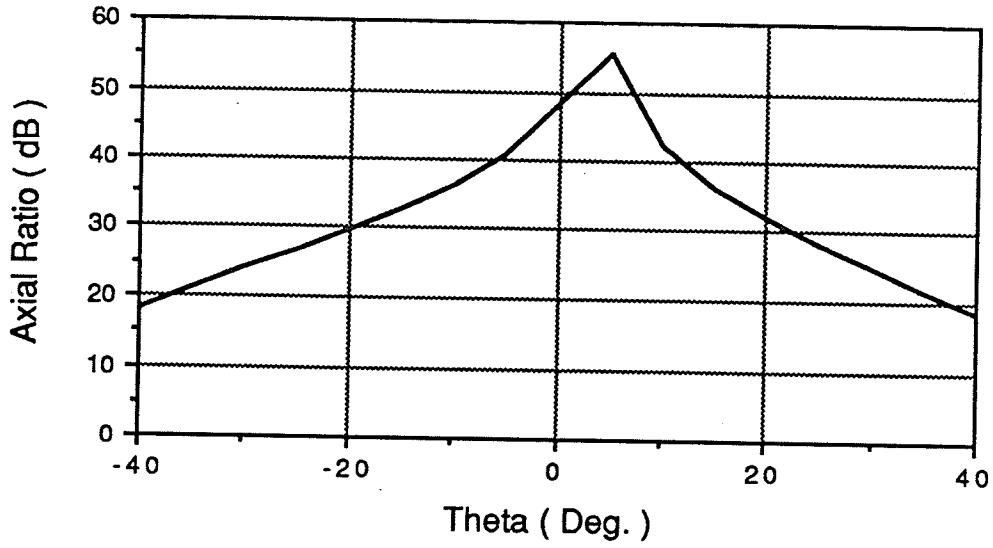

Fig. 4.17 c) : Axial ratio of open circuit 4-arm antenna

A frequency sweep from 2.75 GHz to 3.25 GHz was performed under both these conditions. The patterns for the open circuit condition are given in figure 4.18 and those for the short circuit condition are given in figure 4.19. Frequencies outside this range resulted in pattern degradation. Accompanying each polar plot is a vector representation of the direction of linear polarization.

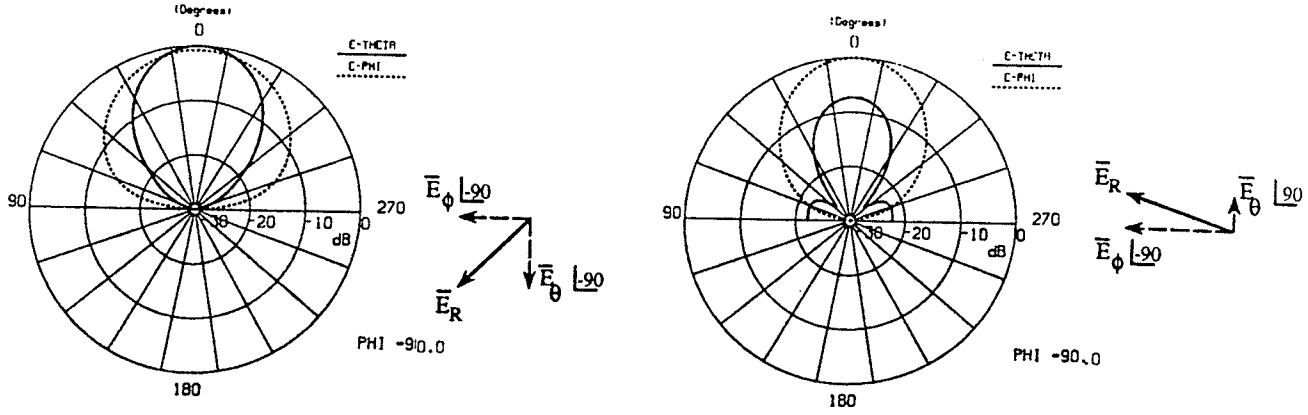

(a) f = 2.75 GHz

(b) f = 3.0 GHz

Fig. 4.18 : Frequency sweep of open circuit terminated antenna, E-plane

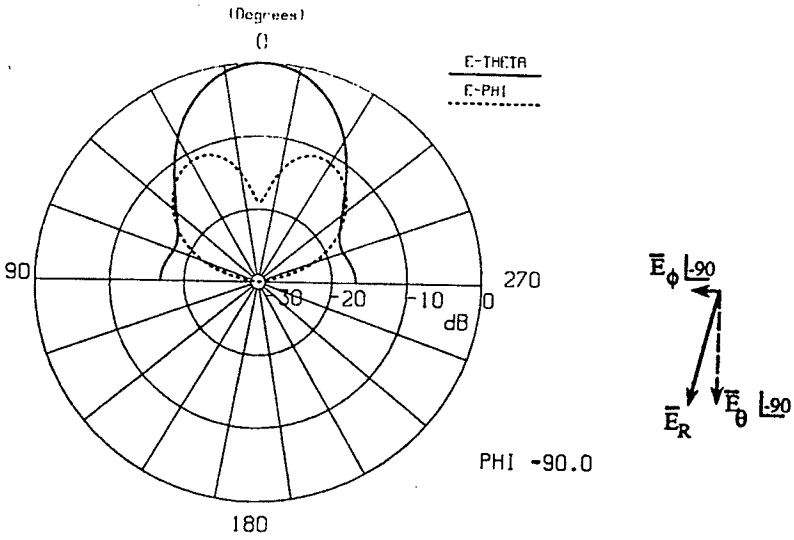

(c) f = 3.25 GHz

Fig. 4.18 (cont.)

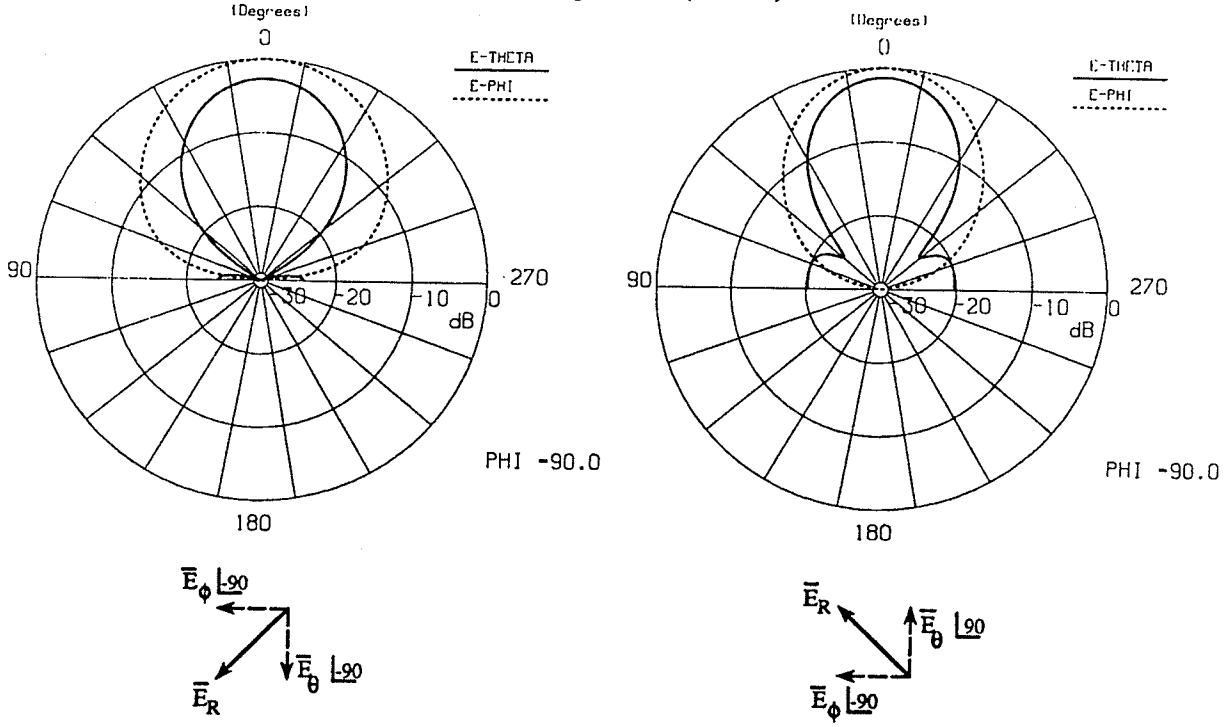

(a) f = 2.75 GHz

(b) f = 3.0 GHz

Figure 4.19 : Frequency sweep of short circuit terminated 4-arm antenna, E-plane

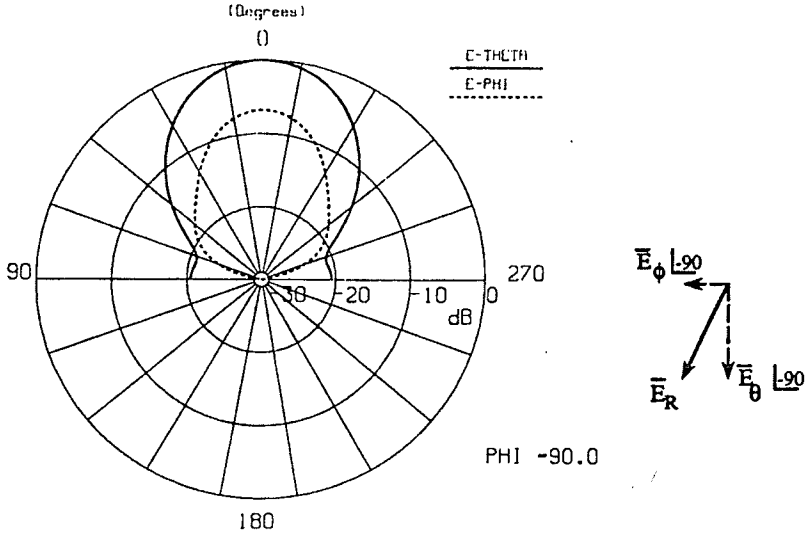

(c) f = 3.25 GHz

Fig. 4.19 (cont.)

A pattern bandwidth very narrow for applications which require vertical or horizontal linear polarization as the direction of polarization varies dramatically with frequency. The input impedance and gain were also plotted for this frequency range and are shown in figure 4.20. The bandwidth can be seen to be very small. This structure shows close to 100 % radiation efficiency due to the reflections at the line end. A substantial increase in gain can also be seen in figure 4.20 (c).

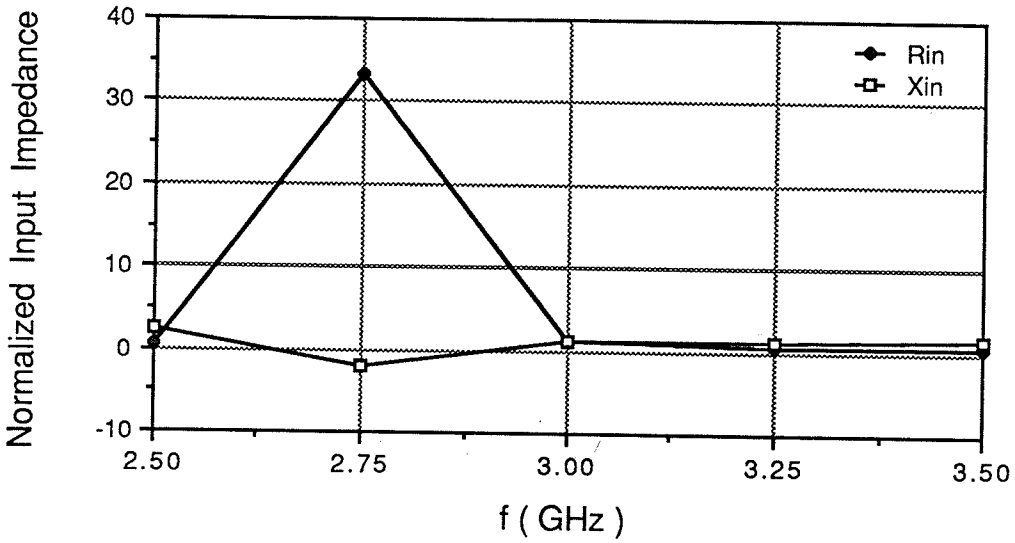

Fig. 4.20 a) : Input impedance of open circuit 4-arm antenna normalized to $Z_{in_{3\ GHz}} = 1.87\text{-}j308\ \Omega$

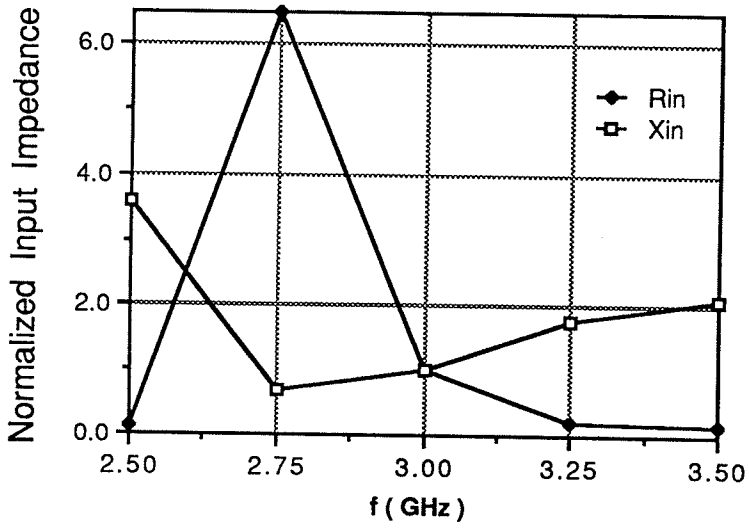

Fig. 4.20 b) : Input impedance of short circuit 4-arm antenna normalized to $Z_{in_{3\ GHz}} = 5.0\text{-}j180\ \Omega$

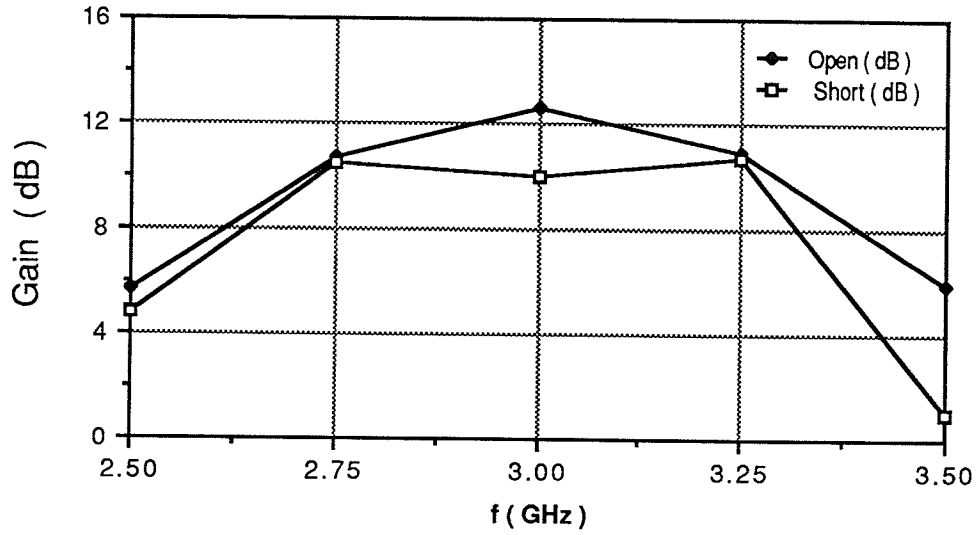

Fig. 4.20 c) : Gain of open and short circuit terminated 4-arm antenna, f_o = 3 GHz

It has been found that the four arm structure radiates a linearly polarized pattern when terminated with a short or open circuit. A matched load termination generates a circular polarized pattern with a large impedance and pattern bandwidth. However, the traveling wave structure has the problem of low radiation efficiency. Possible techniques to improve the efficiency are now investigated.

4.3.4 Efficiency Improvements of 4-arm antenna

In order to determine methods to improve efficiency, the cause of the low efficiency should be understood. This can be done by examining the current distribution along the structure and applying the concept of image theory. Equation (4.1b) defines a current of

$$\bar{I} = H_y \hat{x} \tag{4.11}$$

along a microstrip line. A ground plane below is equivalent to an image structure underneath with the tangential currents oppositely phased. This is illustrated in figure 4.21.

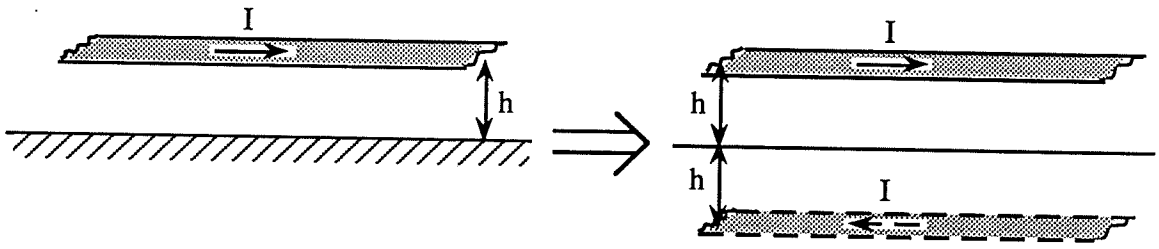

Fig. 4.21 : Currents of a microstrip line

At a small height above the ground plane the structure is very close to its image which has opposing currents. This results in most of the radiated field being cancelled by the image structure. Thus the first method to improve efficiency and to confirm this analogy would be to increase the height over the ground plane. This should improve the efficiency and become maximized at a height of $\lambda/4$ where the structure and image will be in phase and add constructively. The structure at various heights above the ground plane was analyzed using NEC and the results of efficiency and peak gain are given in figure 4.22.

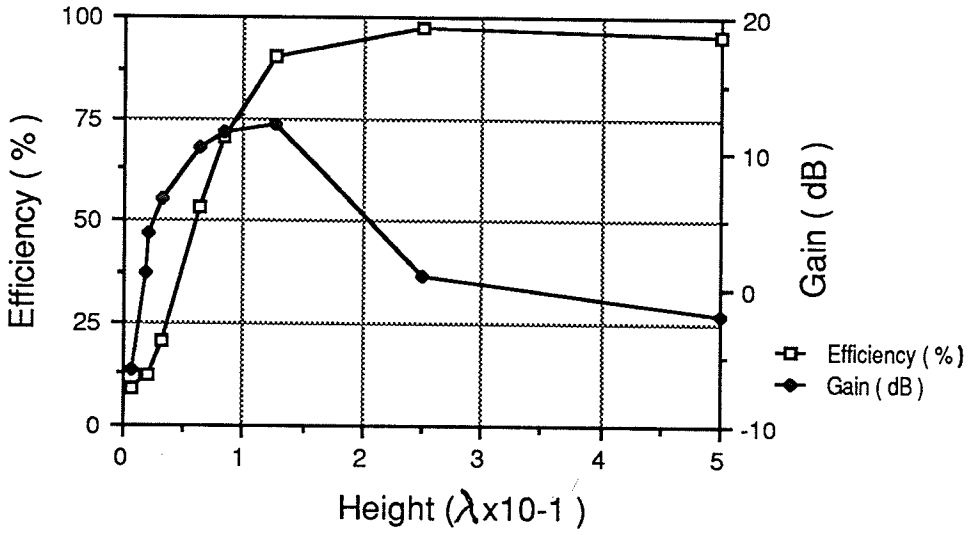

Fig. 4.22 : Effects of height on efficiency and gain of 4-arm antenna.

As the height above the ground plane increases, the efficiency and gain increase as expected. The gain decreases after h = λ/4 since the radiation pattern begins to degrade at this point. A height of λ/60 corresponds to a 25 mil thick alumina substrate. This height yields a slightly improved efficiency than a height of λ/156 above the ground plane and will be used in the experimental verification. At this height and other heights close to the ground plane, the antenna structures were observed to behave with similar characteristics as previously noted. Thus it has been shown that the efficiency can be improved by increasing the height. However, this is not a practical solution since the substrates used are 10 to 25 mils in thickness. An alternate approach already observed with the 8-arm antenna is to increase the number of discontinuities in the structure.

One method is to increase the discontinuities at the outer radiating segments. Two concepts studied are illustrated in figure 4.23.

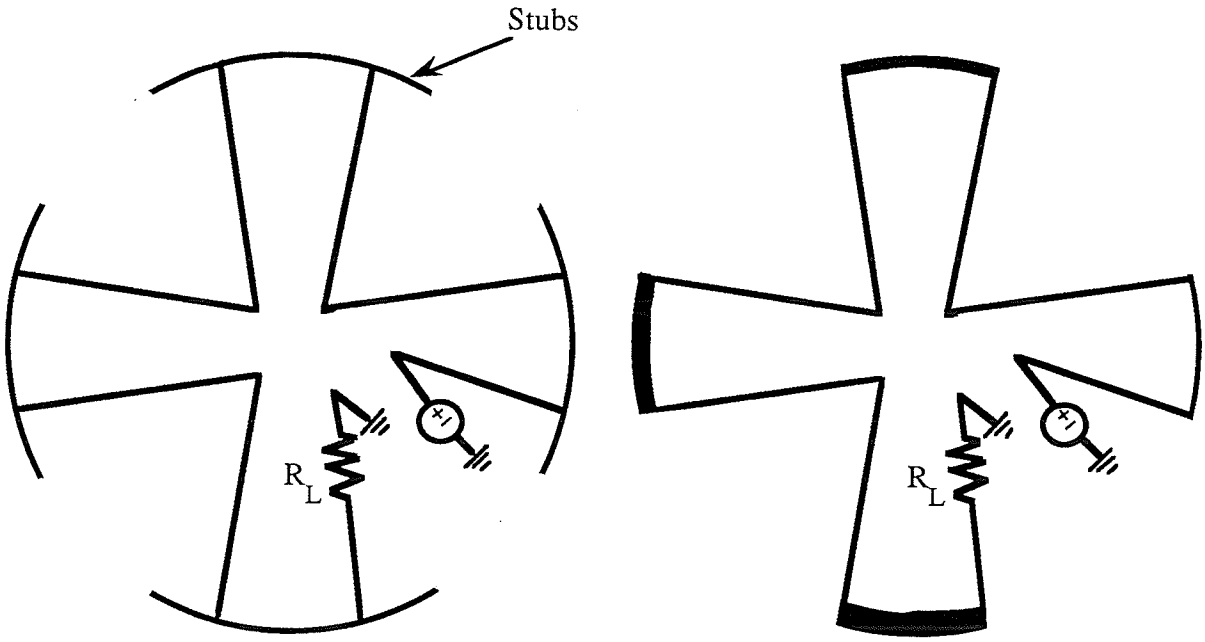

(a) Stubs (b) Tapered patches

Figure 4.23 : Geometries with increased discontinuities.

Figure 4.23 (a) has open circuit stubs attached to the corners of each arm with the antenna being match terminated. NEC indicated a standing wave current distribution and hence a linearly polarized pattern resulted with these additions. An interesting result is that the direction of the linear polarization can be controlled by the stub lengths. A vectorial representation of the fields accompanies the radiation patterns given in figure 4.24. This shows that the direction of polarization changes from vertical to horizontal as the stub length is increased.

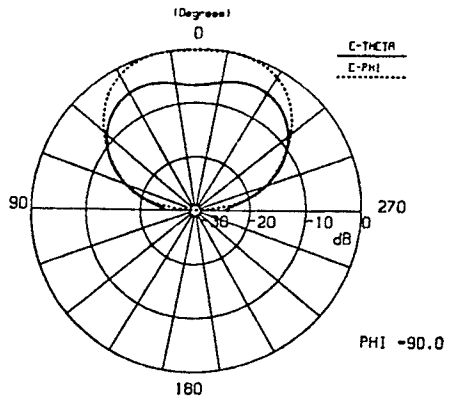

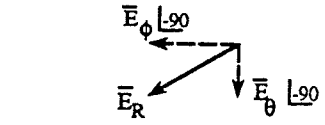

(a) λ/16 stubs

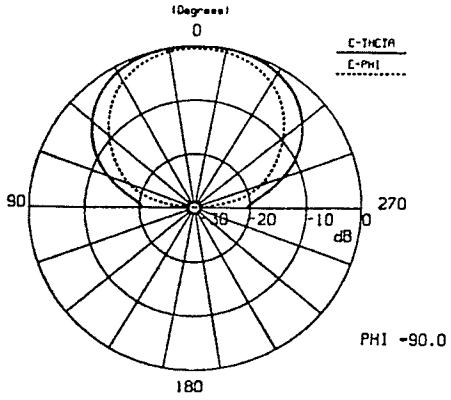

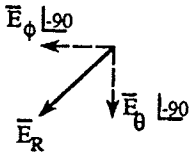

(b) λ/32 stubs

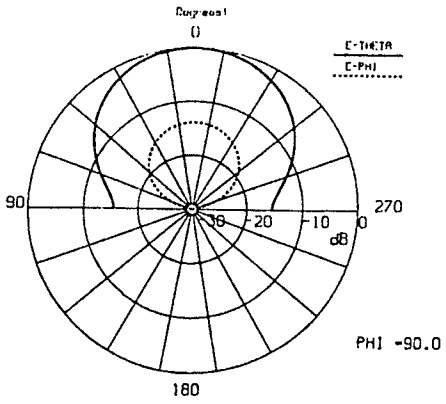

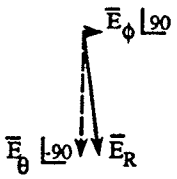

(c) λ/64 stubs

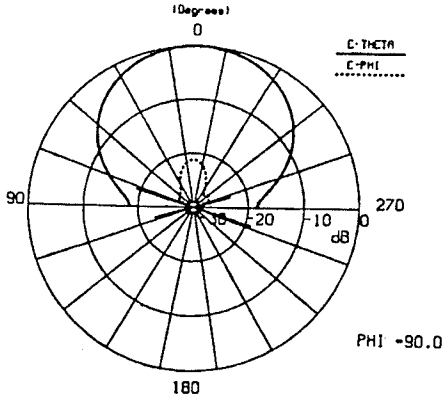

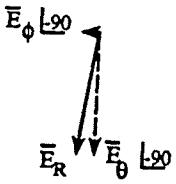

(d) λ/128 stubs

Fig. 4.24 : 4-arm antenna with various stub lengths, E-plane

The stub lengths of λ/128 were selected to be studied over a frequency range since this produces a pattern which is very nearly vertically polarized. Figure 4.25 shows the patterns generated from 2.75 GHz to 4 GHz and the input impedance is given in figure 4.26.

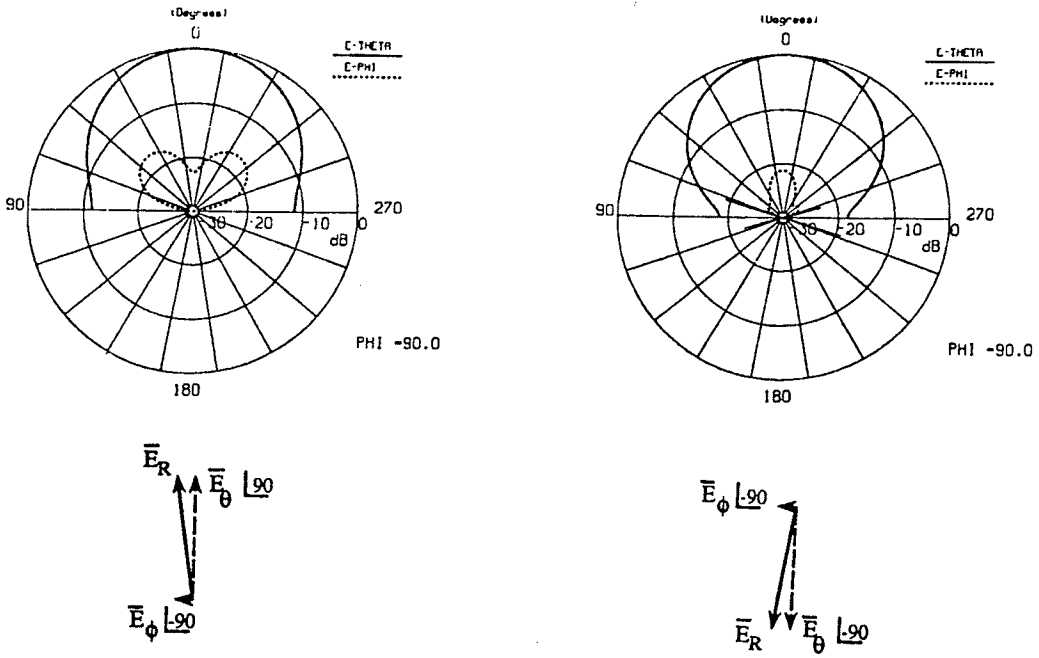

(a) f = 2.75 GHz = f_L

(b) f = 3.0 GHz = f_o

Fig. 4.25 : Frequency sweep of 4-arm antenna with λ/128 stubs, E-plane

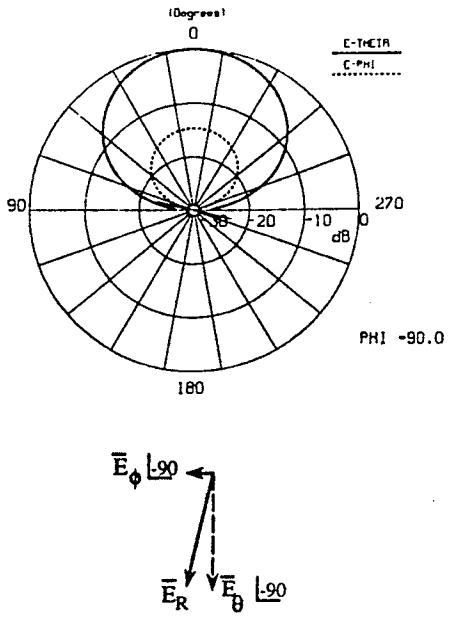

(c) f = 3.25 GHz

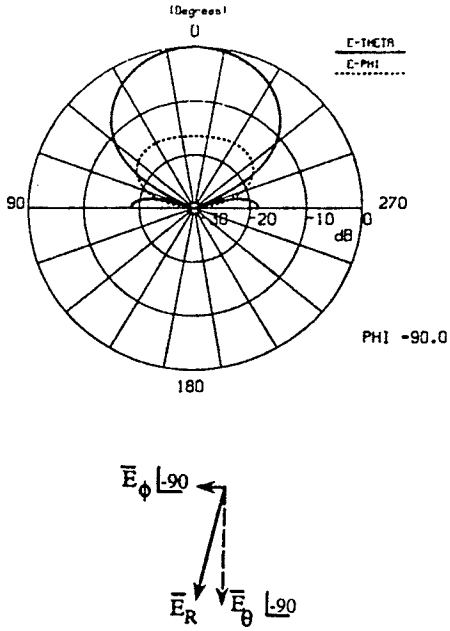

(d) f = 3.5 GHz = f_U

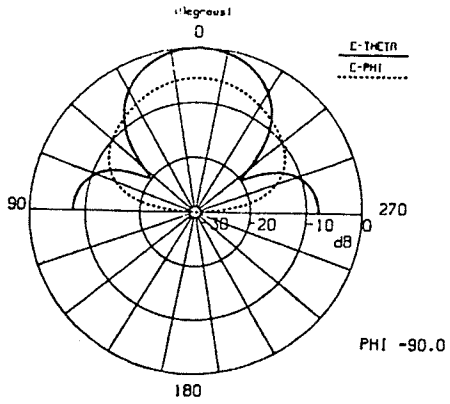

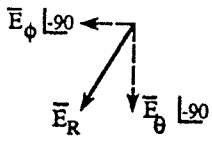

(e) f = 4 GHz

Fig. 4.25 (cont.)

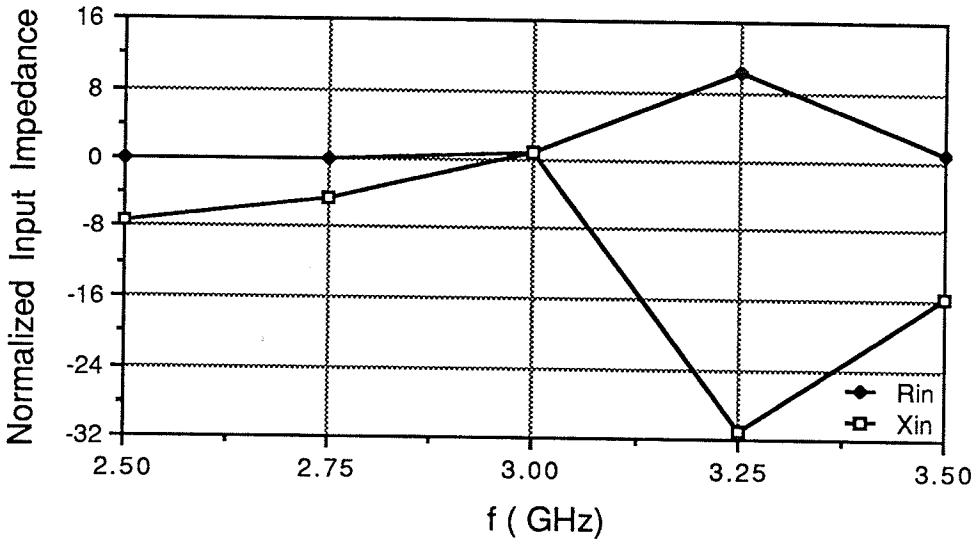

Fig. 4.26 : Input impedance of 4-arm antenna with λ/128 stubs normalized to $Z_{in_{3\ GHz}} = 1.75+j54\ \Omega$

These figures show that this structure with λ/128 stubs has a relatively large pattern bandwidth, but a very narrow impedance bandwidth. An important observation is that the direction of polarization remained fairly constant over the frequency range within the pattern bandwidth, while the polarization of the open 4-arm antenna with no stubs varied immensely, thus generating a small pattern bandwidth. Similar characteristics were observed for the structure with λ/64 stubs. The efficiency of all structures with stubs was in the order of 98 %. This high efficiency is due to a standing wave current distribution which is created by the open end stubs. This structure yields a peak gain of 8.6 dB. The stubs were placed in various geometries as shown in figure 4.27. However, these configurations did not have improved characteristics over the one shown in figure 4.23 (a). Most characteristics were equivalent except the gain which can be seen in figure 4.27. The stubs oriented in these configurations generate fields which add in a destructive manner, thus the gain is quite low for some.

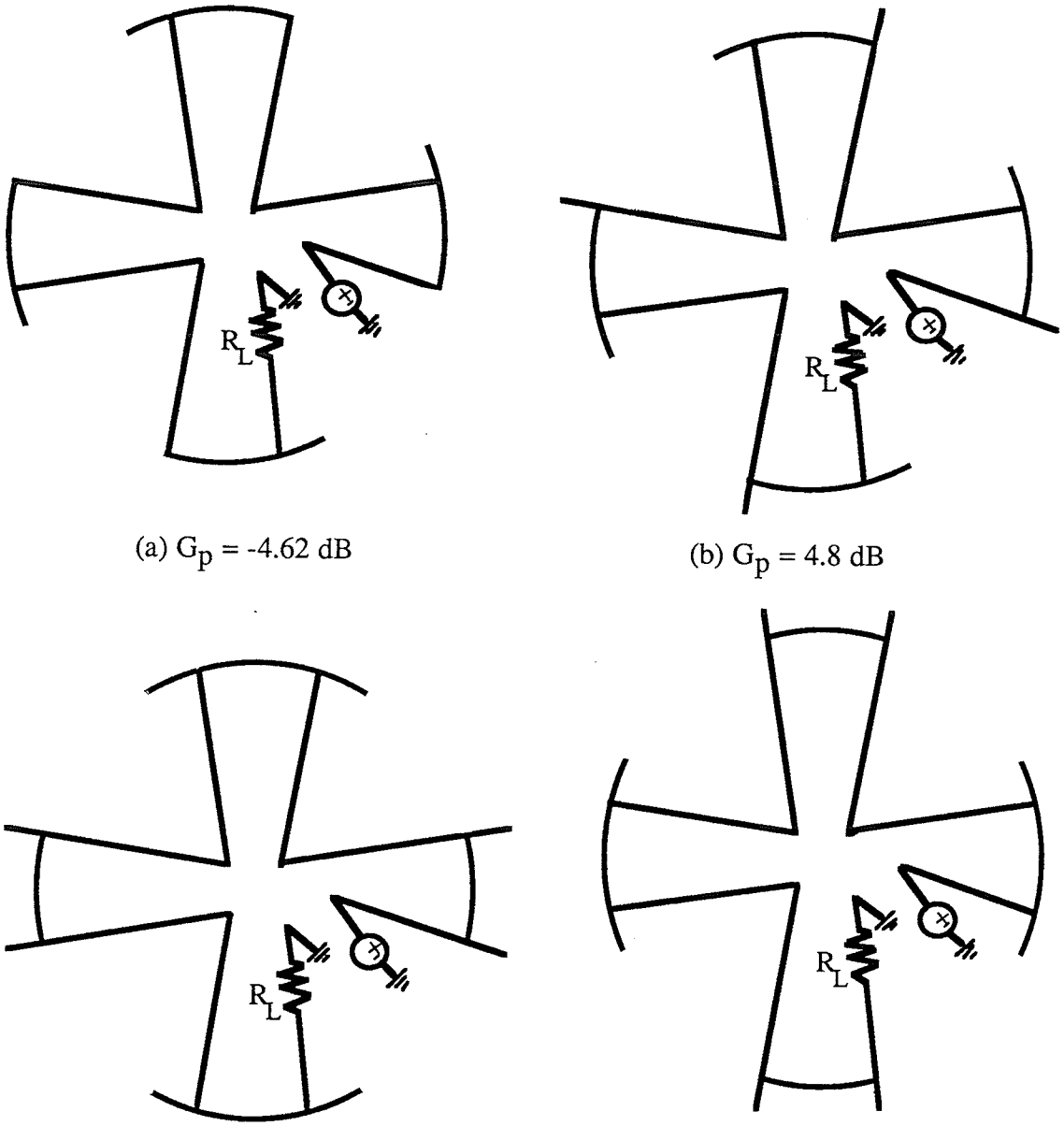

(a) G_p = -4.62 dB

(b) G_p = 4.8 dB

(c) G_p = 7.63 dB

(d) G_p = 0.42 dB

Fig. 4.27 : Various stub orientations on 4-arm antenna

The structure in figure 4.23 (b) contains patches at the end of each arm. These patches increase progressively in width along each arm of the antenna. Several cases were modelled using NEC and all cases indicated an efficiency of approximately 30 %. The pattern bandwidth was very narrow, in the order of a few percent, as the pattern remained constant only around the operating frequency. Thus this structure was considered unsuitable but was studied to determine its effects on the radiation efficiency.

Another alternate method of increasing the discontinuities is to increase the number of windings for the structure as shown in figure 4.28.

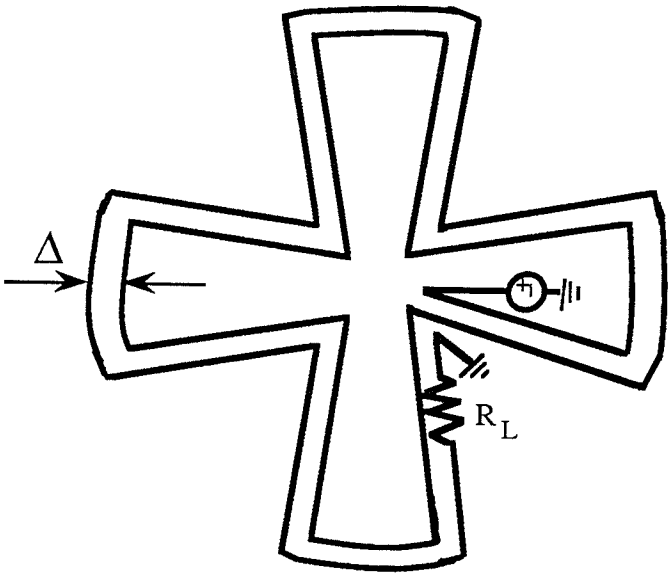

Fig. 4.28 : 4-arm antenna with two windings.

This structure was constructed such that the of the average inner and outer segments would be $\lambda/4$. The efficiency was first studied as a function of the distance, Δ, between the two windings. The results of this are given in figure 4.29 from this, it was determined that the

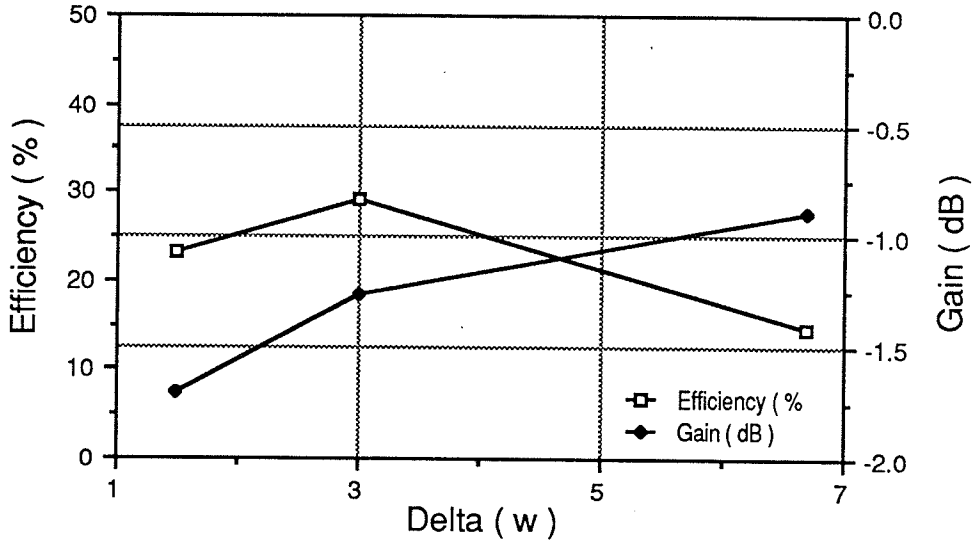

Fig. 4.29 : Effects of winding gap on 4-arm antenna with two windings.

ideal separation distance is 3 line widths yielding an efficiency of 29.2 %. A frequency sweep from 2.75 GHz to 3.5 GHz was performed to determine the pattern bandwidth. Figure 4.30 shows the pattern bandwidth to be $BW_{pat} = 15\%$. The input impedance over this frequency range is shown in figure 4.31, from which the bandwidth is determined to be $BW_{Zin} \cong 13$ %.

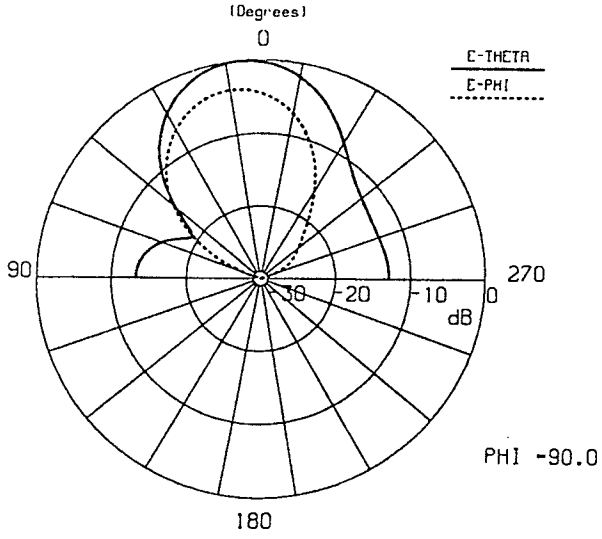

(a) f = 2.75 GHz

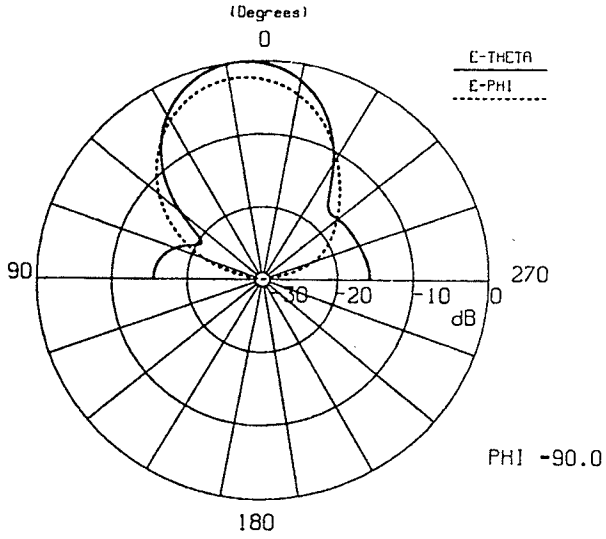

(b) f = 2.775 GHz = f_L

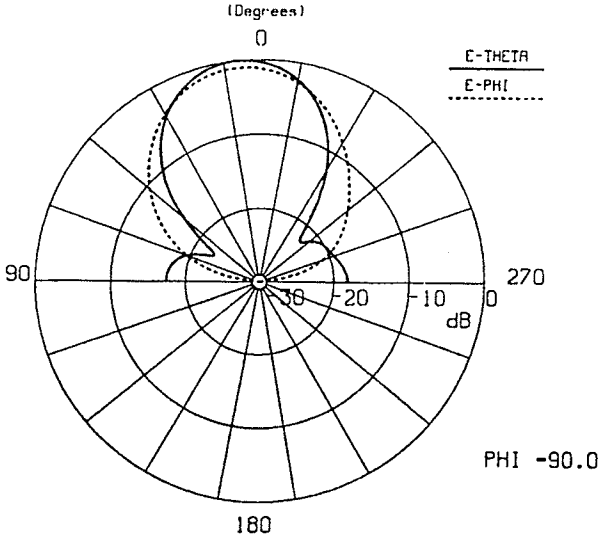

(c) f = 2.8 GHz

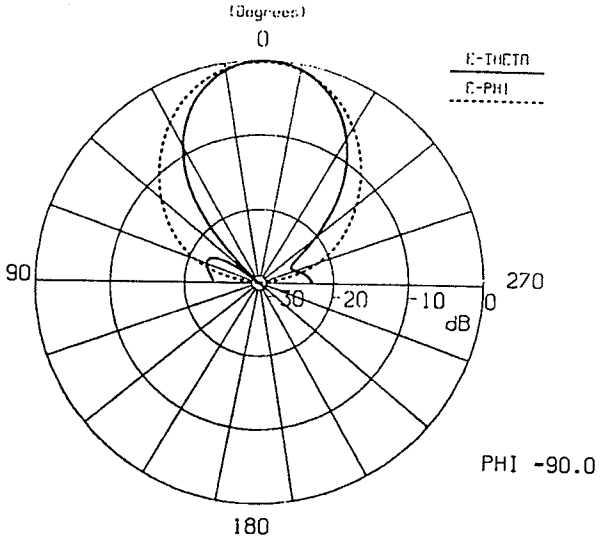

(d) f = 3.0 GHz = f_o

Fig. 4.30 : Frequency sweep of 4-arm antenna with two windings, E-plane

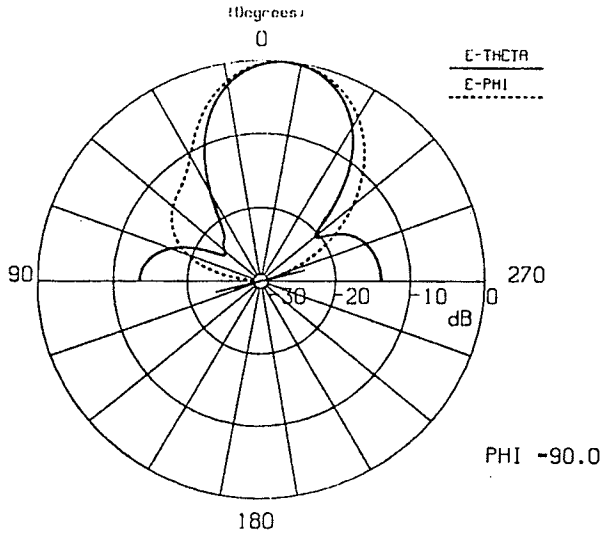

(e) f = 3.2 GHz

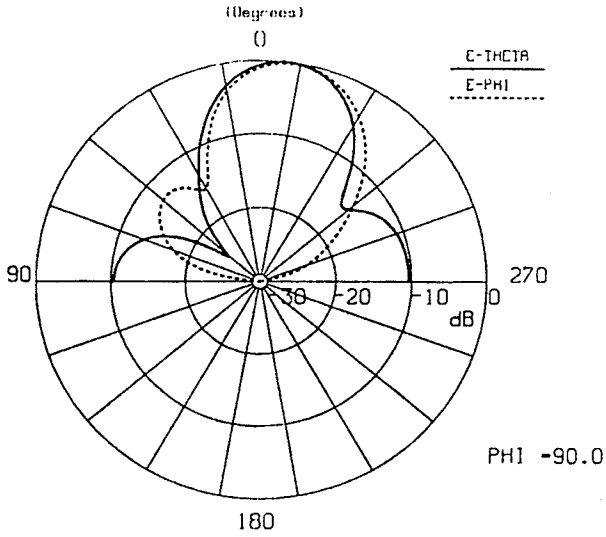

(f) f = 3.225 GHz = f_U

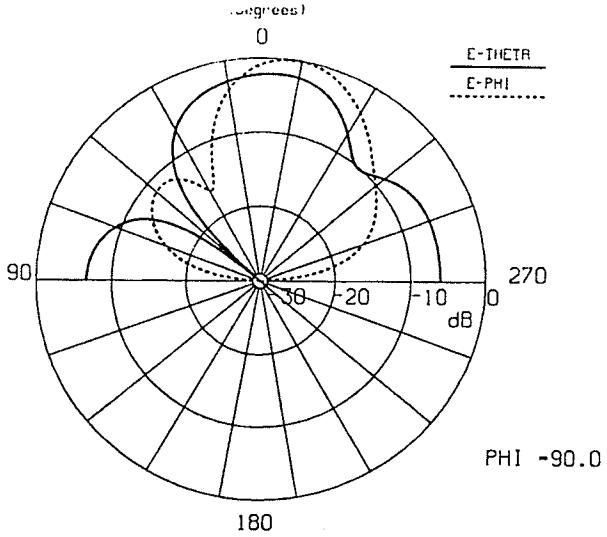

(g) f = 3.25 GHz

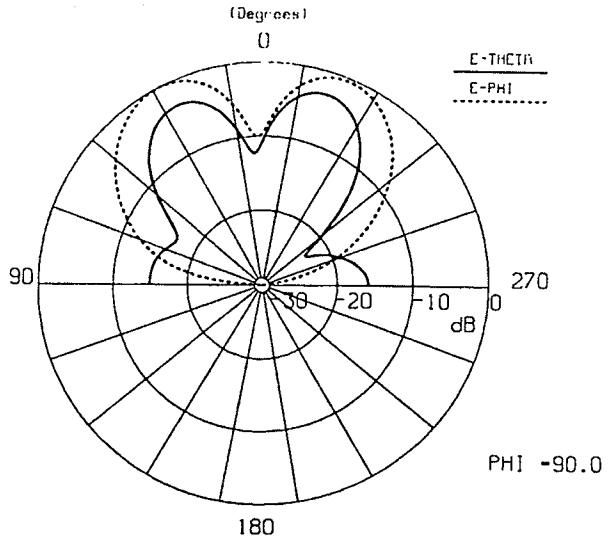

(h) f = 3.5 GHz

Fig. 4.30 (cont.)

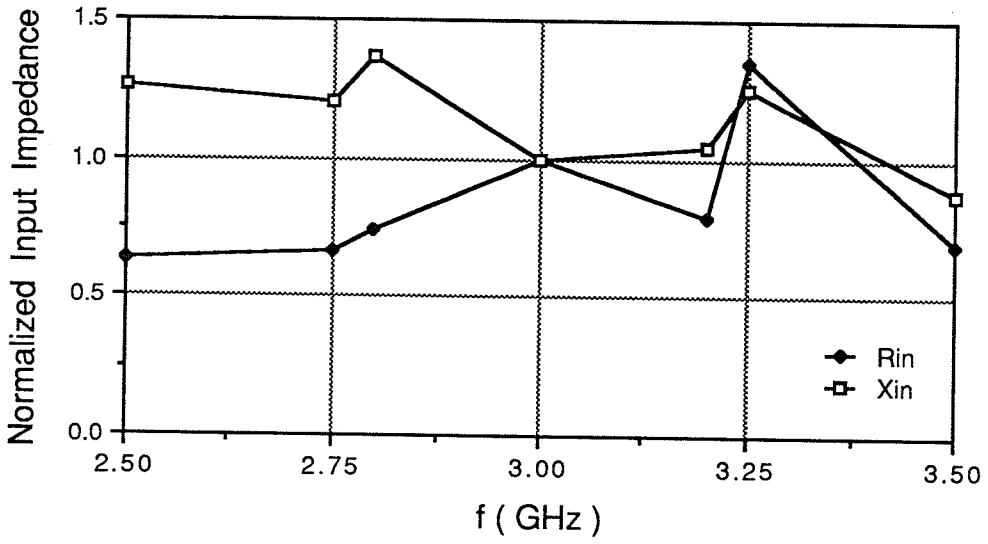

Fig. 4.31 : Input impedance of 4-arm antenna with two windings normalized to $Z_{in_{3\ GHz}} = 128\text{-}j410\ \Omega$

Some of the studied structures were fabricated and tested to confirm both the theoretical and numerical results.

4.4 Experimental Data for the Traveling Wave Antenna

The antenna structures for testing were fabricated by the Department of Components and Subsystems at the Communications Research Center. The first stage of this process involved designing a mask of the microstrip antenna. With the mask completed, the antenna design was etched onto a grounded alumina ($\varepsilon_r = 9.8$) substrate 2" x 2" x .025" using the lift-off technique. The width of the microstrip line was chosen such that the characteristic impedance of the line, would be 50Ω. This was calculated as follows [42] :

$$\frac{w}{h} = \left[\frac{e^{H'}}{8} - \frac{1}{4\,e^{H'}}\right] \qquad \text{,for } Z_o > (44\text{-}2\varepsilon_r)\ \Omega \qquad (4.11\ a)$$

where

$$H' = \frac{Z_o \sqrt{2(\varepsilon_r + 1)}}{120} + \frac{1}{2}\left(\frac{\varepsilon_r - 1}{\varepsilon_r + 1}\right)\left(\ln\frac{\pi}{2} + \frac{1}{\varepsilon_r}\ln\frac{4}{\pi}\right)$$

and

$$\frac{w}{h} = \frac{2}{\pi}\left[\left(d_\varepsilon - 1\right) - \ln\left(2\,d_\varepsilon - 1\right)\right] + \frac{\varepsilon_r - 1}{\pi\,\varepsilon_r}\left[\ln\left(d_\varepsilon - 1\right) + 0.293 - \frac{0.517}{\varepsilon_r}\right],$$

$$\text{for } Z_o < \left(44 - 2\varepsilon_r\right)\Omega \qquad (4.11\text{ b})$$

with

$$d_\varepsilon = \frac{60\,\pi^2}{Z_o\sqrt{\varepsilon_r}}$$

For $\varepsilon_r = 9.8$ and $Z_o = 50\Omega$, equation (4.11 a) is used. Substituting these values and a height of .025" = .635 mm yields a width of w = .62 mm. The lengths of the lines were defined by the effective wavelength, at 3 GHz. This may be shown as

$$\lambda_{eff} = \frac{\lambda_o}{\sqrt{\varepsilon_{eff}}} \qquad (4.12)$$

where

$$\lambda_o = \frac{c}{f_o}$$

$$\varepsilon_{eff} = \frac{\varepsilon_r + 1}{2} + \frac{\varepsilon_r - 1}{2}\left(1 + 10\,\frac{h}{w}\right)^{-0.5}$$

Equation (4.12) gives an effective wavelength of $\lambda_{eff} = 3.86$ cm at a frequency of 3 GHz. This information was used to design a four arm antenna.

A four arm microstrip antenna was etched on a grounded alumina substrate having the dimensions shown in figure 4.32. Feeding and terminating the antenna was accomplished by vertical launchers at the beginning and end of the structure. The launchers were fastened to a ground plane jig which supported the substrate chip. The vertical launchers were connected to the microstrip line by tabs soldered to the pin on one end and to the microstrip line on the other. An illustration of the complete set-up is given in

figure 4.32. As can be seen, this arrangement is convenient for altering the loading conditions at the termination point.

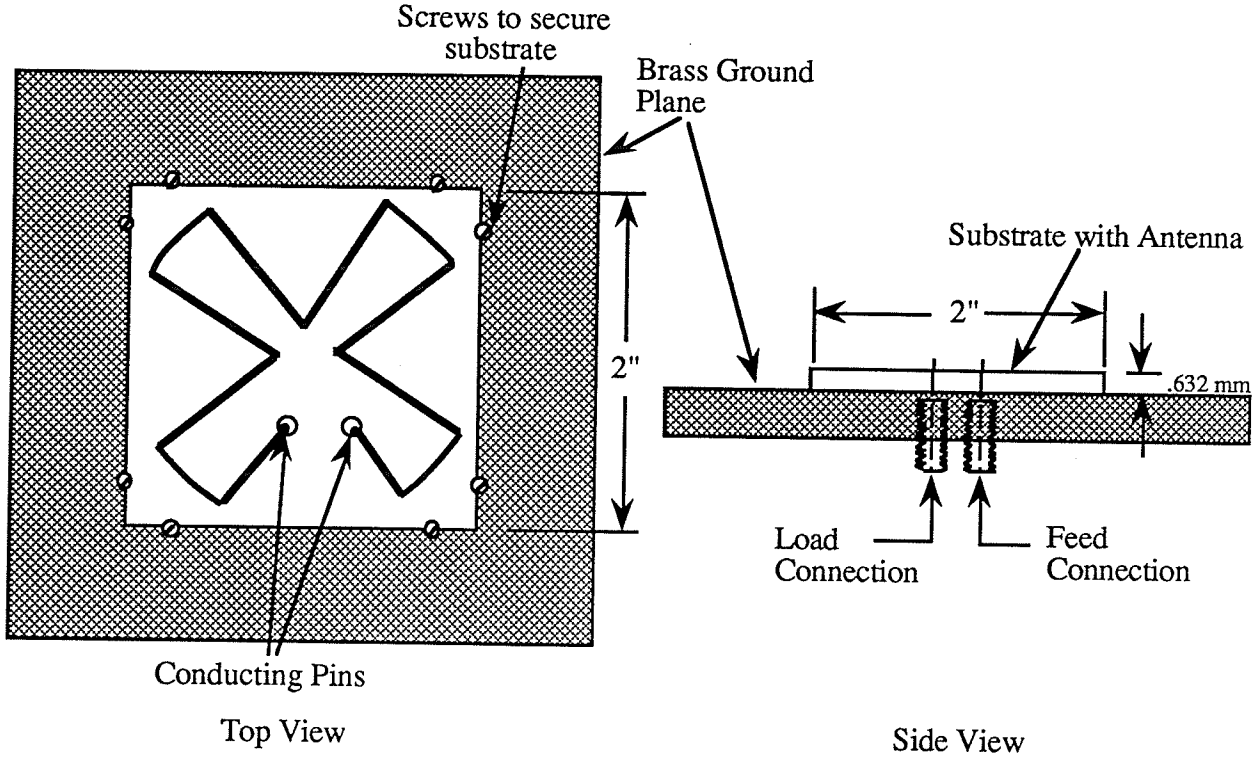

Fig. 4.32 : Fabricated 4-arm microstrip antenna

The testing procedure involved measuring the antenna scattering parameters and then the radiation pattern.

This antenna was then connected to an HP8510 Network Analyzer in order to determine the scattering parameters. The S_{11} and S_{21} parameters are of interest in order to determine the return loss and insertion loss of the antenna. An ideal antenna would have a low return loss value, indicating a good match, and a low insertion loss value. A low insertion loss value indicates that the majority of the energy does not reach the end of the antenna. It is desirable to have this energy dissipated in terms of radiation.

4.4.1 4-Arm Antenna : Matched Termination

The four arm antenna was terminated with the characteristic impedance of the line. The measured return loss and insertion loss are shown in figures 4.33 and 4.34 respectively. The frequency range observed was between 2 and 4 GHz. Over this range, the return loss was less than -10 dB, the specified cutoff point for the impedance bandwidth at VSWR = 2. Thus the input impedance bandwidth over this range is BW_{Zin} = 66.7 %. Unfortunately, figure 4.34 shows an insertion loss of only -0.75 dB. This indicates that the majority of the power is absorbed by the load, thus a very low radiation efficiency is present. This result is not surprising as this was predicted from the computer modelling.

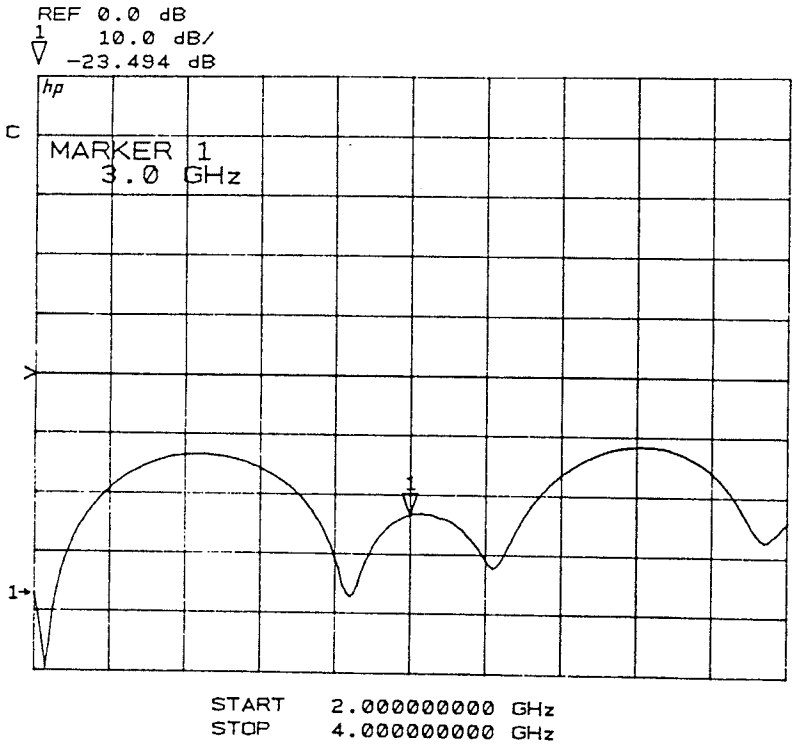

Fig. 4.33 : Return loss of match terminated 4-arm antenna

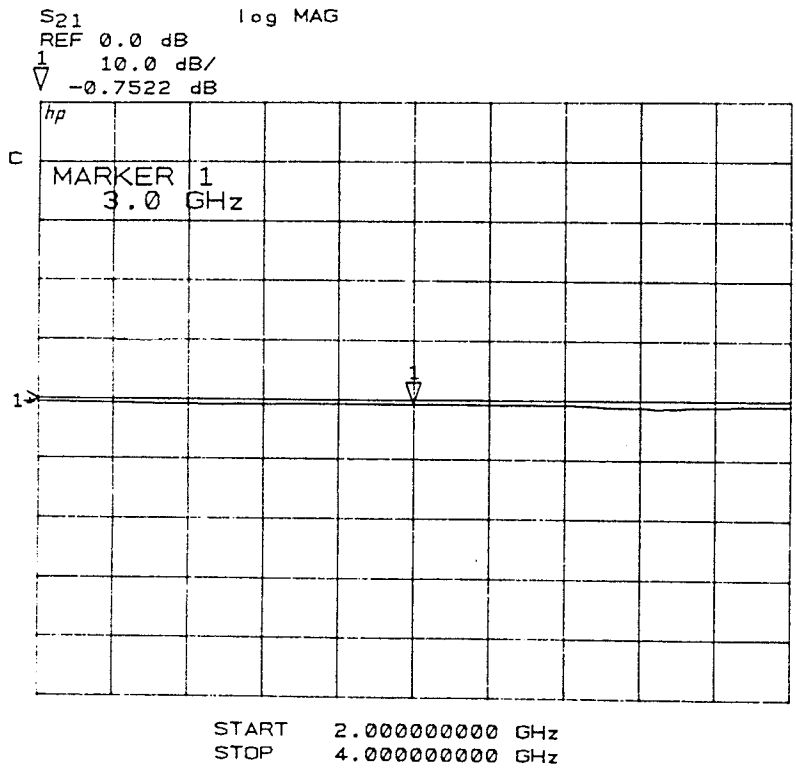

Fig. 4.34 : Insertion loss of match terminated 4-arm antenna

The radiation pattern of this structure was measured in the anechoic chamber at the University of Manitoba. Initially, a linear source was used to measure the field components of an elevation cut at $\phi = 0^{o}$, 45^{o}, and 90^{o}. These components were shown to be approximately equal, thus a good indication that circular polarization was present. A rotating linear source was next used to measure the pattern of the antenna as the angle of elevation varied from - 120 to +120 . Figure 4.35 shows these patterns over a frequency range of 2.55 GHz to 3.5 GHz. Patterns with acceptable characteristics can be found between 2.9 GHz and 3.5 GHz. This yields a bandwidth of $BW_{pat} = 15\%$ which is the predicted bandwidth. Within this bandwidth, the axial ratio is less than 3 dB and maintains a broadside pattern. Note also that for frequencies less than f_0, the beam squints towards $\theta > 0^{o}$ and tracks towards $\theta < 0^{o}$ for higher frequencies. The beam squint within BW_{pat} varies between $\pm 30^{o}$. It can also be determined that the 3 dB beamwidth is 40^{o}. To ascertain that acceptable circular polarization is present a measurement was taken with the

antenna at $\phi = 45^{o}$. The patterns measured within the above bandwidth are given in figure 4.36. These patterns have a slightly larger axial ratio, but may still be considered to be circular polarized. Thus this structure has many favorable characteristics except for the low efficiency previously noted. This is evident in the pattern measurements as the peak gain is -11 dB.

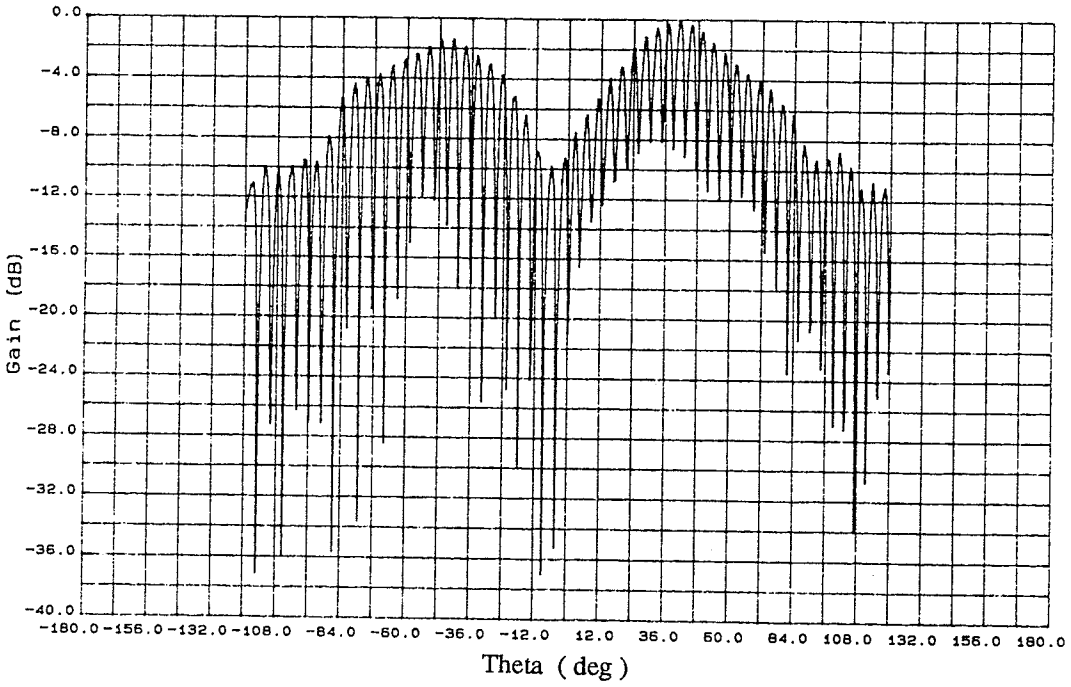

(a) f = 2.5 GHz, Gp = -20.17 dB

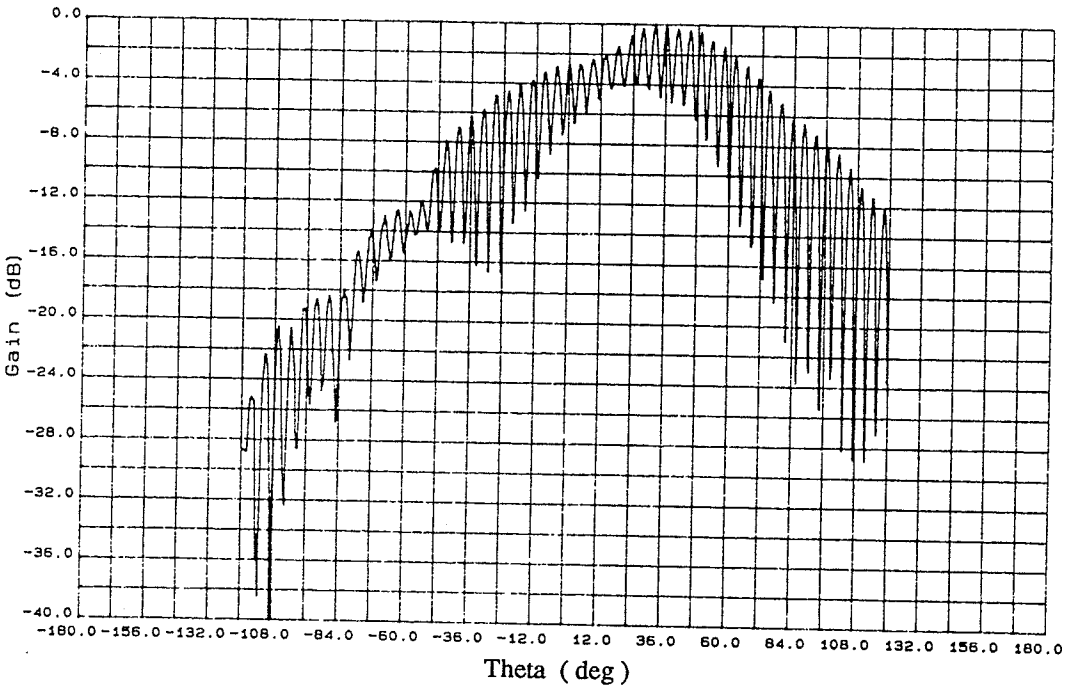

(b) f = 2.7 GHz, Gp = -15.4 dB

Fig. 4.35 : Measured patterns of matched, 4-arm antenna, $\phi = 0^{o}$, E-plane

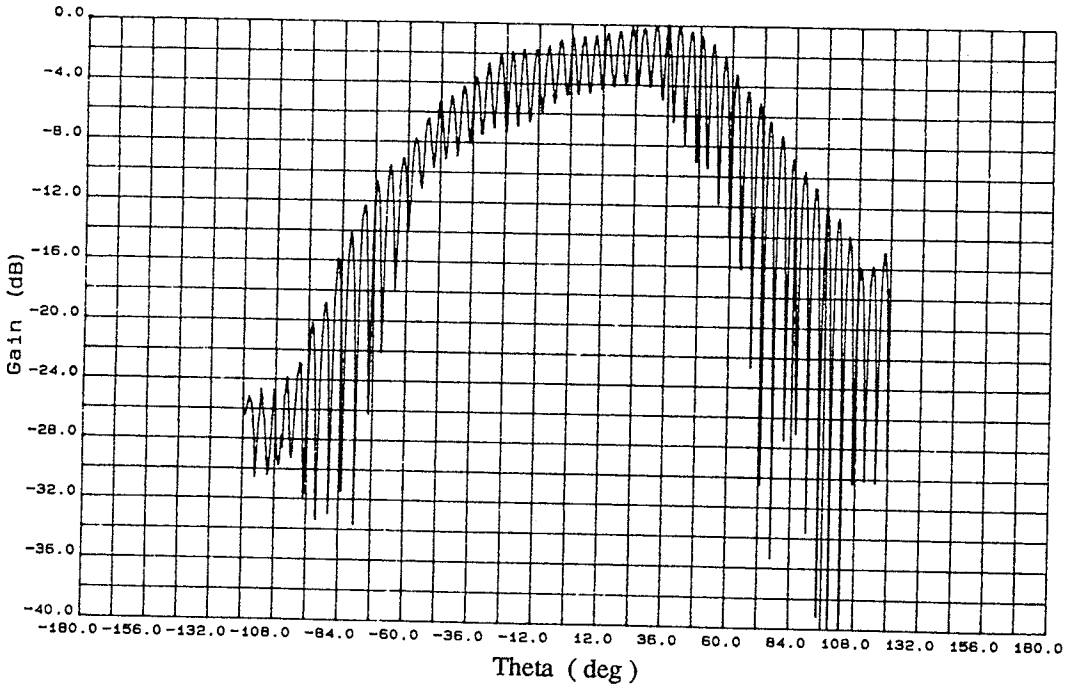

(c) f = 2.8 GHz, Gp = -13.53 dB

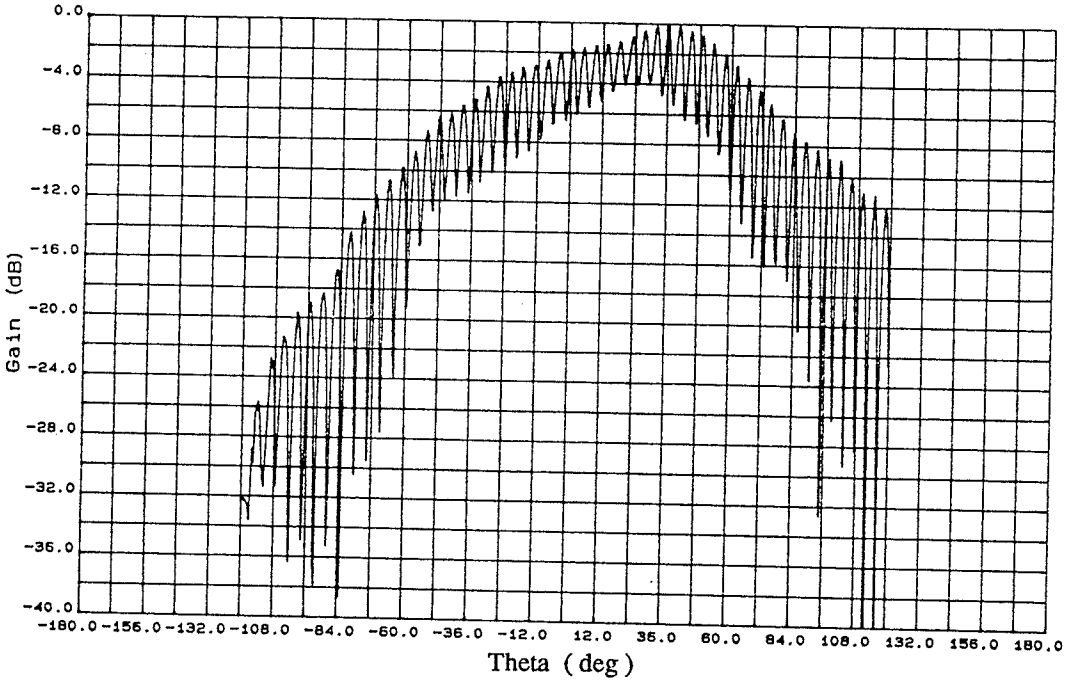

(d) f = 2.85 GHz, Gp = -13.38 dB

Fig. 4.35 (cont.)

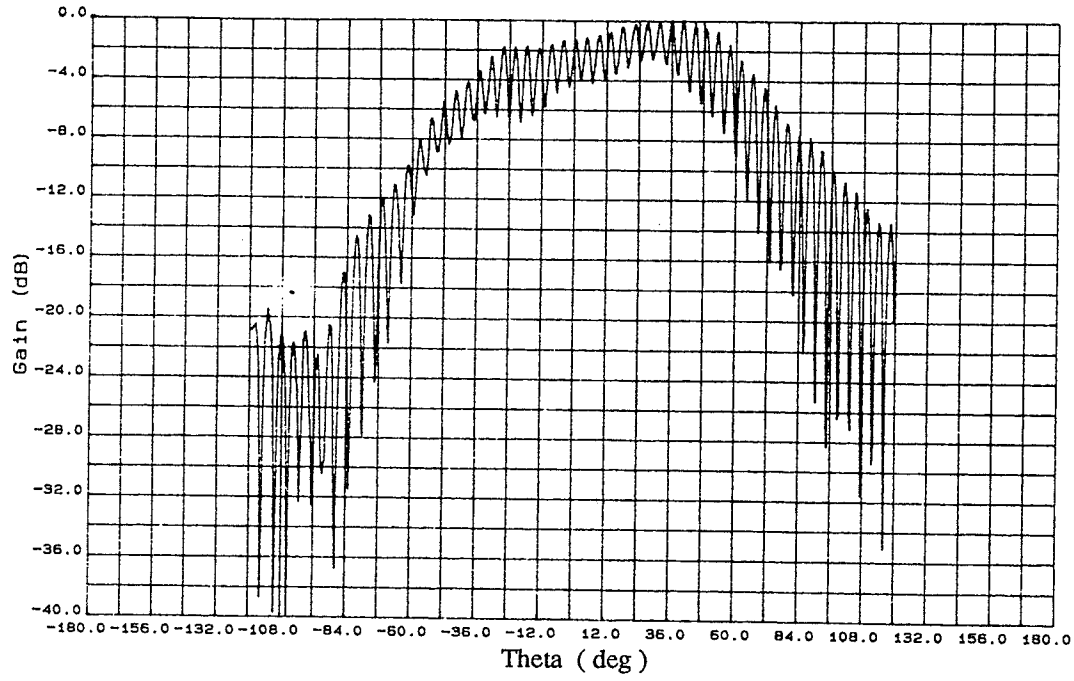

(e) f = 2.9 GHz = f_L, Gp = -13.37 dB

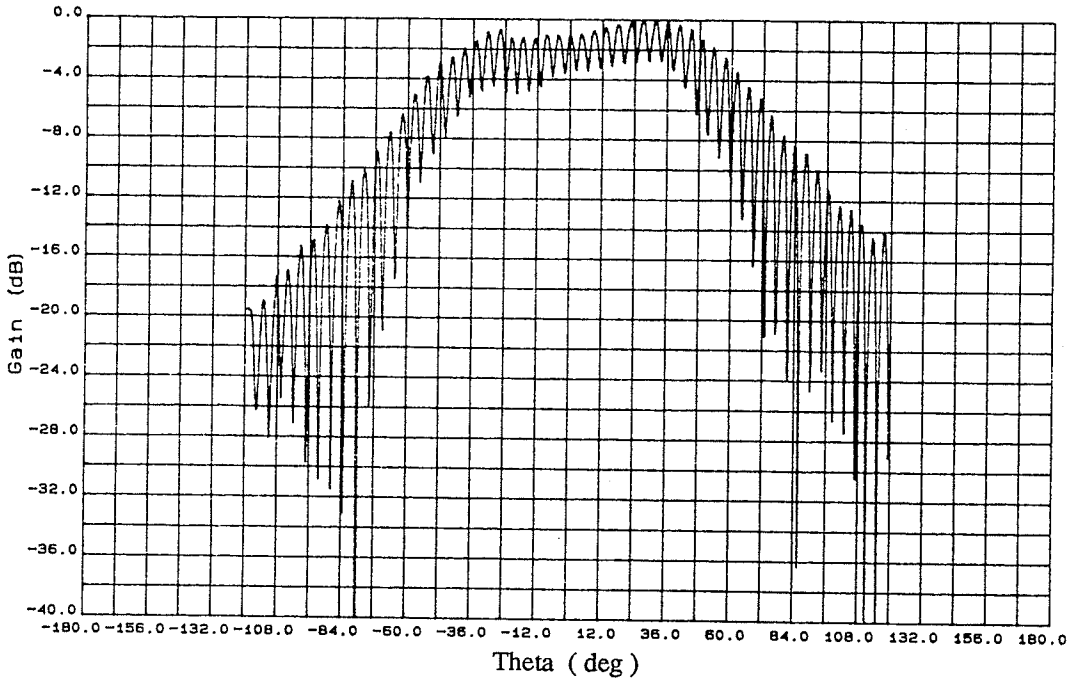

(f) f = 3.0 GHz = f_o, Gp = -12.96 dB

Fig. 4.35 (cont.)

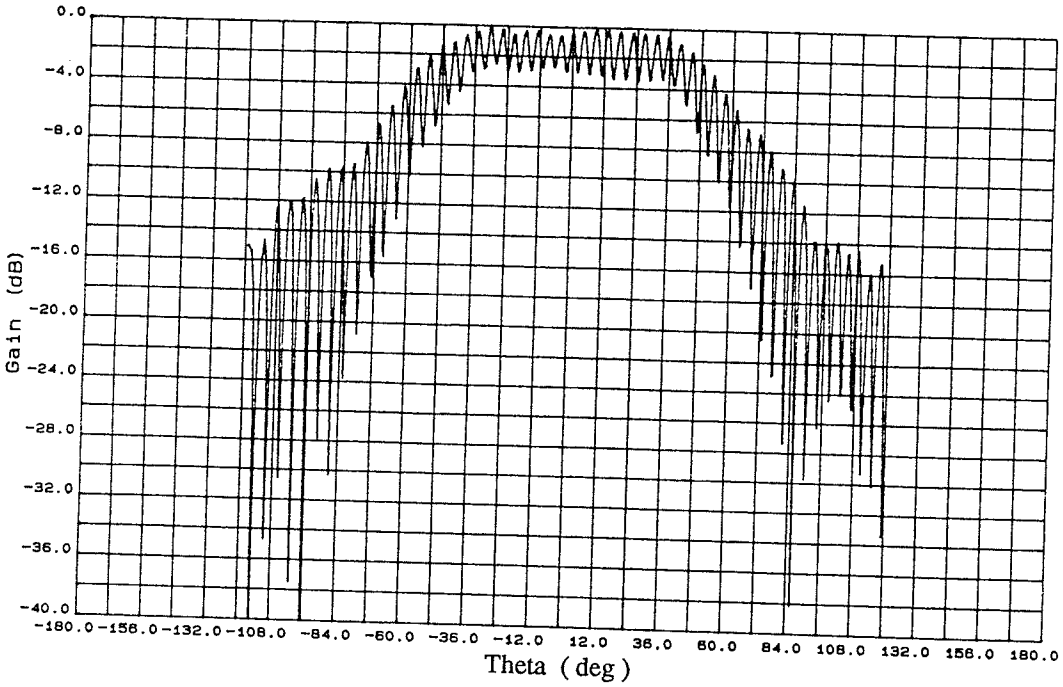

(g) f = 3.1 GHz, Gp = -12.58 dB

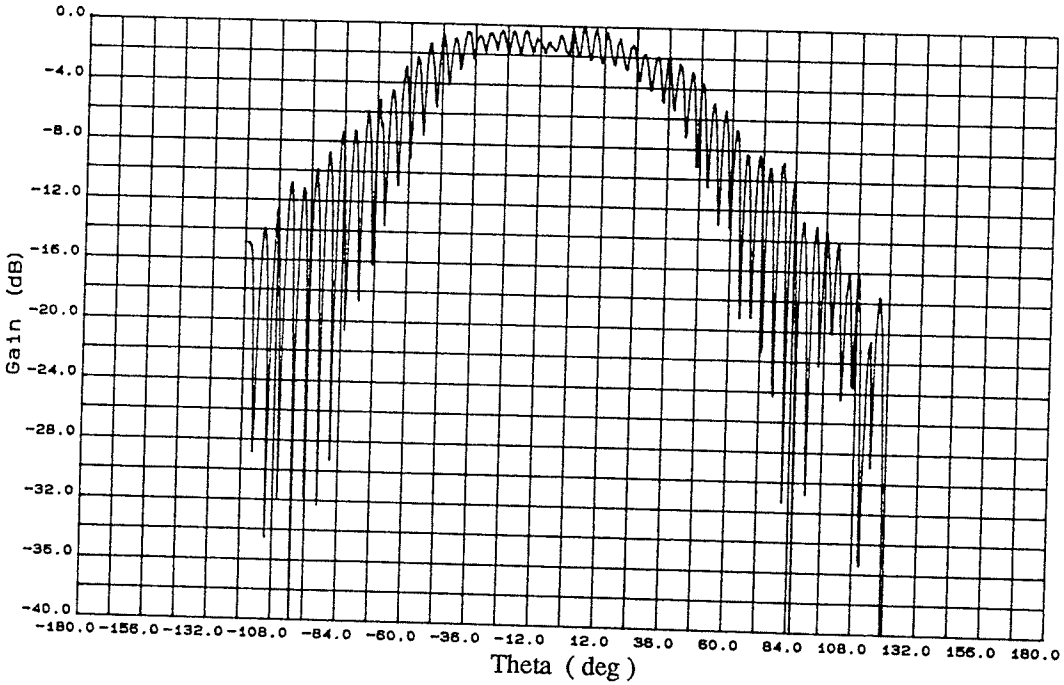

(h) f = 3.2 GHz, Gp = -12.55 dB

Fig. 4.35 (cont.)

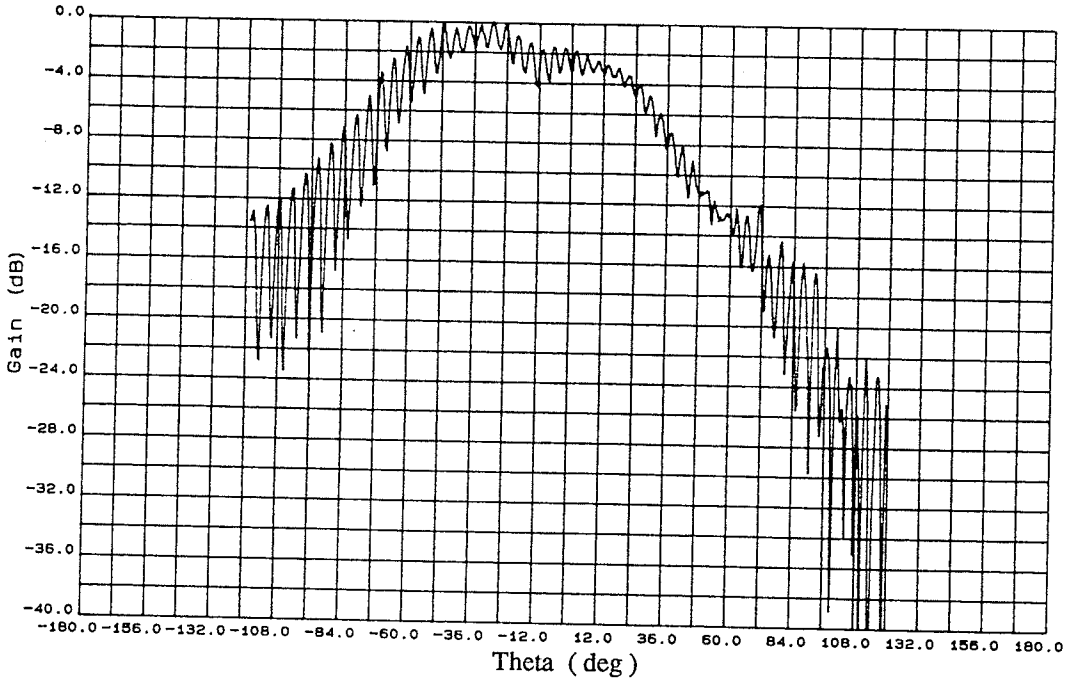

(i) f = 3.35 GHz = f_U,Gp = -14.0 dB

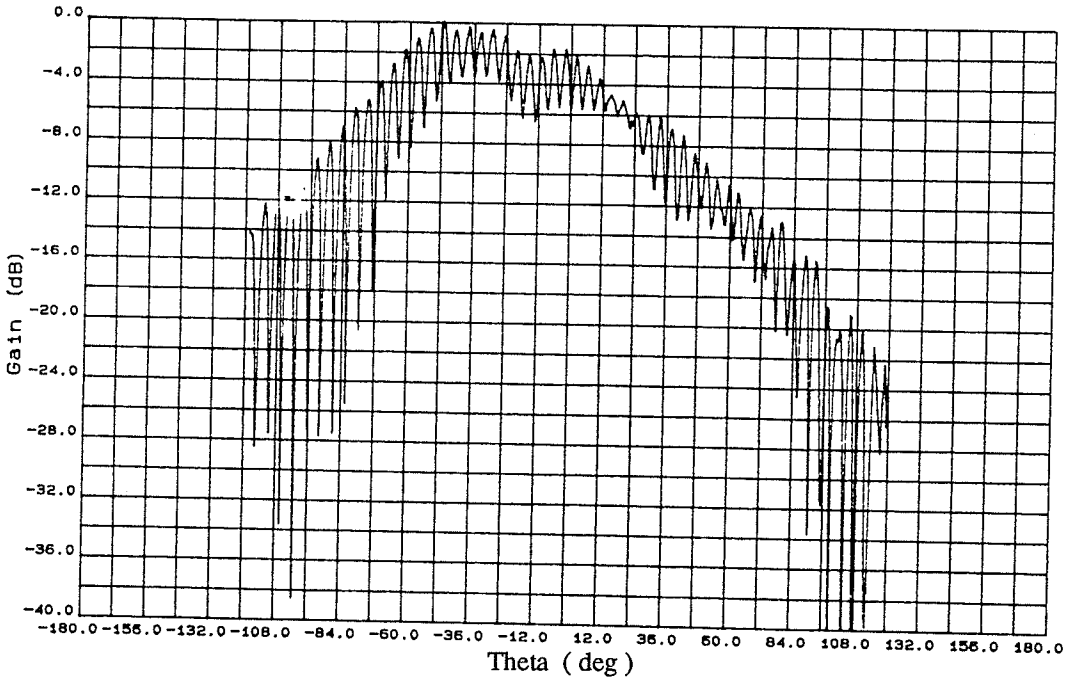

(j) f = 3.4 GHz, Gp = -14.41 dB

Fig. 4.35 (cont.)

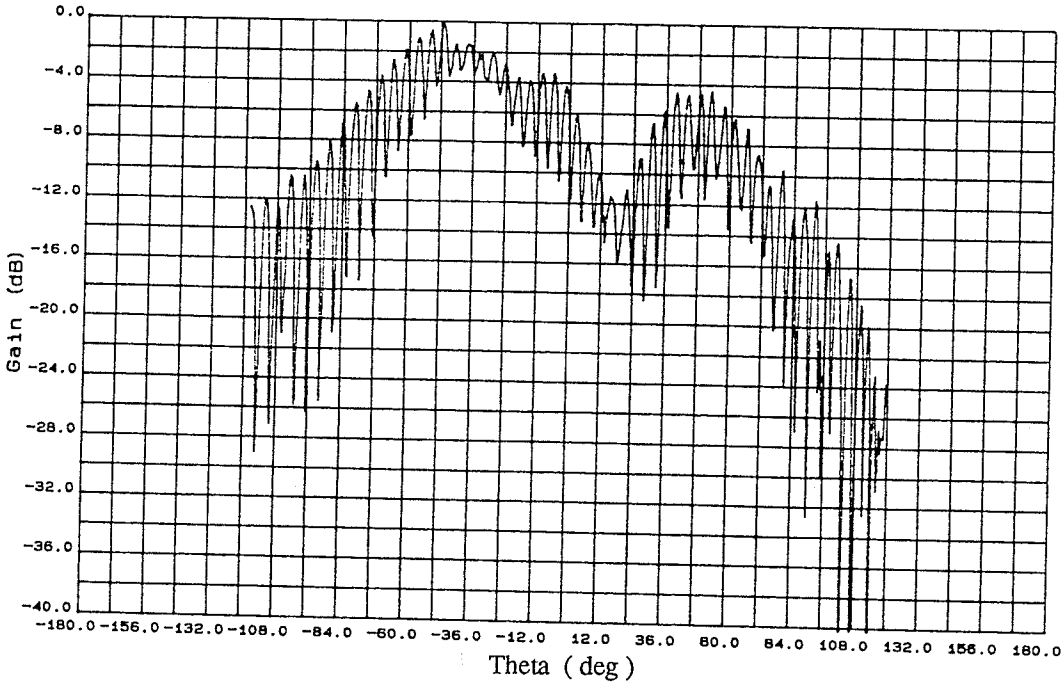

(k) f = 3.5 GHz, Gp = -14.72 dB

Fig. 4.35 (cont.)

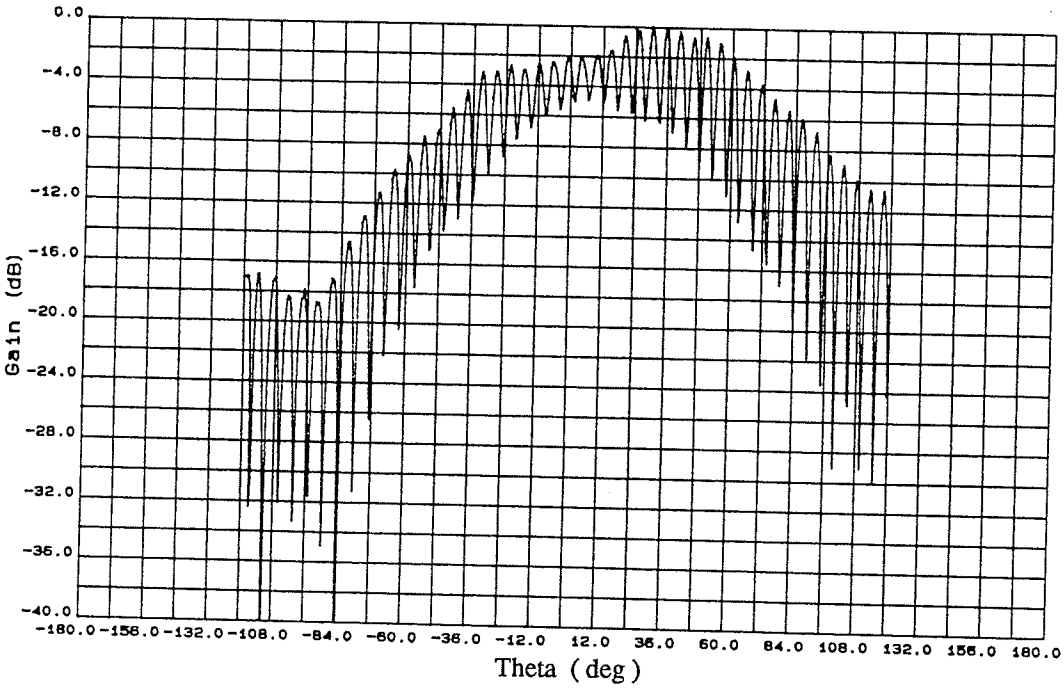

(a) f = 2.9 GHz, Gp = -12.63 dB

Fig. 4.36 : Measured patterns of match terminated 4-arm antenna, $\phi = 45^{o}$

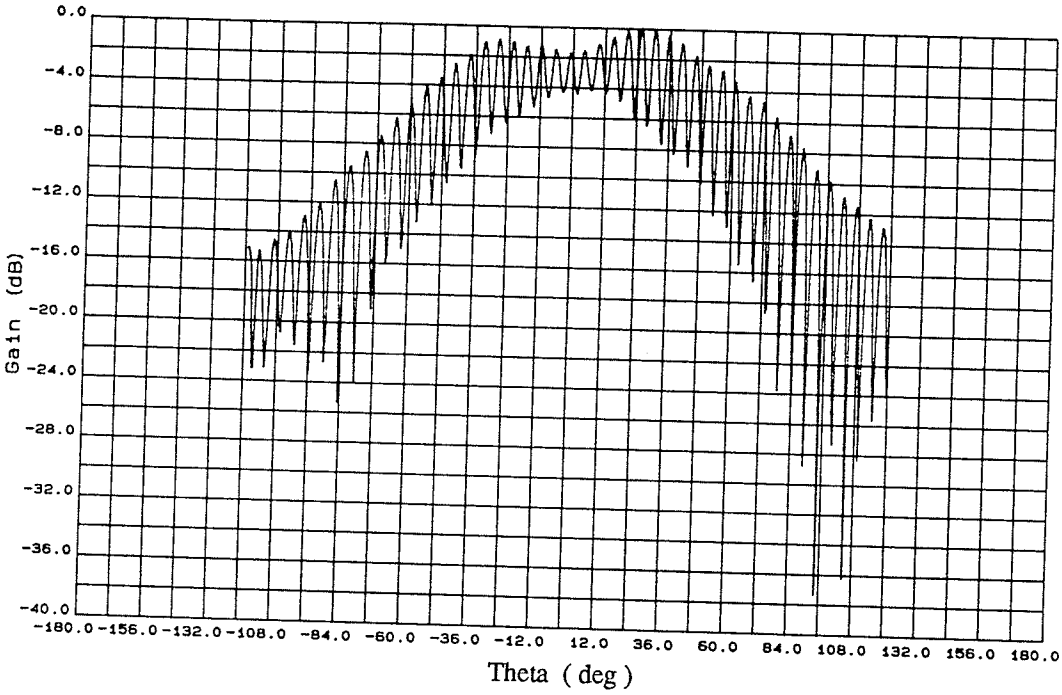

(b) f = 3.0 GHz, Gp = -12.17 dB

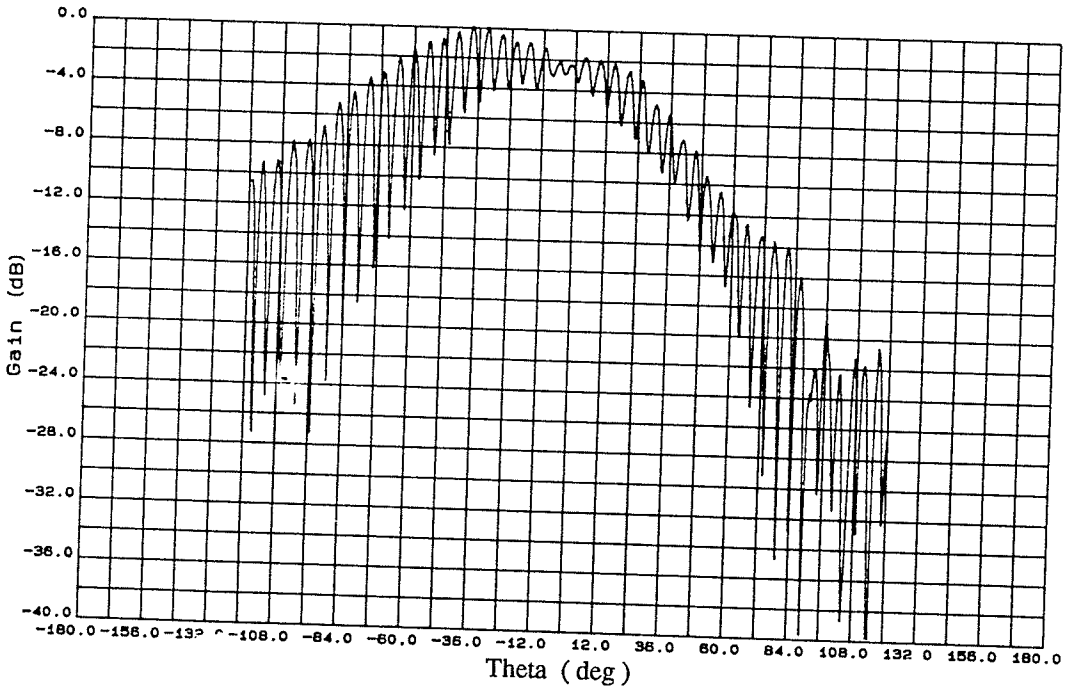

(c) f = 3.2 GHz, Gp = -10.88 dB

Fig. 4.36 (cont.)

4.4.2 4-Arm Antenna : Open Termination

This same antenna was measured with its end left as an open circuit. The return loss was measured and shown in figure 4.37. Due to the open circuit at the end, a large amount of energy is reflected back towards the source. An impedance match was achieved at f = 3 GHz by inserting a three stub tuner between the source and the input of the antenna. Measurements were done over a frequency range from 2.7 GHz to 3.3 GHz. The recorded patterns are given in figure 4.38. The polarization was linear and the components of the E and H plane were measured. Accompanying the pattern plots are vectorial representation of the two components in the E field. The magnitudes are similar to those predicted in figure 4.18 but the phases were not measured. The vectors in figure 4.38 are assumed to have the same phase as in figure 4.18 in order to compare the expected directional changes. Notice that at the impedance matched frequency of 3 GHz, gain increases to -5 dB. Thus the 4-arm antenna with an open termination generates the expected linear polarization characteristics.

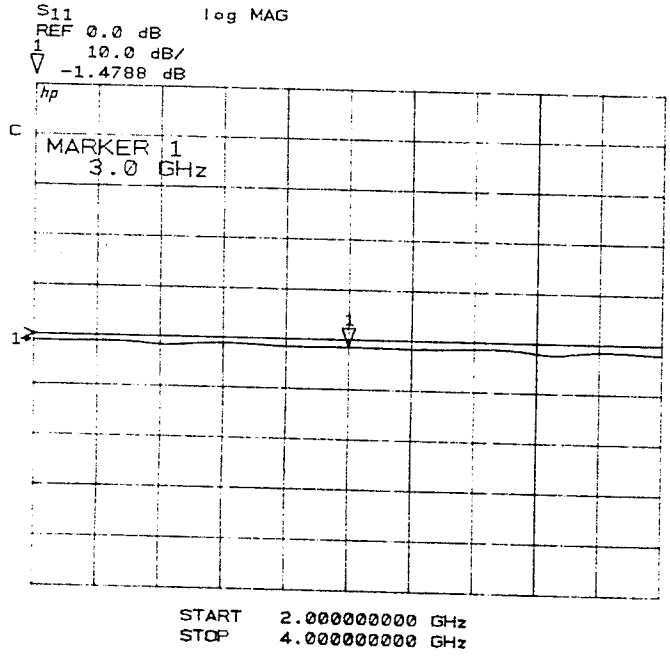

Fig. 4.37 : Return loss of 4-arm antenna with open termination

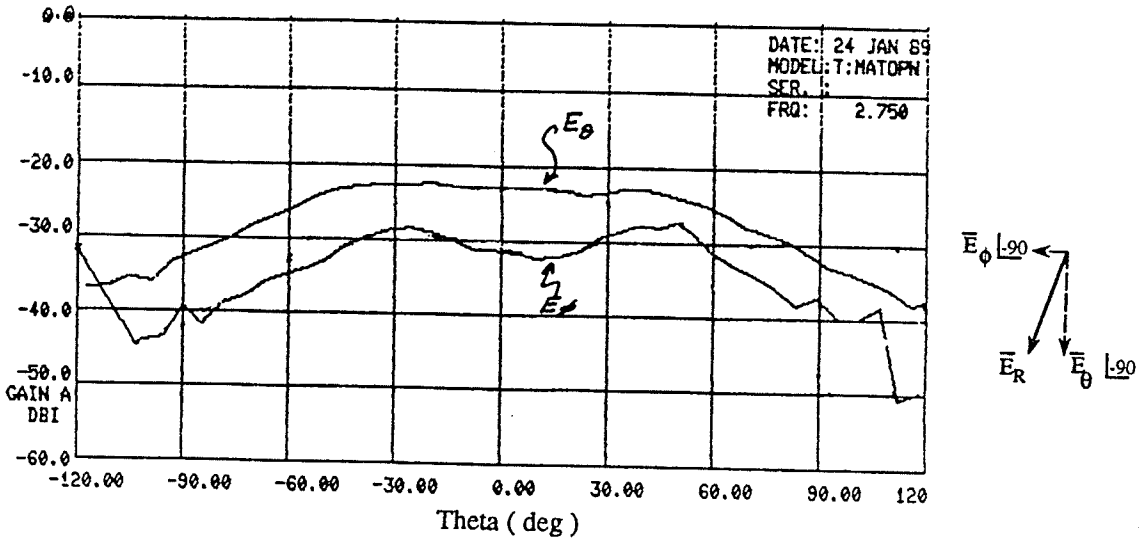

(a) f = 2.75 GHz

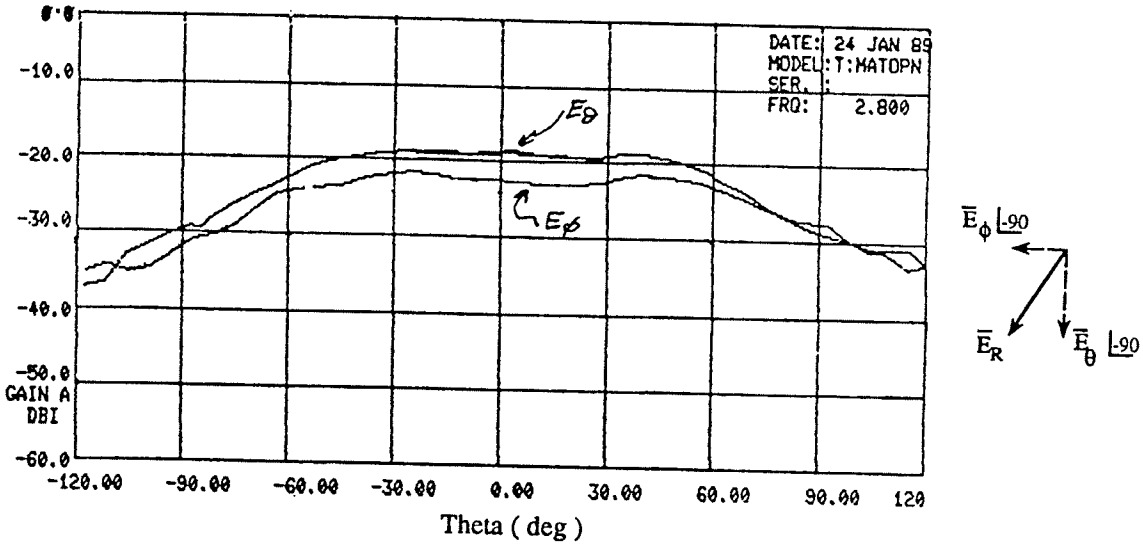

(b) f = 2.8 GHz

Fig. 4.38 : Measured E-plane patterns of open 4-arm antenna, $\phi = 0^{o}$

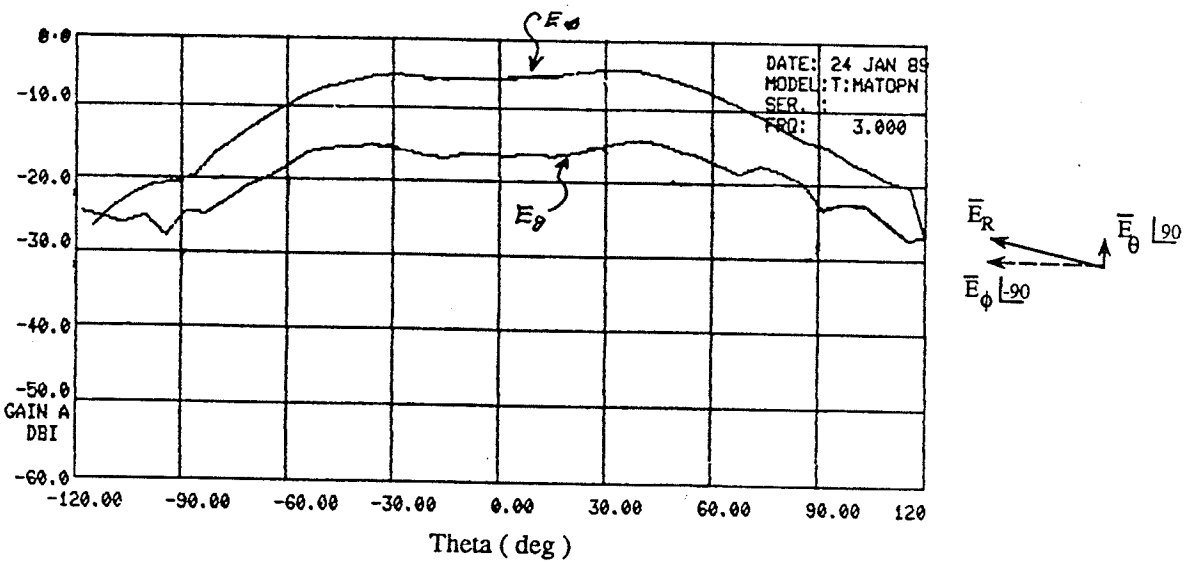

(c) f = 3.0 GHz

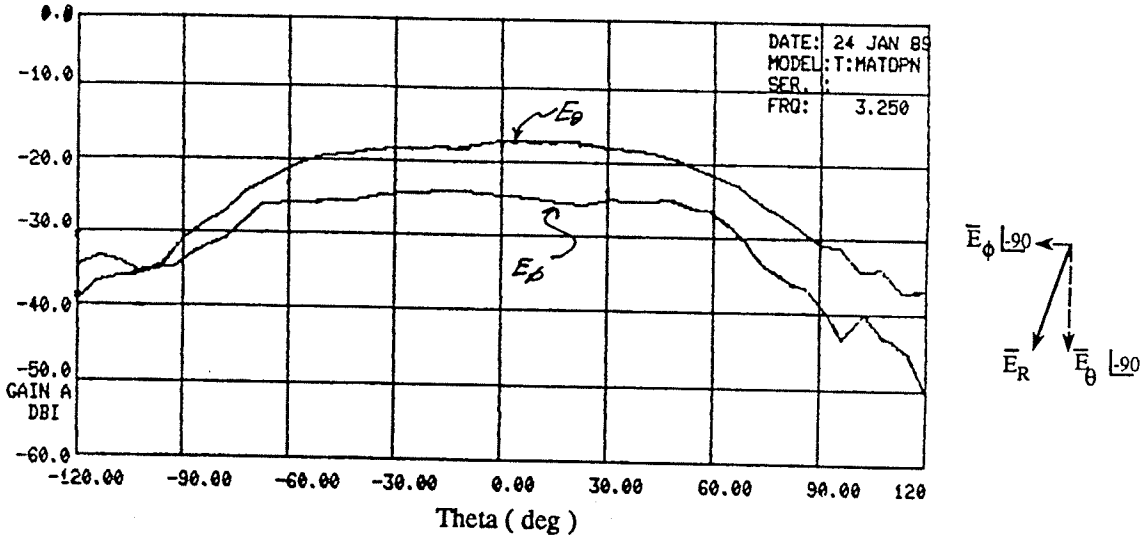

(d) f = 3.25 GHz

Fig. 4.38 (cont.)

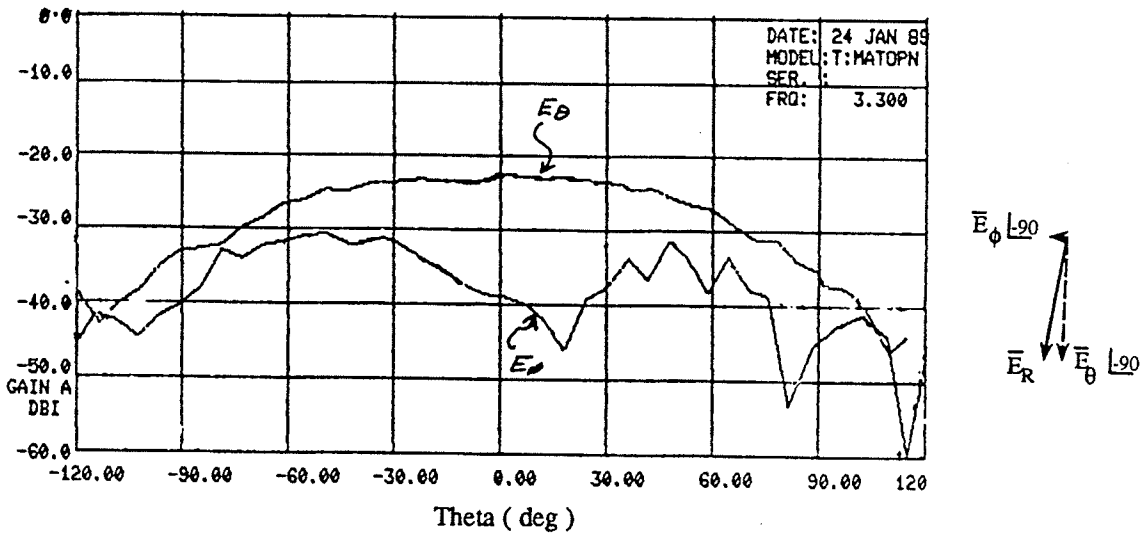

(e) f = 3.3 GHz

Fig. 4.38 (cont.)

4.4.3 4-Arm Antenna : Short Termination

The 4-arm antenna was now terminated with a short circuit. Similar characteristics were noted as the case of the open circuit structure. A return loss of -1.69 dB was recorded and linear polarization was confirmed. A frequency sweep from 2.7 GHz to 3.2 GHz was done in order to observe the direction of linear polarization. Figure 4.39 shows the measured patterns and the vector representation of the linear polarization. Again, the direction of linear polarization varies over frequency and is in agreement with figure 4.19.

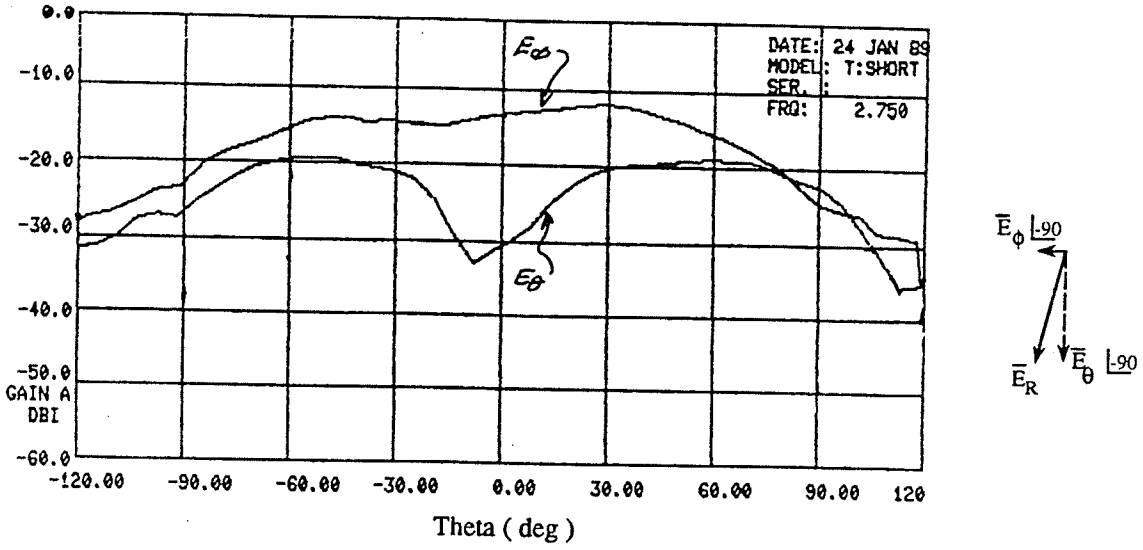

(a) f = 2.75 GHz

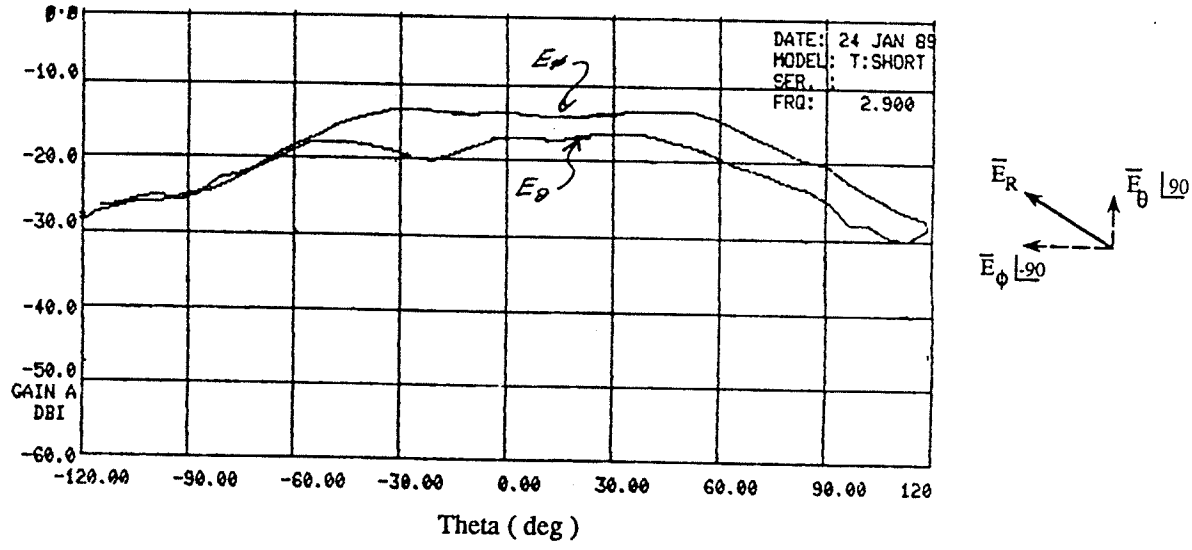

(b) f = 2.9 GHz

Fig. 4.39: Measured E-plane patterns of shorted 4-arm antenna, $\phi = 0^o$

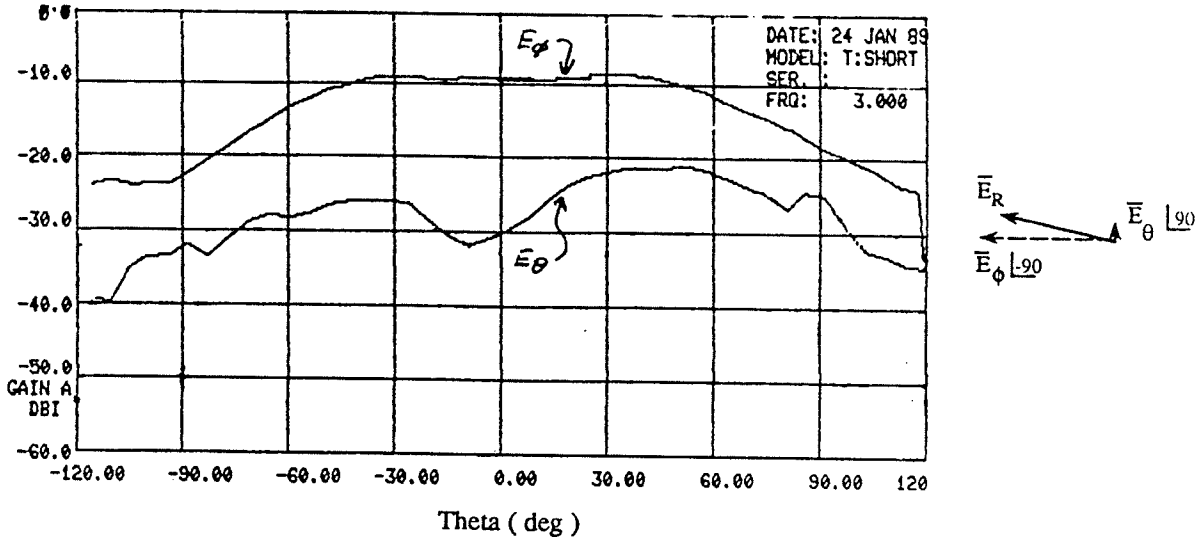

(c) f = 3.0 GHz

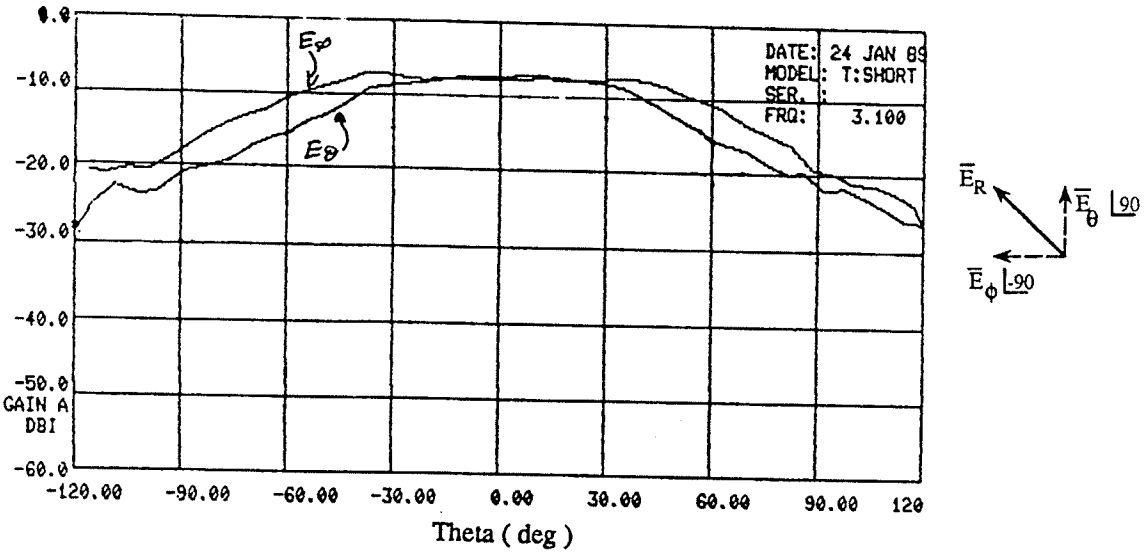

(d) f = 3.1 GHz

Fig. 4.39 (cont.)

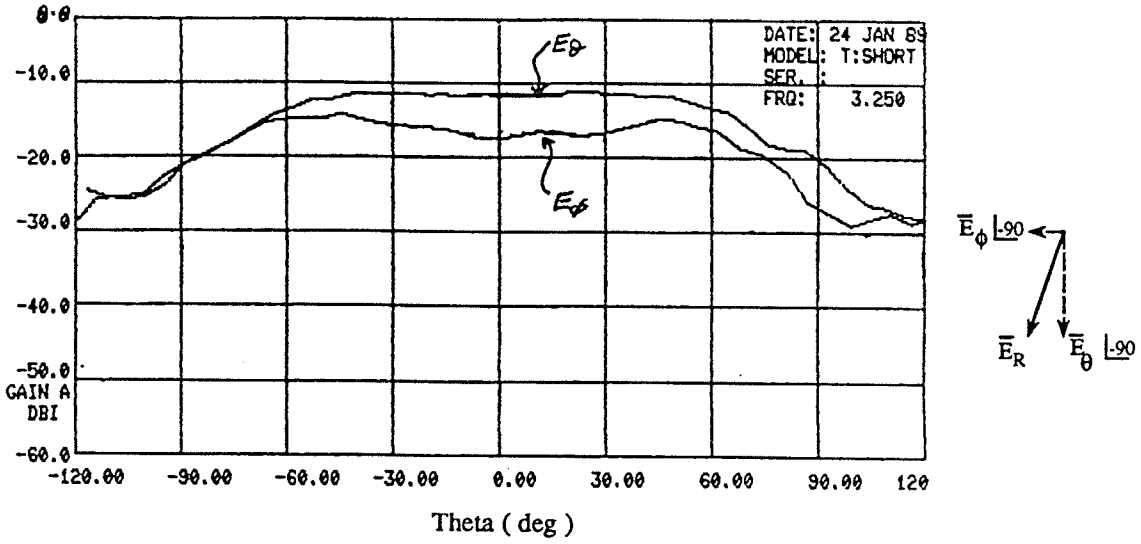

(e) f = 3.25 GHz

Fig. 4.39 (cont.)

4.4.4 4-Arm Antenna with Stubs

The structure indicated in figure 4.23 (a) was fabricated with $\lambda/128$ stubs. The return loss measurements are given in 4.40 (a) and (b) respectively. It can be seen that the return loss maintains a value less than -10 dB from 2.55 GHz to 3.55 GHz. This yields BW_{Zin} = 33.3 %. The insertion loss is shown to be -1.74 dB, an improvement of 1 dB. This indicates that less power is going to the load and hence the efficiency has improved, but not to 98 % as predicted by NEC.

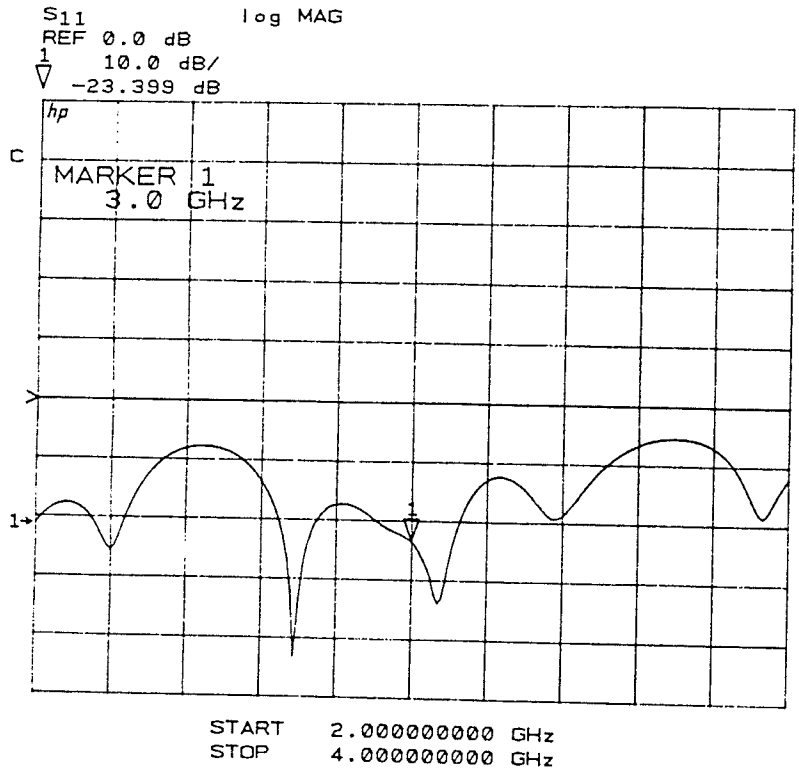

Fig. 4.40 a) : Return loss of the 4-arm antenna with λ/128 stubs

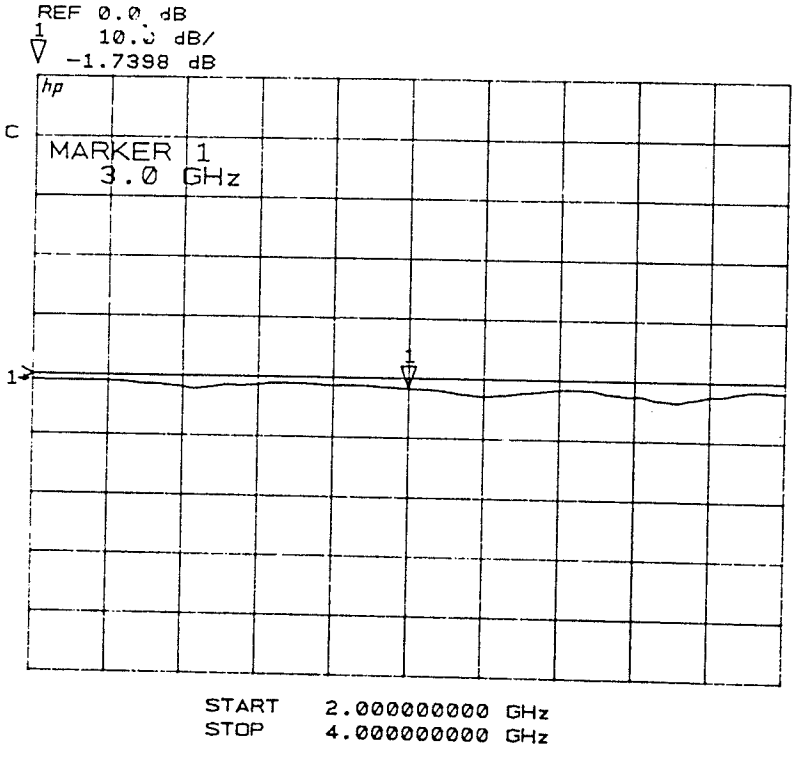

Fig. 4.40 b) : Insertion loss of the 4-arm antenna with λ/128 stubs

The pattern measurement for this structure with λ/128 stubs was not obtained due to damage to the antenna. However, λ/16 stubs were added and the pattern measurements were recorded. A frequency sweep was done to determine if the direction of linear polarization remained constant as frequency varied. The vector representation is given in figure 4.41 which can be compared to figure 4.24. The predicted characteristics agree with those measured, hence the addition of the tabs introduces control over the direction of linear polarization. The last structure studied was the type in figure 4.23 (b).

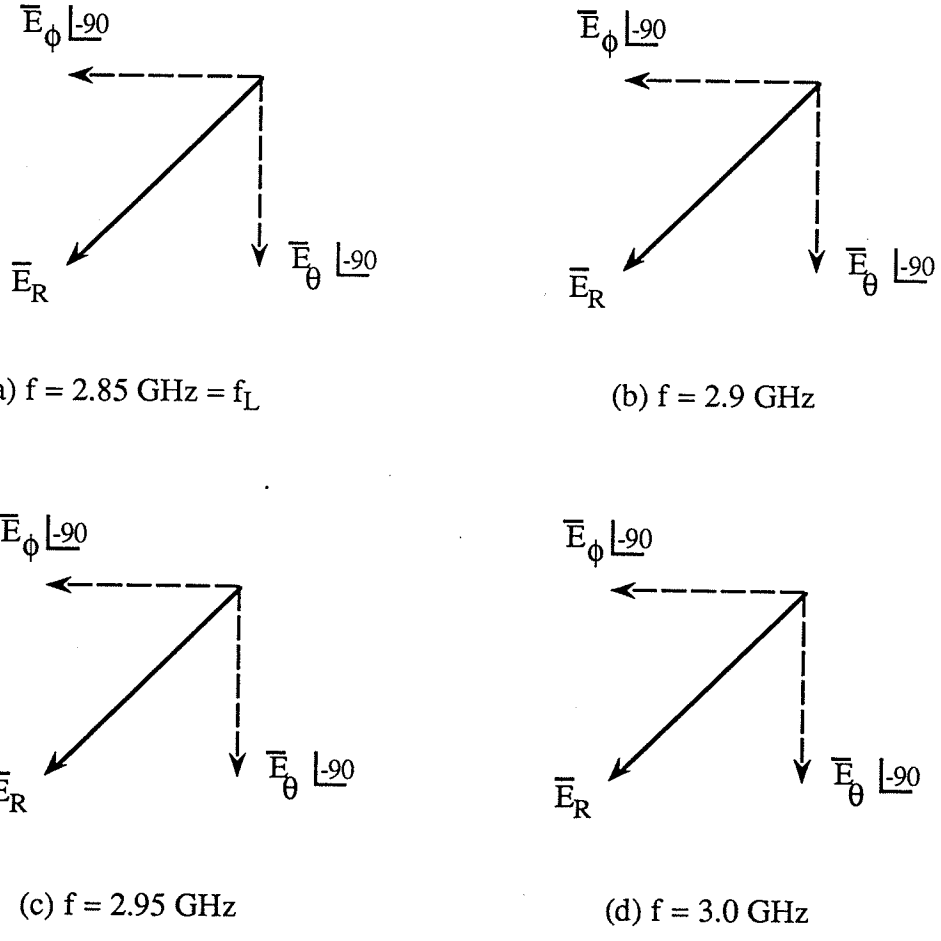

(a) f = 2.85 GHz = f_L

(b) f = 2.9 GHz

(c) f = 2.95 GHz

(d) f = 3.0 GHz

Fig. 4.41 : Vector representation of field components for 4-arms with λ/16 stubs

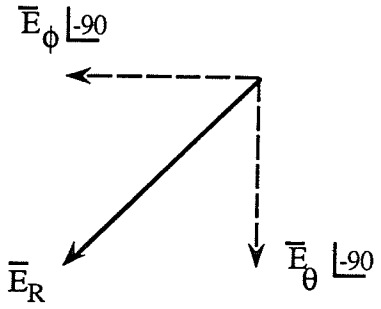

(e) f = 3.05 GHz = f_U

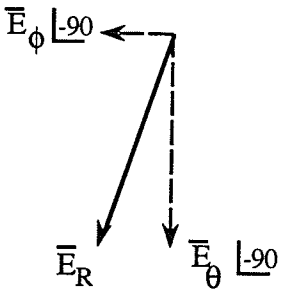

(f) f = 3.1 GHz

4.4.5 4-Arm with Patches

The last structure studied was the four arm structure with patches, of the type in figure 4.23 (b). The structure fabricated and measured is illustrated in figure 4.42. Each arm end increases in width by one line width with progression towards the load.

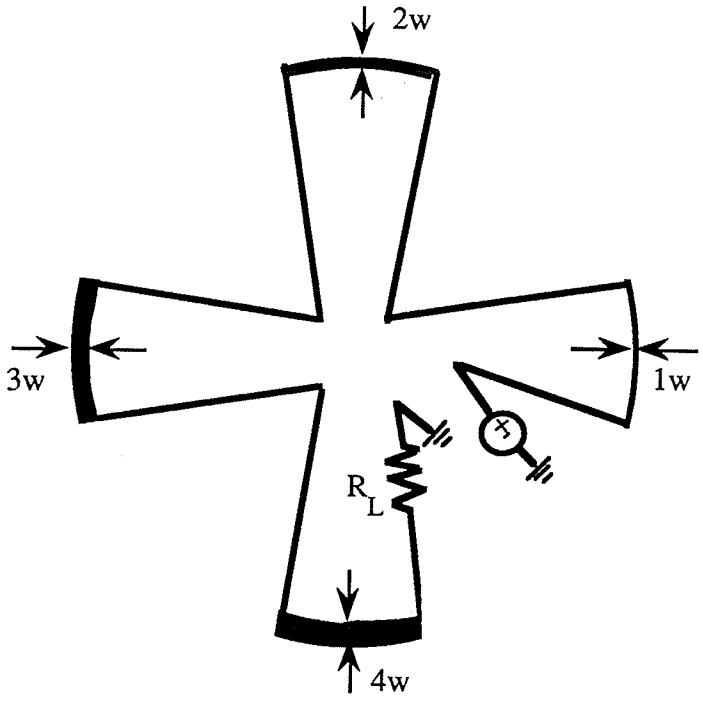

Fig. 4.42 : 4-arm antenna with tapered patches.

Analyzing this antenna on the network analyzer showed a narrow impedance bandwidth of BW_{Zin} = 1.8 %. At the operating frequency of 3 GHz, the return loss was -13 dB, with an insertion loss of -2.5 dB. These are shown in figure 4.43 (a) and (b).

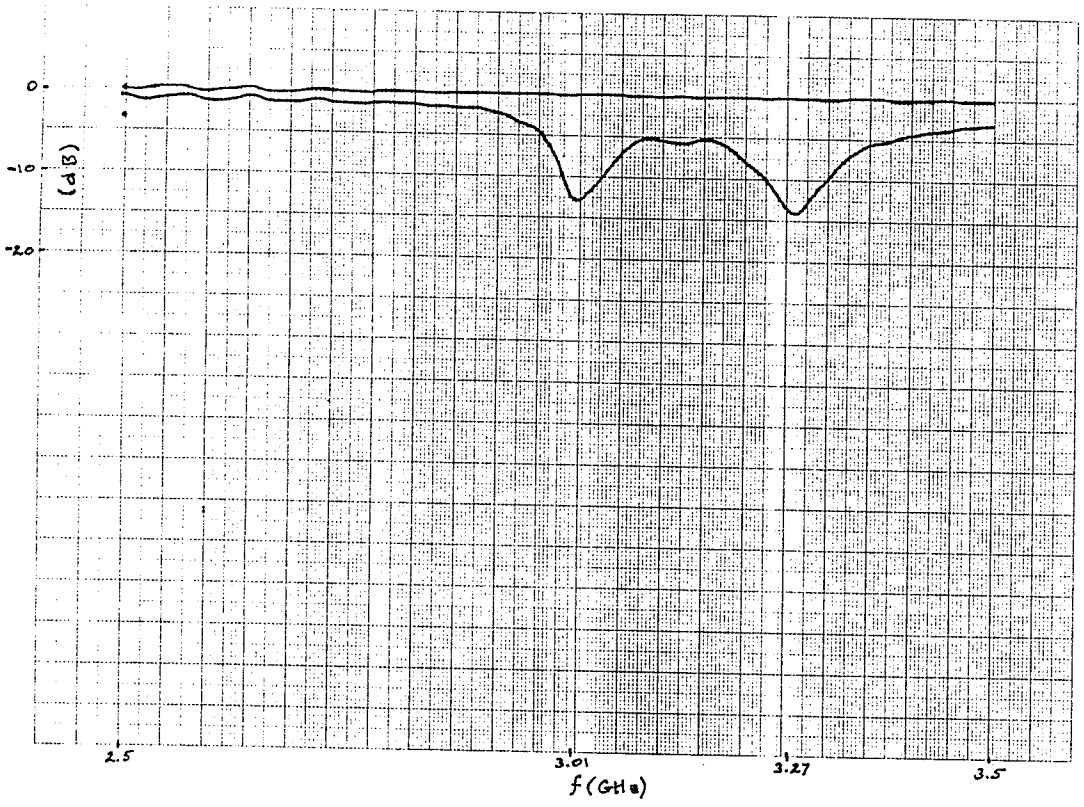

Fig. 4.43 a) : Measured return loss of 4-arm antenna with tapered patches

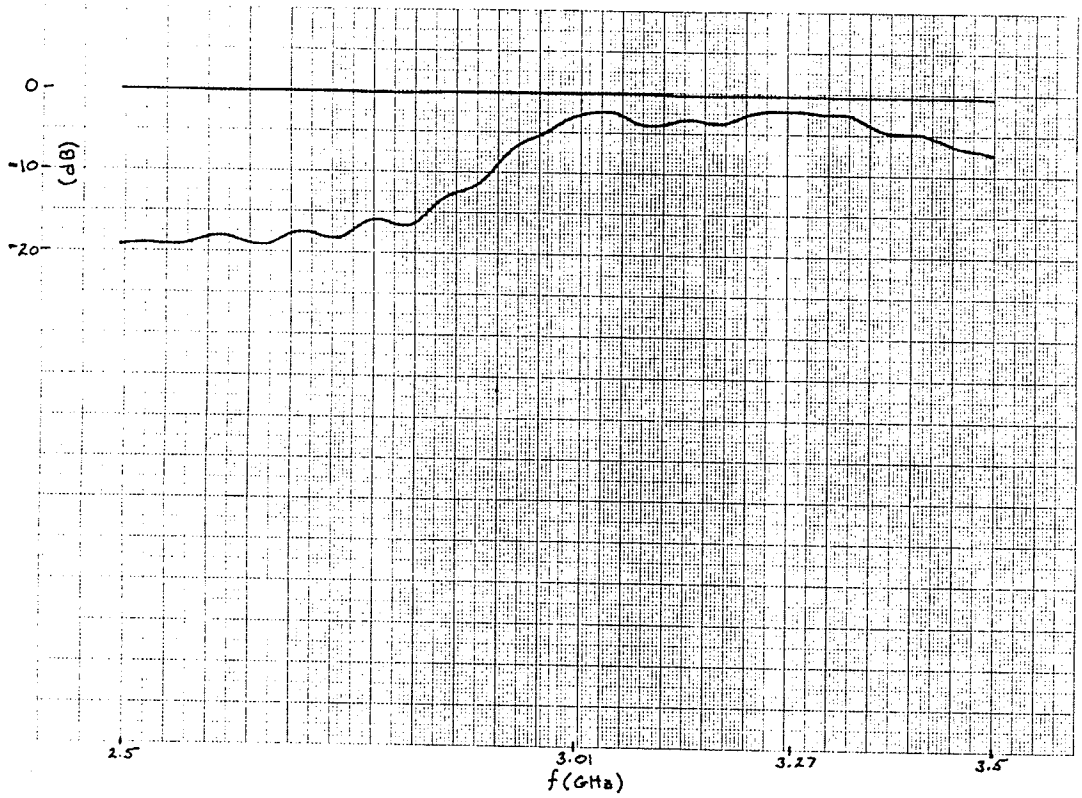

Fig. 4.43 b) : Measured insertion loss of 4-arm antenna with tapered patches

The insertion loss indicates better radiation efficiency which appears a f = 3.05 GHz in the measured patterns shown in figure 4.44. It can be observed that the pattern is relatively constant from f = 2.95 GHz to f = 3.10 GHz yielding a bandwidth of BW_{pat} = 5.0 %. As expected, the pattern degraded outside this bandwidth. In addition, the peak gain at f = 3.05 GHz is -9 dB due to the increase in radiation. Pattern measurements were also taken at $\phi = 45^{o}$ to confirm that the patterns observed were linearly polarized at 45^{o}.

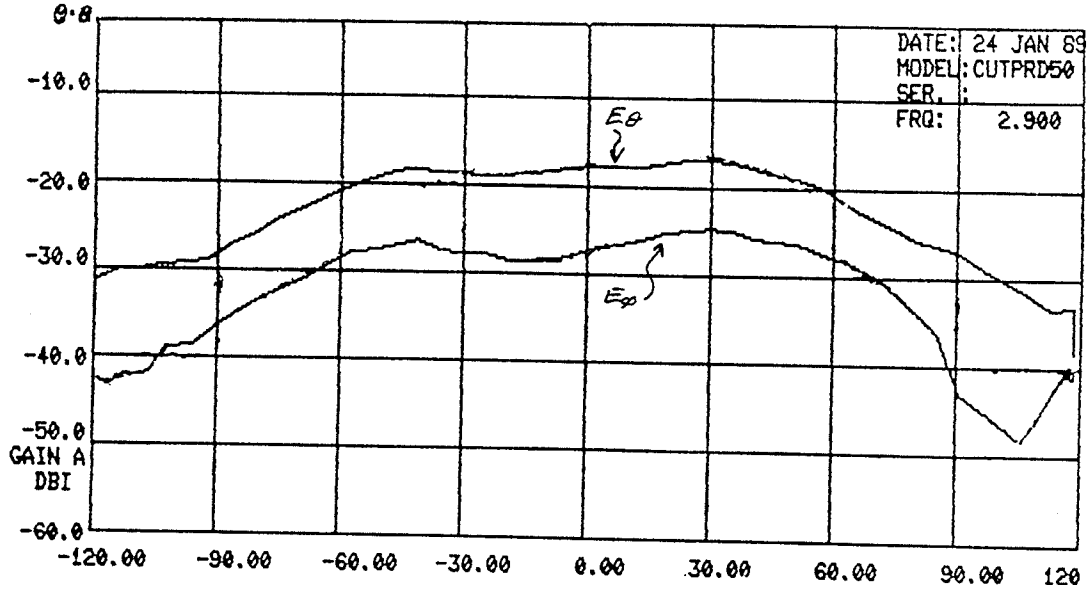

(a) f = 2.9 GHz

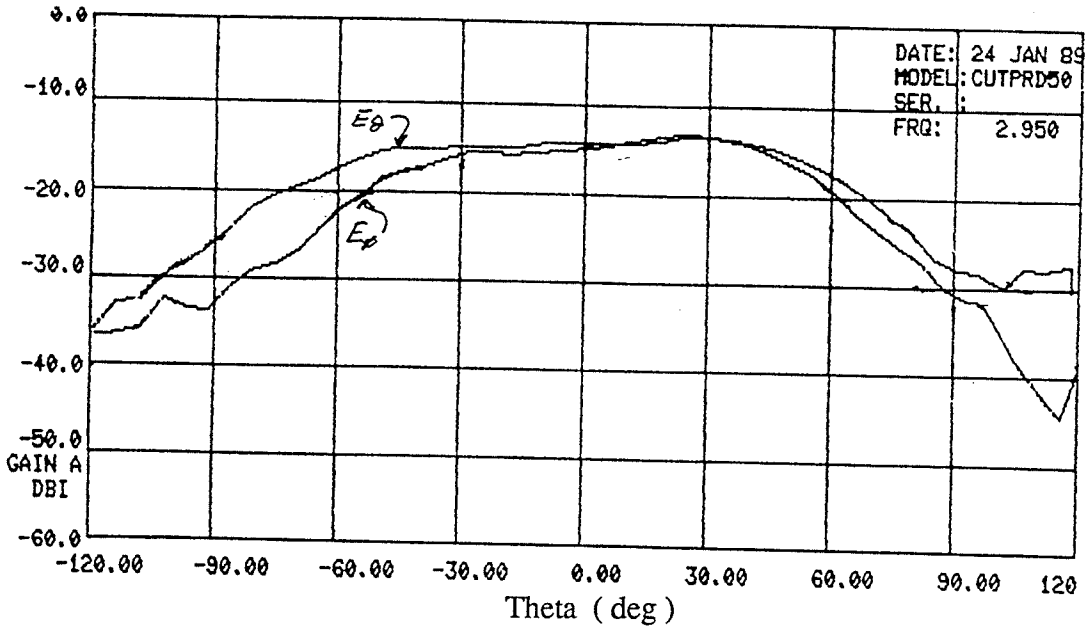

(b) f = 2.95 GHz = f_L

Fig. 4.44 : Measured E-plane patterns of 4-arm antenna with tapered patches, $\phi = 0^o$

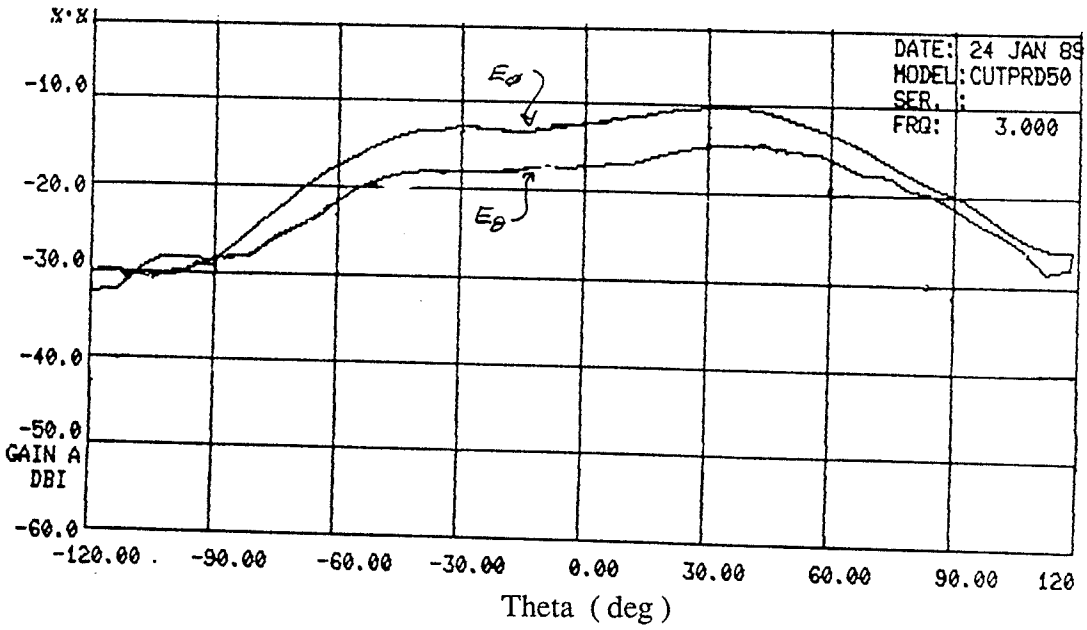

(c) f = 3.0 GHz

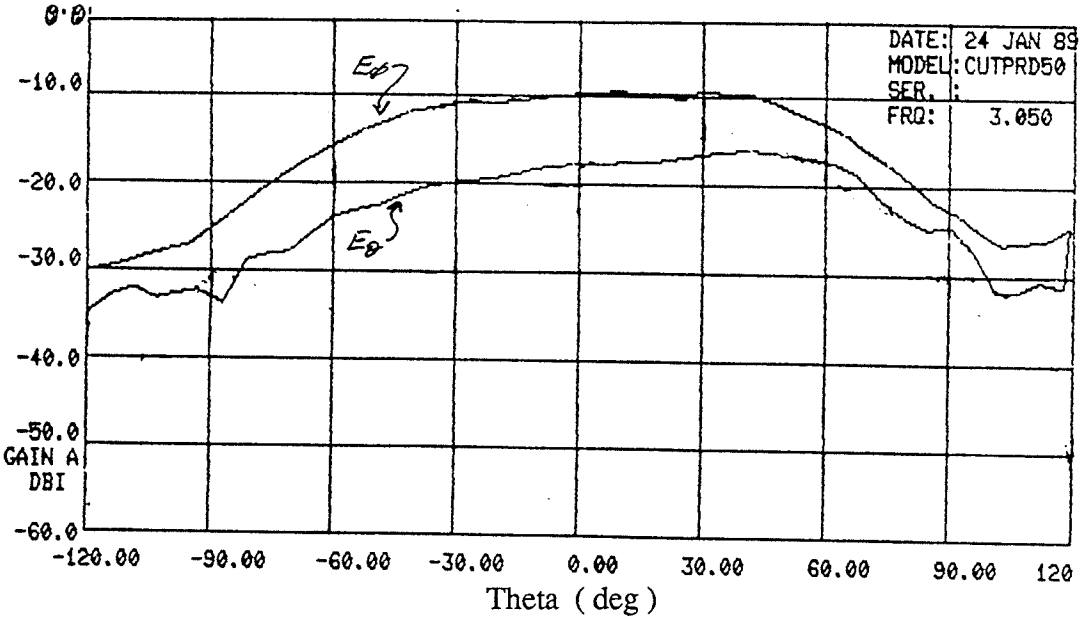

(d) f = 3.05 GHz

Fig. 4.44 (cont.)

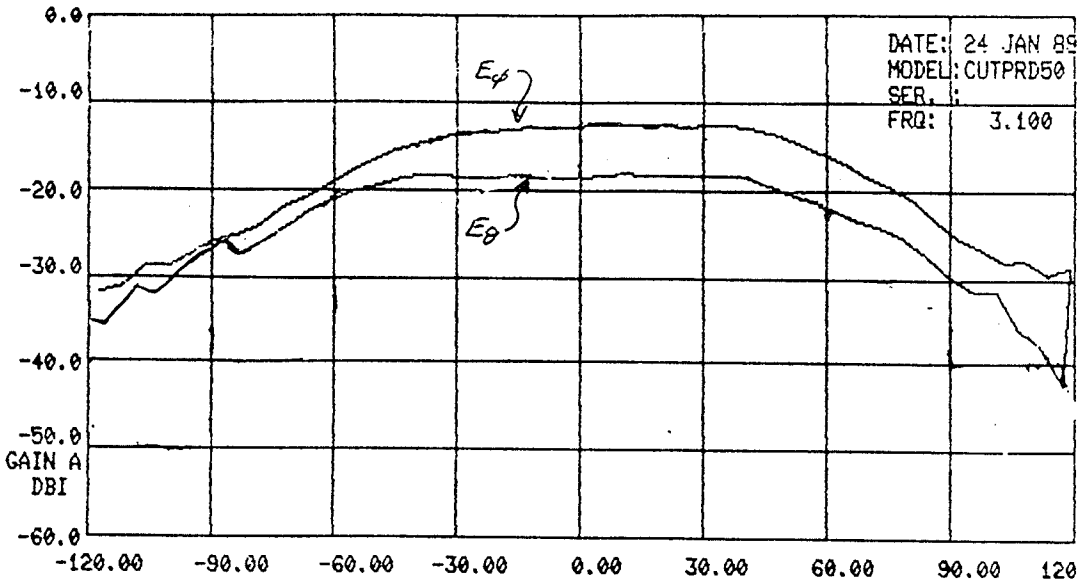

(e) f = 3.1 GHz

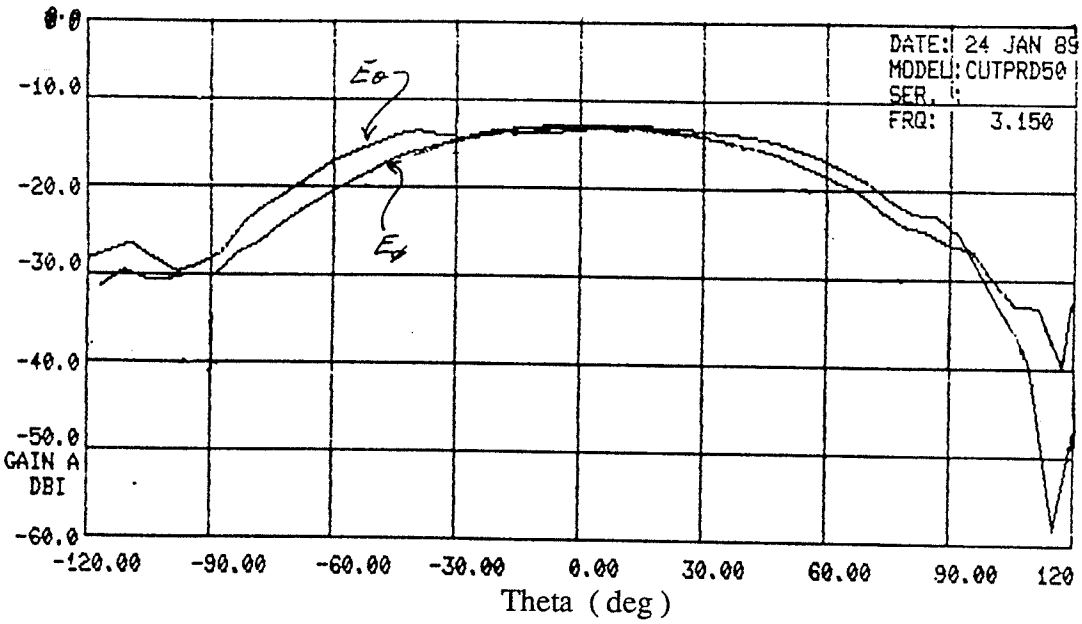

(f) f = 3.15 GHz = f_U

Fig. 4.44 (cont.)

Several 4-arm antenna configurations have been constructed, measured and compared with predicted characteristics and values. A comparison between the analytical and experimental results can now be carried out.

4.5 Discussion

The 4-arm traveling wave antenna designed, built and tested has shown to give a broadside, circular polarized pattern with bandwidths of BW_{pat} = 15 % and BW_{Zin} = 66.7 %. The bandwidths and characteristics measured agree with those predicted but the gain and efficiency do not due to the alumina substrate. At this height (thickness of the alumina), a match loaded structure in free space generates an efficiency of 12 % with a peak gain of 1.1 dB as indicated in figure 4.22. The radiation efficiency with the alumina substrate may be extracted from the measured scattering parameters by examining the total losses in the structure as follows.

At f = 3 GHz, the measured parameters of a loaded 4-arm antenna are:

$$|S_{11}| = -23.5 \text{ dB}$$

$$|S_{21}| = -0.75 \text{ dB}$$

The losses of the structure consist of losses due to radiation and due to the line on a substrate. Hence,

$$P_{loss} = P_{rad} + P_{line} \qquad (4.13)$$

and

$$P_{loss} = P_{in} - P_{out} \qquad (4.14)$$

but $P_{out} = |S_{21}|$ since a good match is obtained with $|S_{11}| = -23.5$ dB

$$10 \log \left(\frac{P_{out}}{P_{in}} \right) = 10 \log |S_{21}|^2 = -.75 \text{ dB}$$

$$\therefore \frac{P_{out}}{P_{in}} = 0.8414 \qquad (4.15)$$

Dividing equation (4.12) by P_{in} yields

$$\frac{P_{loss}}{P_{in}} = 1 - \frac{P_{out}}{P_{in}}$$

Substituting equation (4.13) ,

$$\frac{P_{loss}}{P_{in}} = 0.1586 \qquad (4.16)$$

The line losses may be determined by either modelling the structure on a microwave CAD program or calculating empirically. The calculations are as shown.

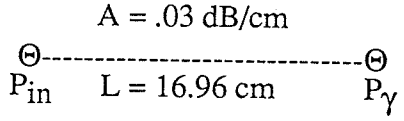

where L is the length of the antenna

A is the attenuation along a line on 25 mil thick alumina

$$\frac{P_\gamma}{P_{in}} = e^{-2\alpha L} = -.03 \text{ dB/cm}$$

where α is the attenuation constant

$$10 \log \frac{P_\gamma}{P_{in}} = -.03(16.96)$$

$$10 \log \frac{P_\gamma}{P_{in}} = -.5088 \text{ dB} = |S_{21}| \qquad (4.17)$$

$$\frac{P_\gamma}{P_{in}} = 0.8895$$

but $P_{line} = P_{in} - P_\gamma$

$$\frac{P_{line}}{P_{in}} = 1 - \frac{P_{\gamma}}{P_{in}}$$

$$\therefore \frac{P_{line}}{P_{in}} = 0.11055$$

The 4-arm antenna was also modelled using the CAD program Touch Stone resulting in $|S_{21}| = -0.545$ which is fairly close to equation (4.17). This value is actually more accurate since it includes the losses due to the corners. Thus the line loss will be based on this value, resulting in

$$\frac{P_{line}}{P_{in}} = 0.1179 \qquad (4.18\ a)$$

$$P_{loss} = P_{rad} + P_{line}$$

$$\frac{P_{loss}}{P_{in}} = \frac{P_{rad}}{P_{in}} + \frac{P_{line}}{P_{in}}$$

$$\frac{P_{rad}}{P_{in}} = 0.0407 \qquad (4.19)$$

The experimental results have shown that only 4.1 % of the input power is radiated. Thus the introduction of the alumina substrate further reduces efficiency by approximately 9 % in comparison to the antenna in free space. The measured gain when loaded is -11 dBi and -3 dBi when terminated with an open circuit. The measured gain for the match terminated case can be verified by extrapolating the data from the analysis in free space to one which includes a dielectric substrate. The values taken from the analysis which includes a dielectric substrate are based upon experimental measurements while those taken from the analysis in free space are based upon the numerical values generated by NEC. Note that the physical size of the structure on a dielectric substrate is smaller than the equivalent structure in free space. This is because of the smaller effective wavelength due to the alumina substrate. Since the physical size is smaller, the corresponding gain will be less than the larger structure in free space. This has been incorporated in the verification that

follows. The maximum gain possible may be determined from equation (4.10) where $\lambda = \lambda_o$, thus

$$G_{max}^{\varepsilon_o} = \frac{4\pi A}{\lambda_o^2}$$

where A is the aperture area

$$A = \pi (.596\lambda_o)^2$$

$$\therefore G_{max}^{\varepsilon_o} = 14.02 \equiv 11.47 \text{ dB}$$

The introduction of a ground plane allows an addition of 3 dB to the gain maximum, thus

$$\therefore G_{max}^{\varepsilon_o} = 14.47 \text{ dB} \equiv 27.98$$

This may be compared to the case where the end termination was an open circuit and close to 100 % efficiency was observed. This yielded a peak gain of 12.86 dB. Gain is related to the aperture area which is dependent upon the effective permittivity as shown below.

$$A^{\varepsilon_o} = \pi (.596\lambda_o)^2 \quad \text{and} \quad A^{\varepsilon_{eff}} = \pi \left(.596 \frac{\lambda_o}{\sqrt{\varepsilon_{eff}}} \right)^2$$

$$= \pi (.596)^2 \frac{\lambda_o^2}{\varepsilon_{eff}^2}$$

thus

$$\frac{A^{\varepsilon_{eff}}}{A^{\varepsilon_o}} = \frac{1}{\varepsilon_{eff}}$$

$$A^{\varepsilon_{eff}} = \frac{A^{\varepsilon_o}}{\varepsilon_{eff}}$$

It has been determined by equation (3.2 c) that $\varepsilon_{eff} = 6.71$ for this structure having $\varepsilon_r = 9.8$

$$\therefore A^{\varepsilon_{eff}} = 0.149\, A^{\varepsilon_o}$$

hence

$$G^{\varepsilon_{eff}} = 0.149\, G^{\varepsilon_o}$$

The gain of this structure on an alumina substrate can now be determined to be

$$G_{max}^{Al} = 0.149\ (\ 27.98\ ) = 4.17 \equiv 6.2\ dB$$

If 4.1 % of the total power was radiated, then the gain would be

$$G^{Al} = 0.041\ (\ 4.17\ )$$

$$G^{Al} = 0.17 = -7.7\ dB$$

The measured gain, G_m^{Al}, was found to be -11.1 dB at a frequency of 3.05 GHz. However, this was measured with a rotating linear source, thus 3 dB should be added to the measured gain, therefore G_m^{Al} = -8.1 dB. A 0.4 dB discrepancy exists which may be accounted for by gain calculation errors because the effective aperture area was not included. Thus, gain has been decreased by a factor of 6.7 when placed on alumina. This decrease in gain has a corresponding broadening effect on the 3 dB beamwidth. The calculated beamwidth may be determined from the definition of directivity given in equation 4.18.

$$D = \frac{4\pi}{\Omega_A} \qquad (4.20)$$

where Ω_A is the element solid angle

$$\Omega_A = \theta_{3dB}\ \phi_{3dB}$$

where θ_{3dB} and ϕ_{3dB} are the 3dB beamwidths

If G ≅ D, then to achieve a maximum gain of 14.47 dB in free space, the required element solid angle is

$$27.98 = \frac{4\pi}{\Omega_A}$$

$$\therefore\ \Omega_A^{\varepsilon_o} = 0.449$$

Both theta and phi beams where observed to be nearly identical, thus $\theta_{3dB} = \phi_{3dB}$

$$\therefore\ \theta_{3dB}^{\varepsilon_o} = \phi_{3dB}^{\varepsilon_o} = 38.4°$$

The 3 dB beamwidth recorded was 40^{o} which shows good agreement. The alumina substrate decreased the free space gain to 6.2 dB. The corresponding 3 dB beamwidth is calculated to be

$$G_{max}^{Al} \cong D = \frac{4\pi}{\Omega_A^{Al}}$$

$$\Omega_A^{Al} = 3.014$$

which yields $$\theta_{3dB}^{Al} = \phi_{3dB}^{Al} = 99.5^{\circ}$$

The measured 3dB beamwidth as shown in figure 4.35 is 90^{o}. Thus the measured broad beamwidth and low gain values coincide with expected results.

Similar calculations were performed with the structures having stubs and tapered patches at the ends of each arm. The radiation efficiencies were measured to be 30 % for the stub structure and 33 % for the tapered patches. Based on these efficiencies, the expected gains calculated from the maximum aperture gain, are 0.97 dB and 1.3 dB for the stub and tapered patch structure respectively. The measured values were both approximately -9.0 dB. The gross differences seen here may be accounted for by the added geometries. Linearly polarized patterns are produced which indicate a variation from the 2π phase progression, thus it is conceivable that the radiated energy is not added in phase. This in turn would result in lower gain values. For these reasons, a comparison of gain values between analytical and measured results can not be performed.

Therefore it can be concluded that the theoretical design and analysis of this type of traveling wave antenna is in good agreement with experimentally measured results. This antenna satisfies the relatively large bandwidth requirements. However, it has also been shown that a problem exists in terms of the radiation efficiency. In addition, the fabrication of this antenna is well suited for monolithic applications where conformal arrays are required.

CHAPTER 5 : Microstrip Patch Antennas

With the study of a traveling wave antenna completed, microstrip patch antennas will now be examined. As outlined in Chapter 3, a microstrip patch antenna has a narrow impedance bandwidth which is decreased further when placed on a thin, high relative permittivity substrate. One scheme previously mentioned was a conically depressed circular patch for which an impedance bandwidth of 28.7 % was obtained for a depression angle of 5^{o} ($\varepsilon_r = 2.5$, h = 6 mm, $f_o = 2.98$ GHz), where the depression angle is defined as the angle from the edge of the cone to its centre (see figure 5.1). In addition, a further increase in bandwidth was reported as the depression angle increased. With such a large reported bandwidth, this structure showed promise for substrates with high relative permittivities.

5.1 : Conically Depressed Circular Microstrip Patch Antenna

A conically depressed circular microstrip patch antenna was first studied by Das and Chatterjee [43]. The structure studied is shown in figure 5.1.

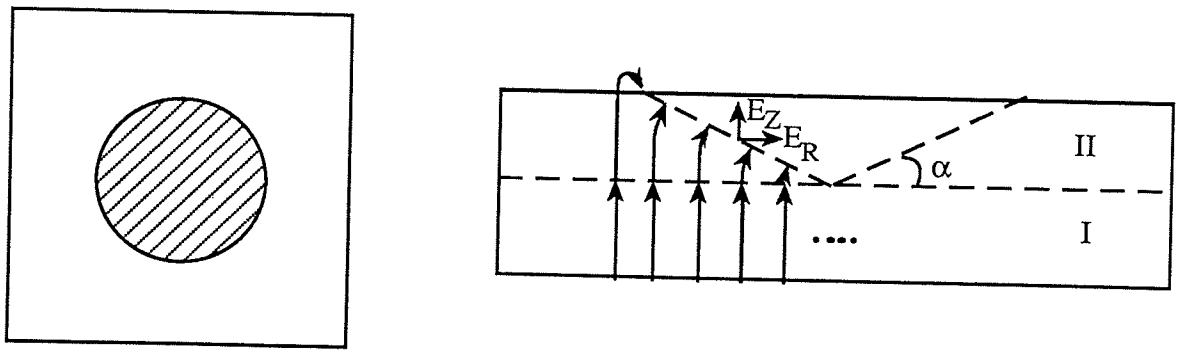

Top View

Side View

Fig. 5.1 : Conically depressed circular microstrip patch antenna

In order to determine the radiation properties of this type of structure, the field structure in the cavity below the patch is required. When the angle of depression is zero, a flat circular patch is formed which has been analyzed in [31]. The cavity model uses magnetic wall boundary conditions on the edges. Assuming a constant electric field in the z-direction, the resulting cavity fields have been found to be transverse magnetic (TM) given in equation (5.1) in cylindrical coordinates.

$$E_\rho = 0 \qquad H_\rho = \frac{-jn}{\omega \mu \rho} E_o J_n(k\rho) \sin n\phi \tag{5.1}$$

$$E_\phi = 0 \qquad H_\phi = \frac{-jk}{\omega \mu} E_o J_n'(k\rho) \cos n\phi$$

$$E_z = E_o J_n(k\rho) \cos n\phi \qquad H_z = 0$$

A problem in carrying out the analysis arises as the angle of depression increases from zero degrees. As can be seen in figure 5.1, there is a dependence on theta, hence the cavity fields should be solved in terms of spherical coordinates, which is not an easy task. To avoid this difficulty, Das [43], divided the cavity into two regions. The lower region assumes a constant electric field in the z-direction and hence the equations in (5.1) are used. The upper region, shown as region 2, contains both TM and TE modes. The total power radiated is the sum of the power radiated in the TM mode by E_z and the power radiated in the TE mode by H_z. The tangential component of the electric field along the depressed surface is zero. The radiation is normal to the surface, hence an additional field is present and is shown in figure 5.1 as E_r. Equation (3.1) indicates that increasing the radiation losses will increase BWzin which is the effect of having an additional field component E_r.

This structure was studied experimentally. The conical depression was milled on a 2.0" x 2.0" x .05" piece of stycast having $\varepsilon_r = 10$. A mask was fabricated and the pattern

on the mask was etched on the piece of metalized stycast. This was done for depression angles of 5^o, 10^o, and 15^o , as well as for a flat patch. The aperture remained constant with a radius of 4.63 mm for all cases. The return loss of each antenna was measured on an HP 8510 Network Analyzer and is presented in figure 5.2. The input impedance bandwidth for each variation in alpha was determined and plotted in figure 5.3 (a). A flat disc was expected to have a bandwidth close to the measured 1.6 % and it can be seen that BW_{Zin} increases by a factor of 2.4 when the angle of depression is 15^o. The change in resonant frequency is interesting, as the aperture area remained constant. Figure 5.3 (b) shows the increase in frequency as alpha increases. For the case of alpha equal to zero, the theoretical resonant frequency may be determined from the effective aperture radius determined from [31].

$$a_e = a\left[1+\frac{2h}{\pi a \varepsilon_r}\left(\ln\left(\frac{\pi a}{2h}\right)+1.7726\right)\right]^{\frac{1}{2}} \qquad (5.2)$$

where a is the disc radius of 4.634 mm

$h = 1.27$ mm

$\varepsilon_r = 10$

$$\therefore\ a_e = 4.77 \text{ mm}$$

A radius of a_e yields a resonant frequency of $f_r = 5.8$ GHz. The discrepancy between that and the measured frequency of 5.65 GHz is due in part to the fabrication process because it was unclear how the process affected the stycast material. However, it can still be determined that the frequency increased by a factor of 1.2 with the aperture area remaining the same. As the angle of depression increases, the centre portion of the patch approaches the ground plane. This creates an area which has strong coupling to the ground plane, thus the actual active area of the patch decreases causing an increase in the resonant frequency.

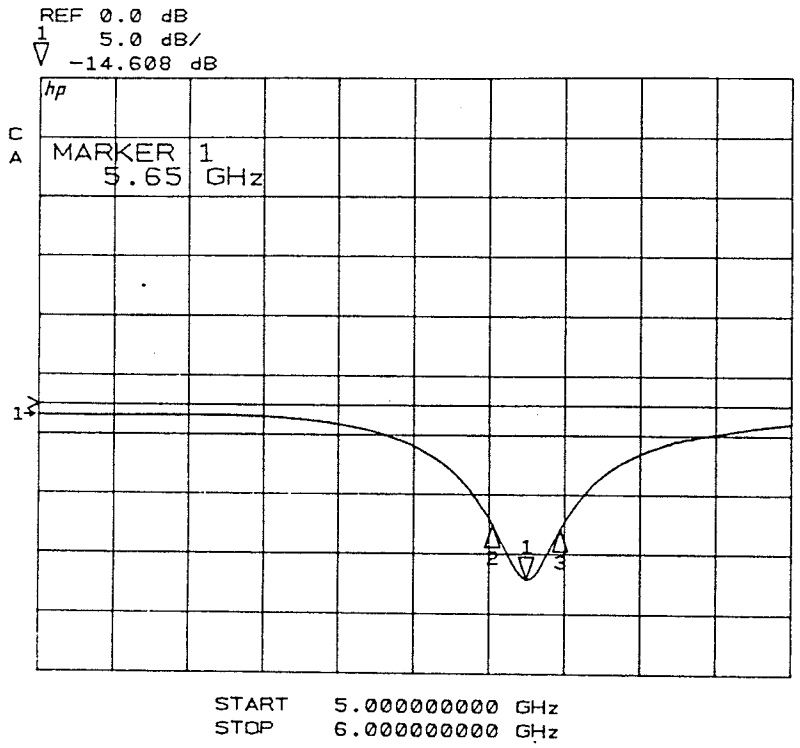

(a) $\alpha = 0^{o}$, $\rho_{feed} = 0.3a$

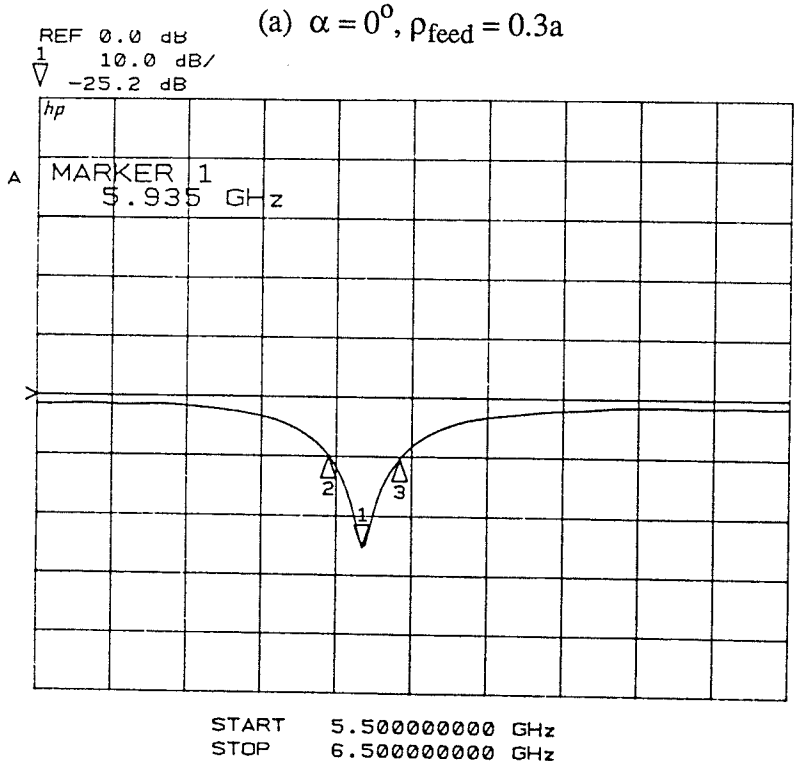

(b) $\alpha = 5^{o}$, $\rho_{feed} = 0.27a$

Fig. 5.2 : Return loss measurements of conically depressed circular patches

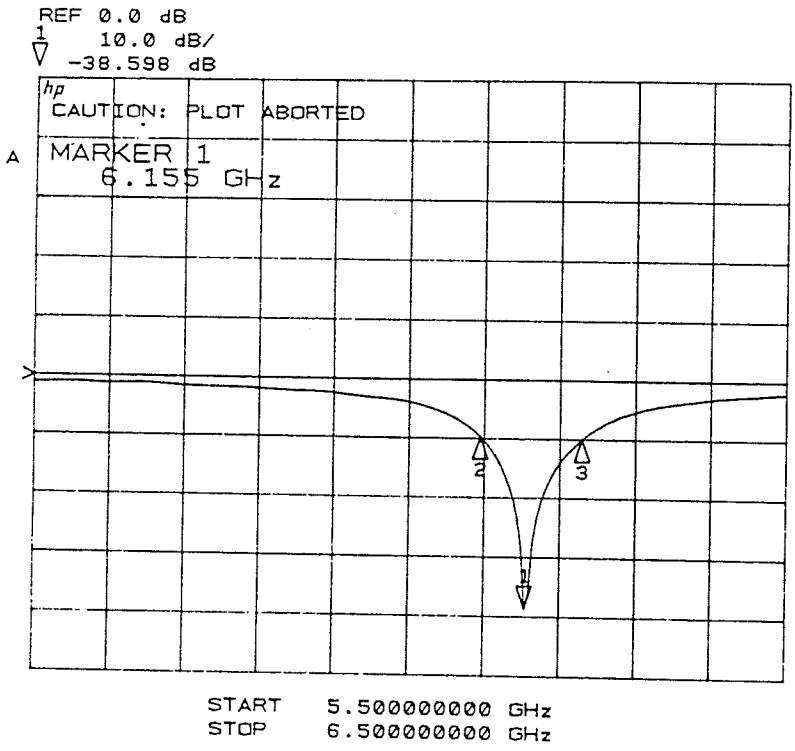

(c) $\alpha = 10^{o}$, $\rho_{feed} = 0.27a$

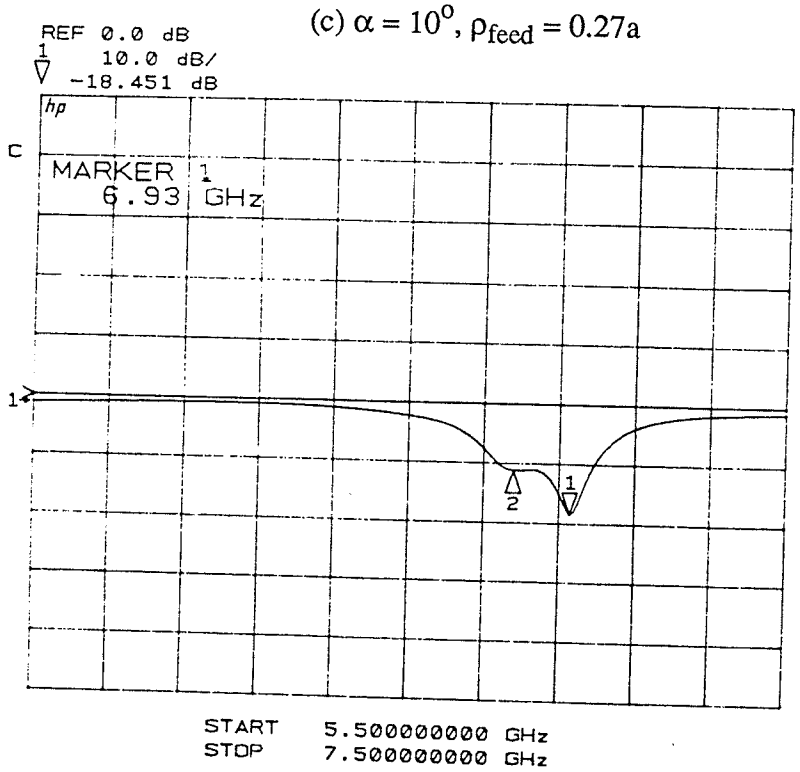

(d) $\alpha = 15^{o}$, $\rho_{feed} = 0.23a$

Fig. 5.2 (cont.)

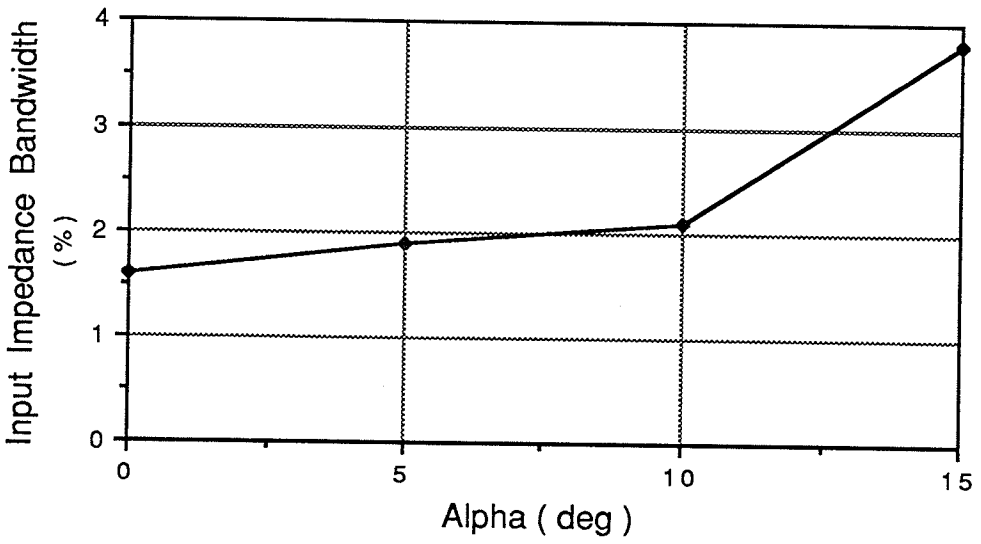

(a)

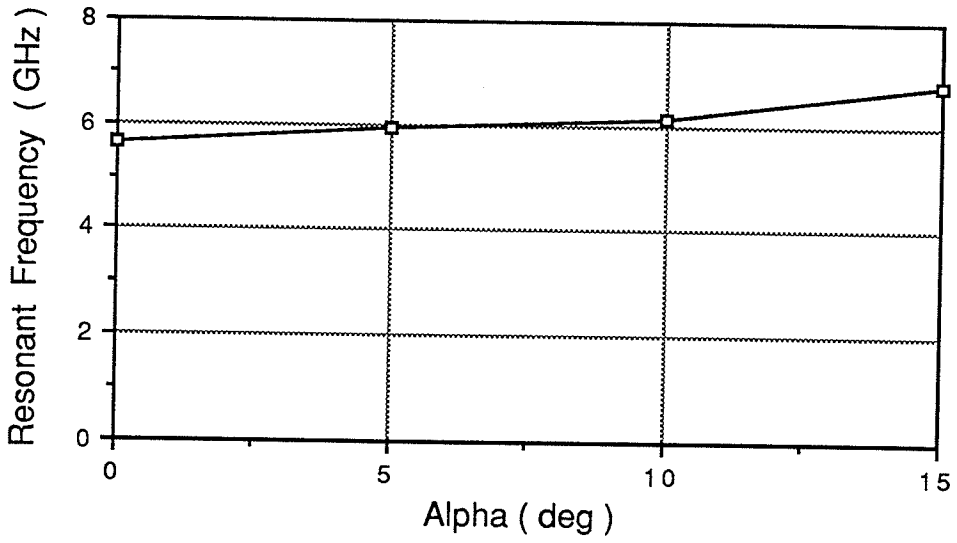

(b)

Fig. 5.3 : Variations of input impedance bandwidth and resonant frequencies due to angular depression

The radiation patterns for each structure were measured and the patterns for $\alpha = 0^o$ and $\alpha = 15^o$ are given in figure 5.4 (a) and (b). All patterns measured showed a ripple in the main beam of the E-plane. This ripple increased in magnitude as the angle of depression increased. Initially, the cause of this was thought to be surface waves. The cutoff frequencies for each surface wave mode may be determined from [26].

$$f_c = \frac{n\,c}{4\,h\,\sqrt{\varepsilon_r - 1}} \qquad (5.3)$$

where $n = 0, 2, 4, \ldots$ for TM modes

$n = 1, 3, 5, \ldots$ for TE modes

It can be seen that the lowest order TM mode, n = 0, exists for all frequencies. Hence that mode of the surface wave will exist in all substrates. The next mode is the TE_1 mode which has a cutoff frequency for this particular application of

$$f_c = \frac{n\,c}{4\,h\,\sqrt{\varepsilon_r - 1}}$$

where $n = 1$

$c = 3\text{x}10^8$ m/s

$h = 1.27\text{x}10^{-3}$ m

$\varepsilon_r = 10$

$$\therefore\ f_c = 19.69 \text{ GHz}$$

Thus only the TM_0 mode of the surface wave exists for these antennas. Equation (5.3) shows that as height and/or relative permittivity increases, more surface wave modes can exist. The effects of surface waves on thin substrates have been studied in [26]. It was determined that for substrates less than .01λ thick, surface wave excitation is trivial and hence may be ignored. This translates to substrate thickness less than 0.5 mm for a frequency of 6 GHz. The substrate thickness used is 1.27 mm, thus the surface waves

cannot be completely ignored. Examining the radiation pattern shows that there are no unusual sidelobes at the edges ($\pm 90^{o}$). If a significant level of surface waves were present, these sidelobes would appear. In addition, the patch was also fabricated on a stycast substrate of thickness 0.64 mm which approaches the trivial case for surface wave excitation. The measured patterns exhibited a ripple equal in magnitude to the case with h = 1.27 mm. Thus it may be concluded that surface waves are not the cause of this ripple.

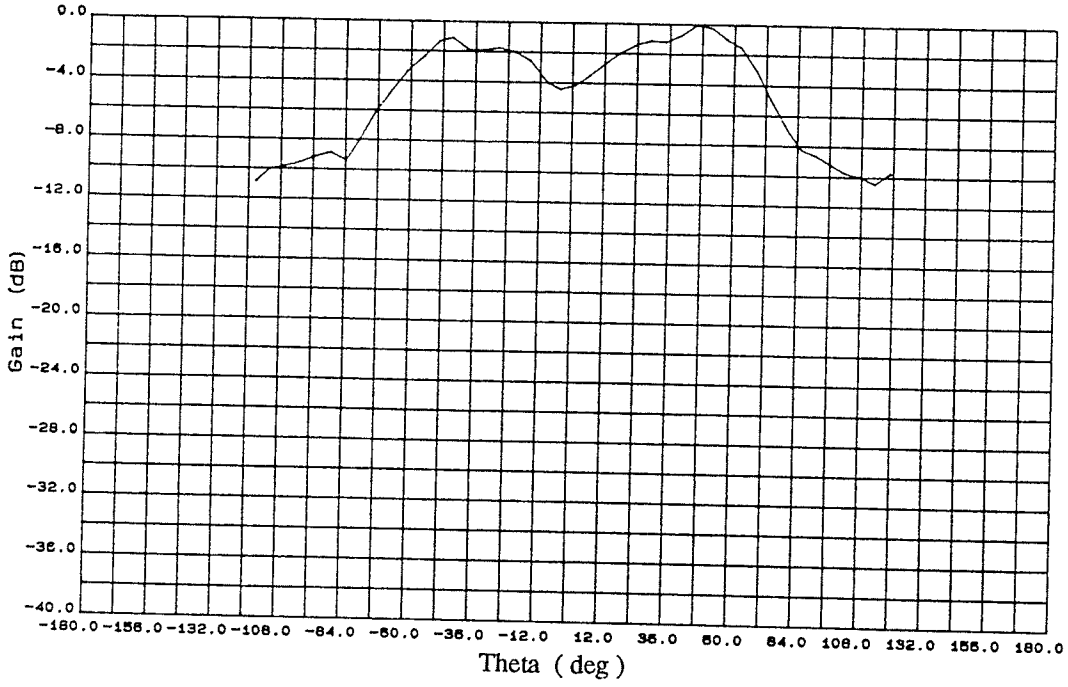

(i) E-plane, f = 5.5 GHz, Gp = 2.15 dB

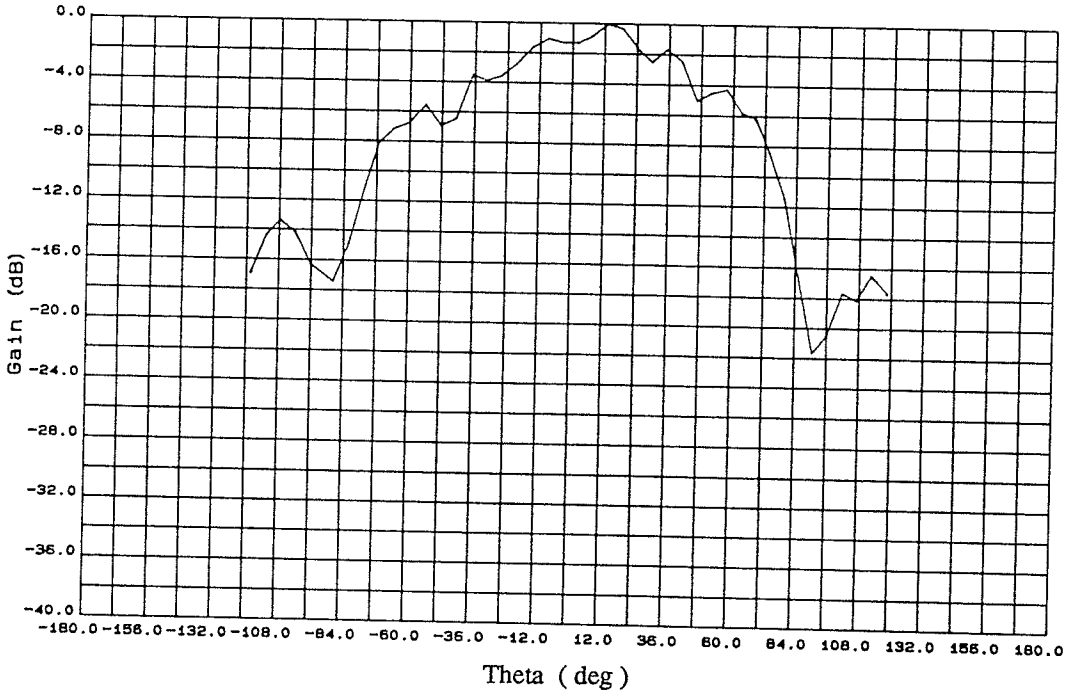

(ii) H-plane, f = 5.5 GHz, Gp = 0.63 dB

Fig. 5.4 a) : Pattern measurements of conically depressed circular patch, $\alpha = 0^{o}$

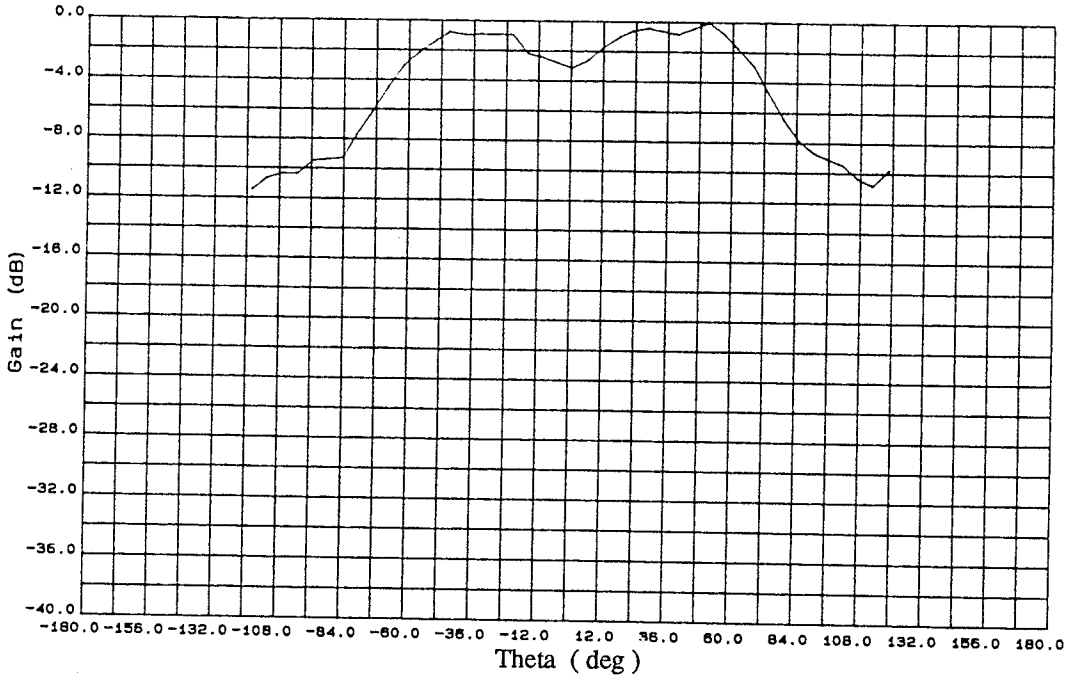

(iii) E-plane, f = 5.6 GHz, Gp = 4.54 dB

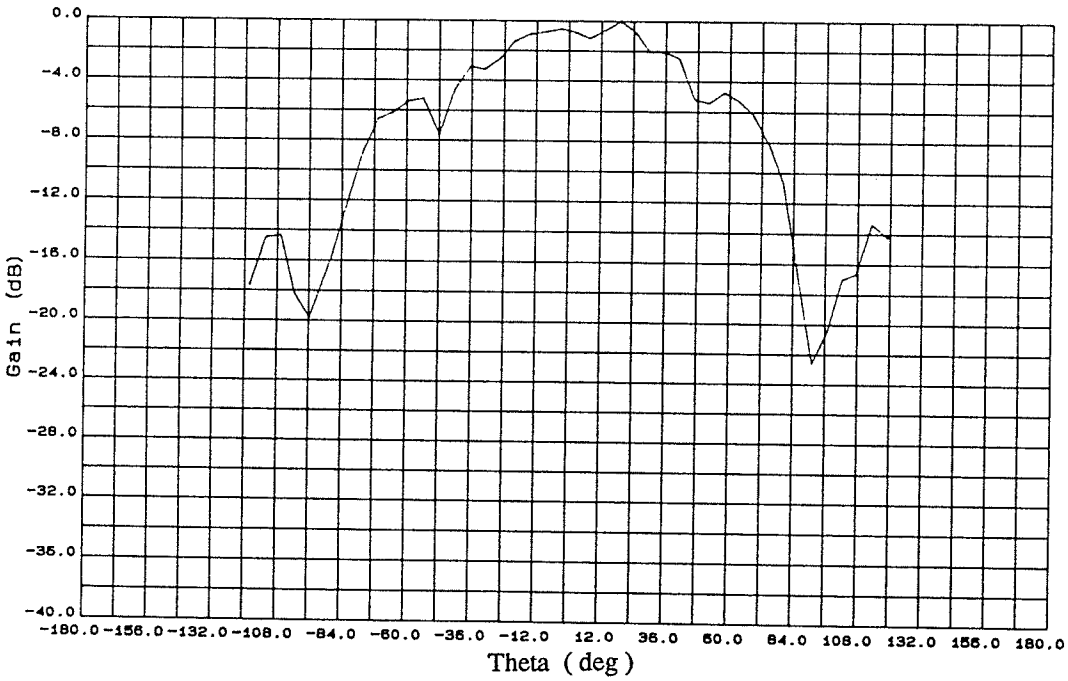

(iv) H-plane, f = 5.6 GHz, Gp = 2.28 dB

Fig. 5.4 (cont.)

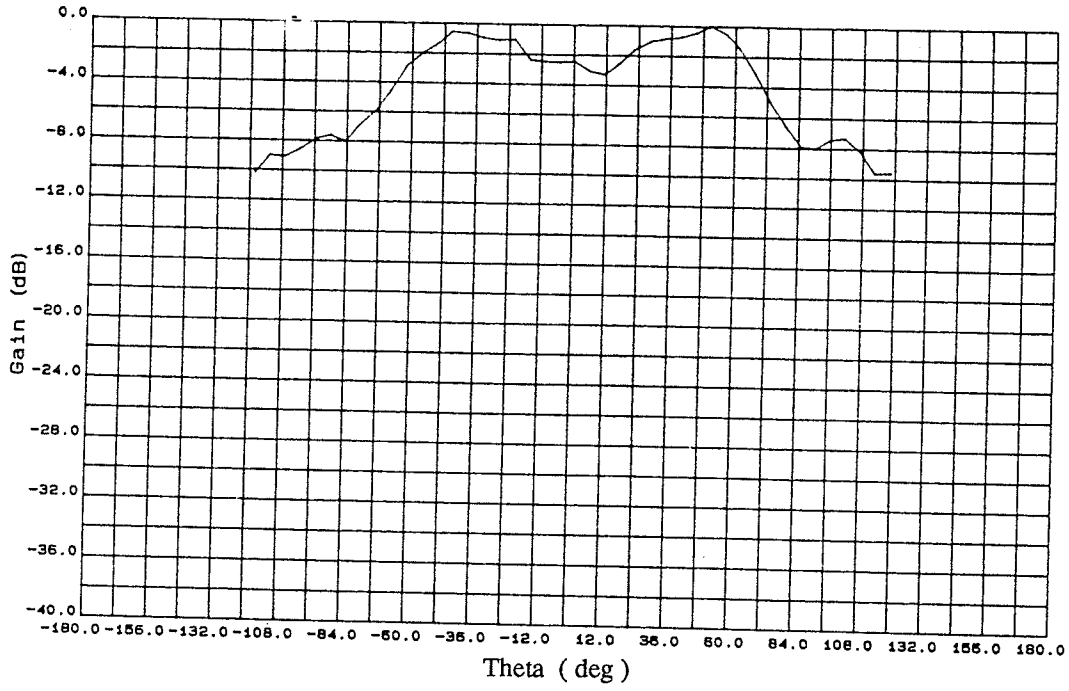

(v) E-plane, f = f_o = 5.65 GHz, Gp = 4.39 dB

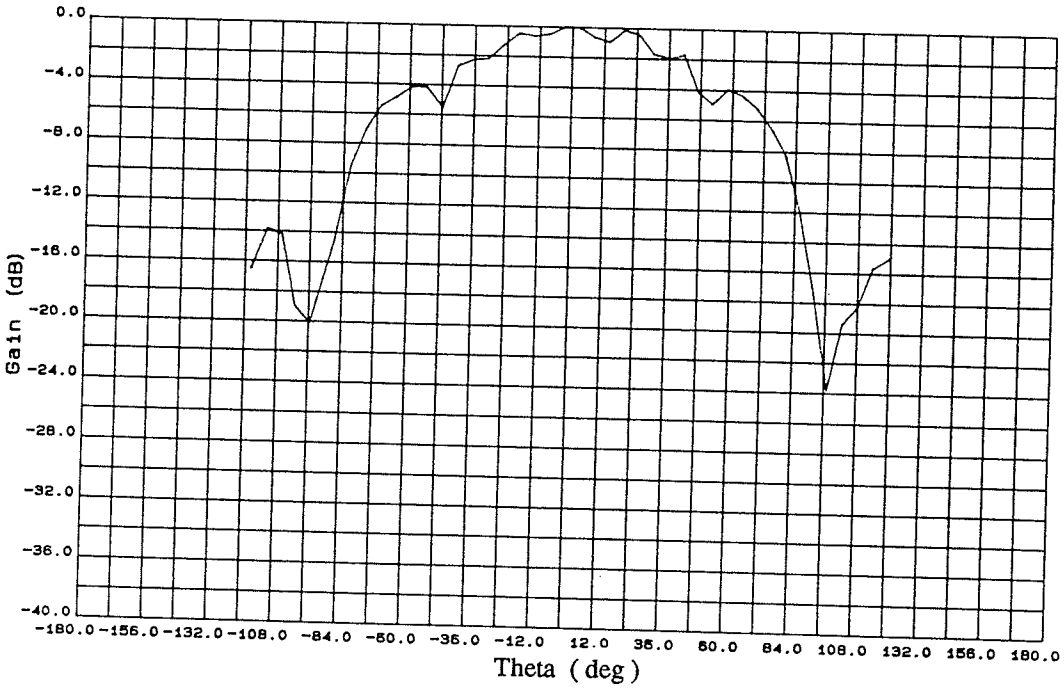

(vi) H-plane, f = f_o = 5.65 GHz, Gp = 2.52 dB

Fig. 5.4 (cont.)

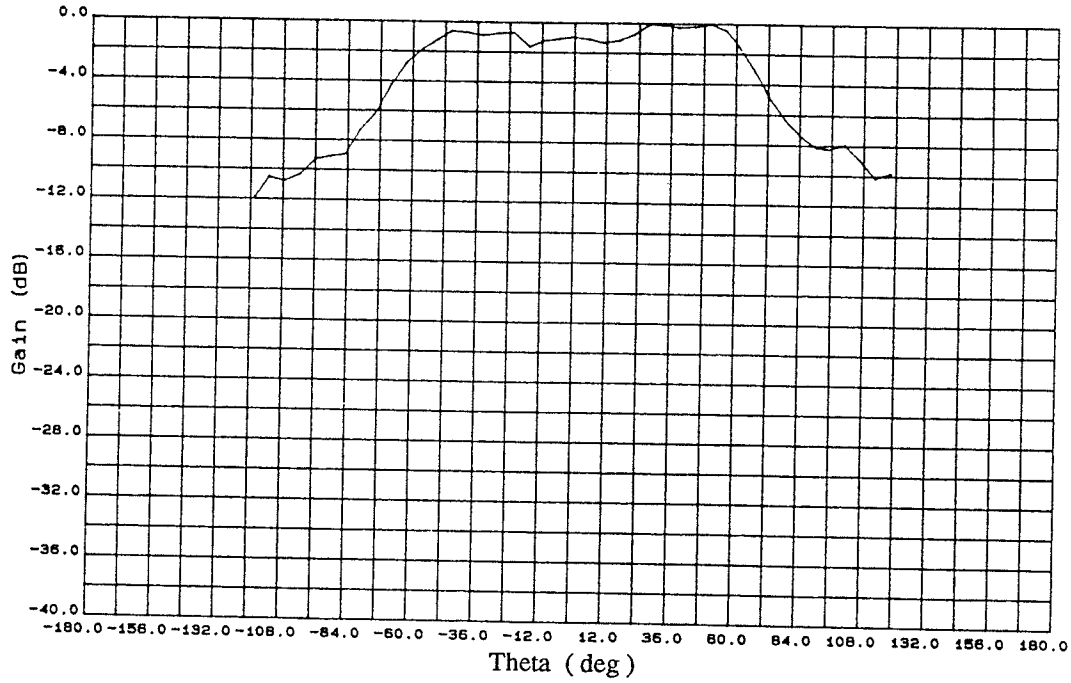

(vii) E-plane, f = 5.7 GHz, Gp = 5.7 dB

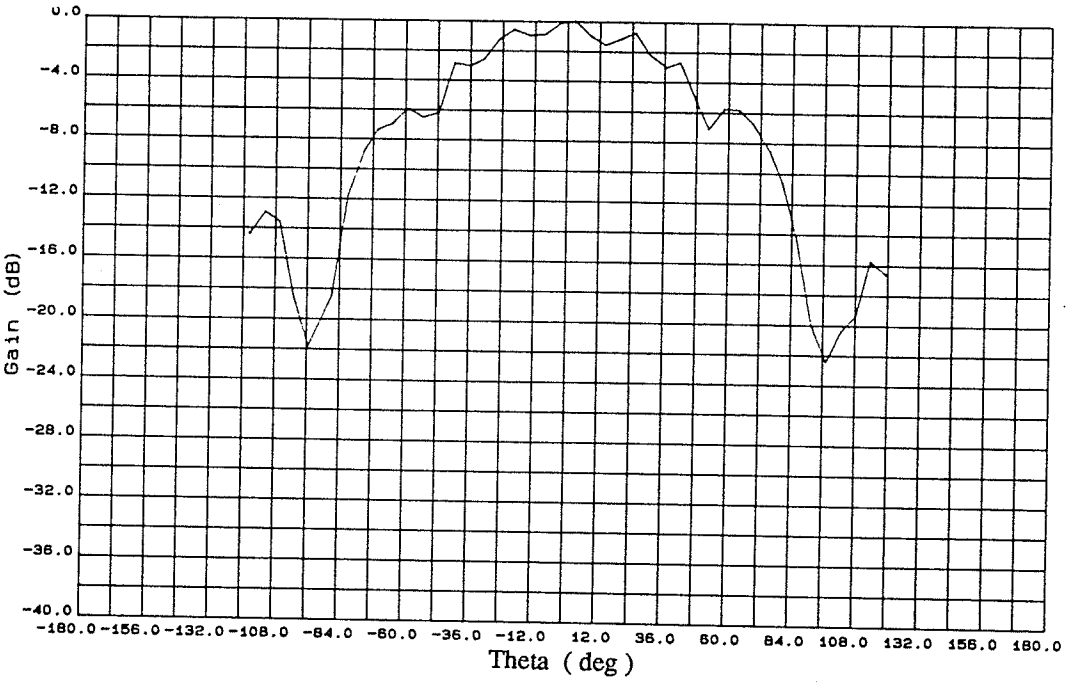

(viii) H-plane, f = 5.7 GHz, Gp = 2.36 dB

Fig. 5.4 (cont.)

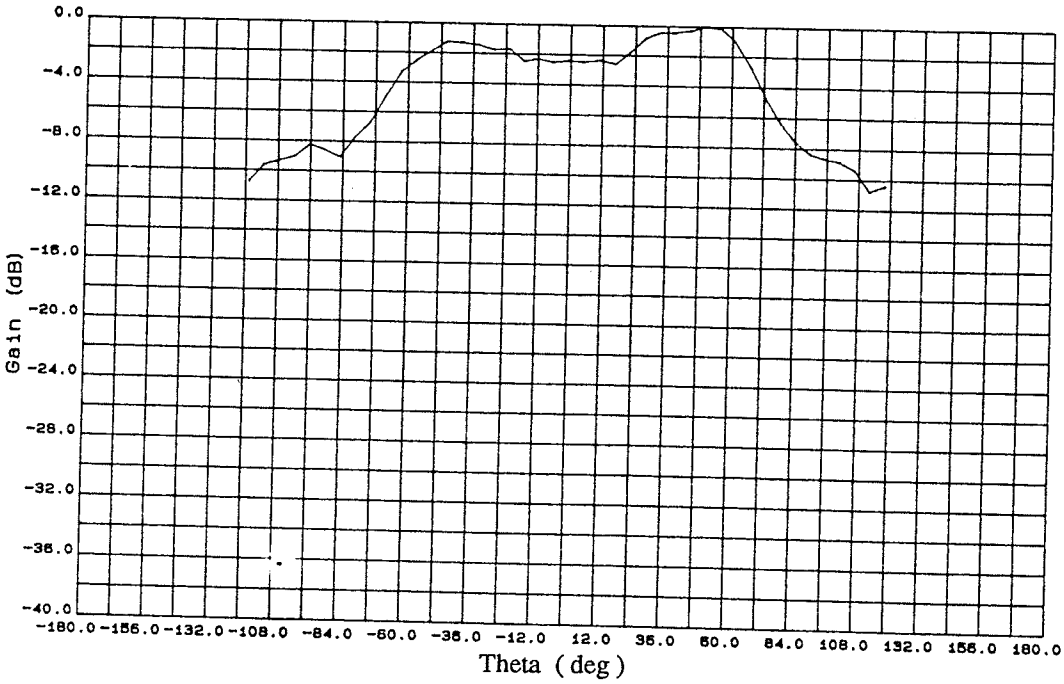

(ix) E-plane, f = 5.75 GHz, Gp = 3.14 dB

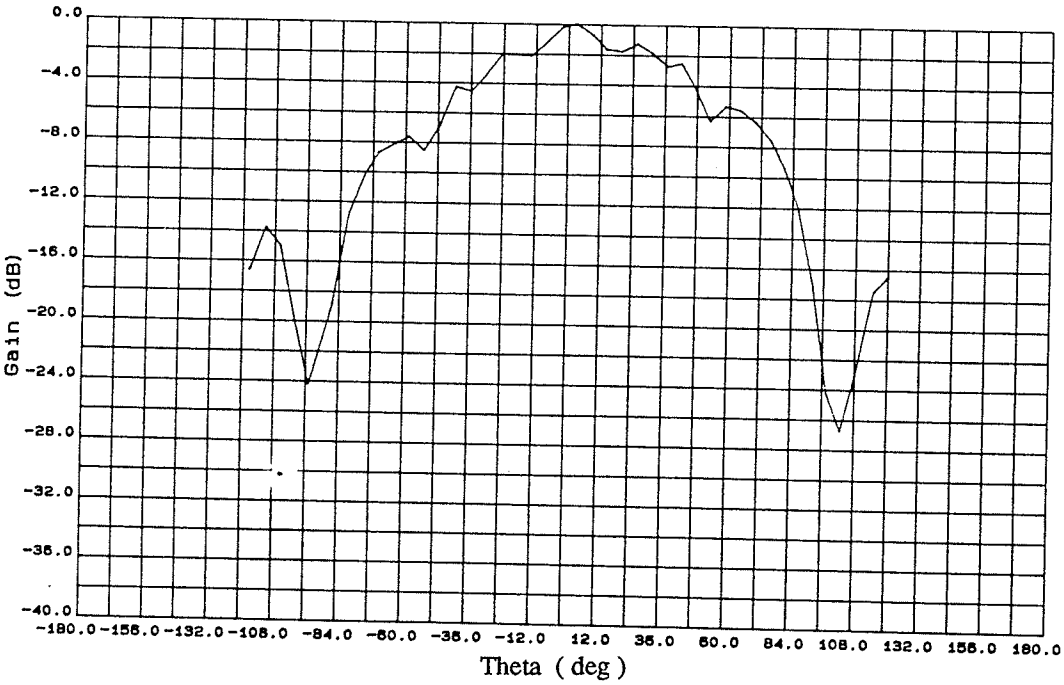

(x) H-plane, f = 5.75 GHz, Gp = 1.81 dB

Fig. 5.4 (cont.)

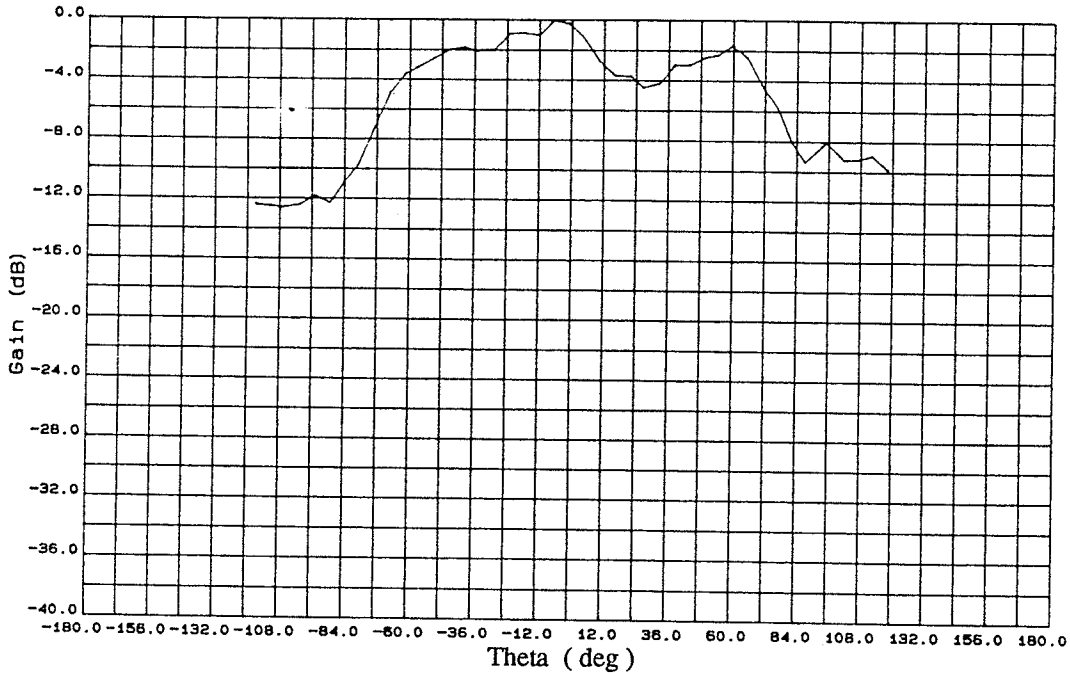

(i) E-plane, f = 6.78 GHz, Gp = 1.22 dB

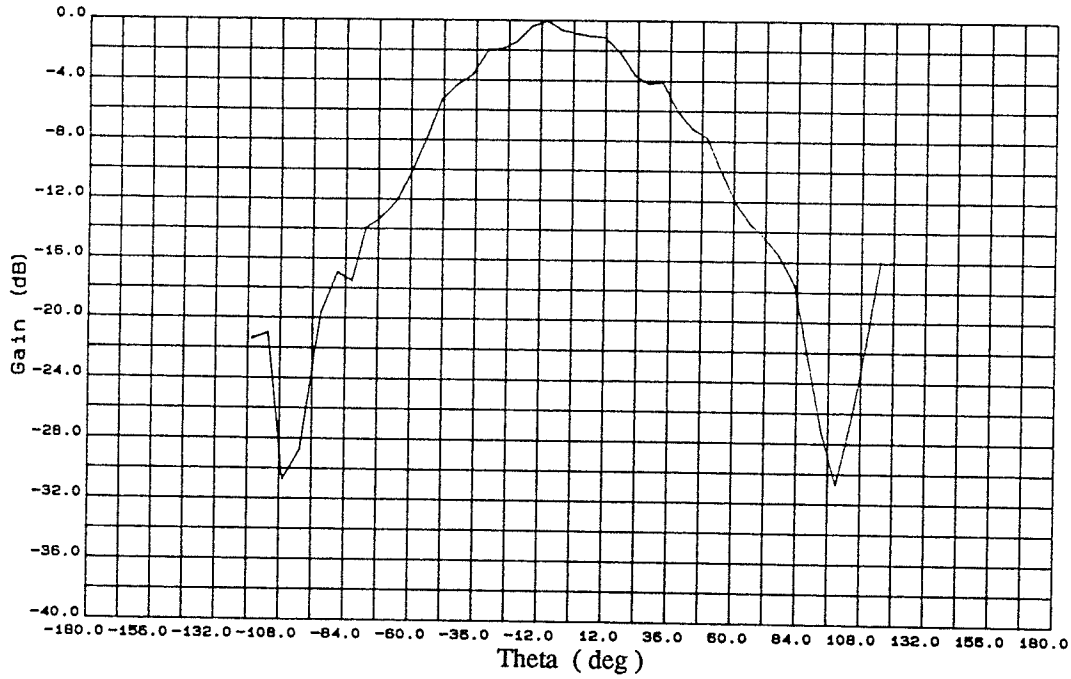

(ii) H-plane, f = 6.78, Gp = 1.37 dB

Fig. 5.4 b) : Pattern measurements of conically depressed circular patch, $\alpha = 15^{o}$

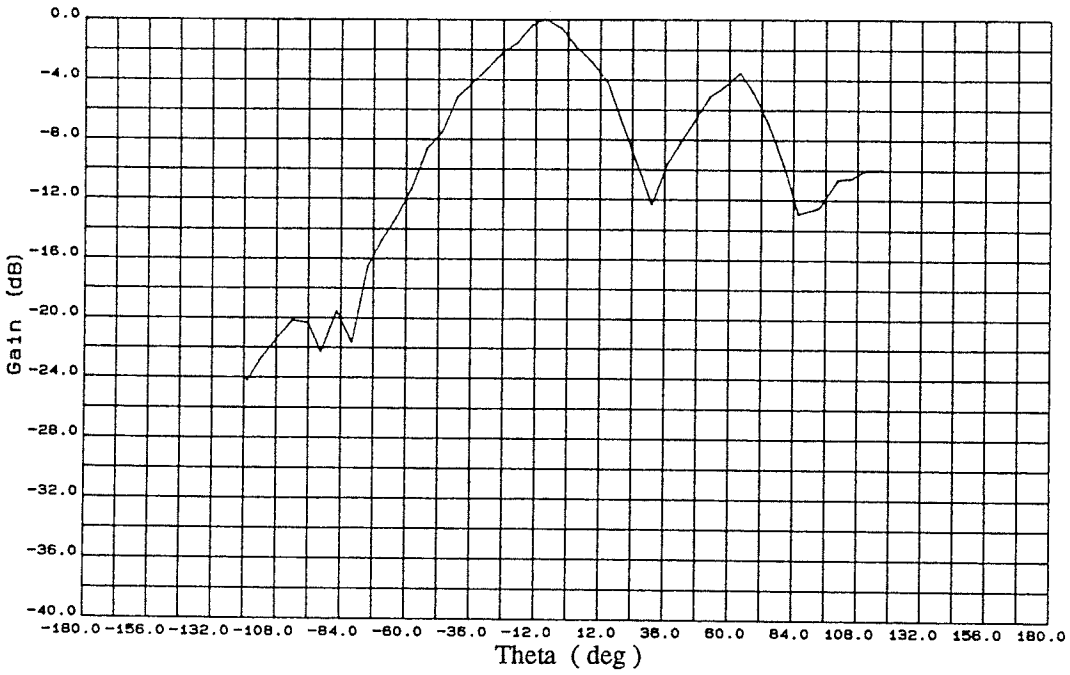

(iii) E-plane, f = 6.93 GHz, Gp = -0.34 dB

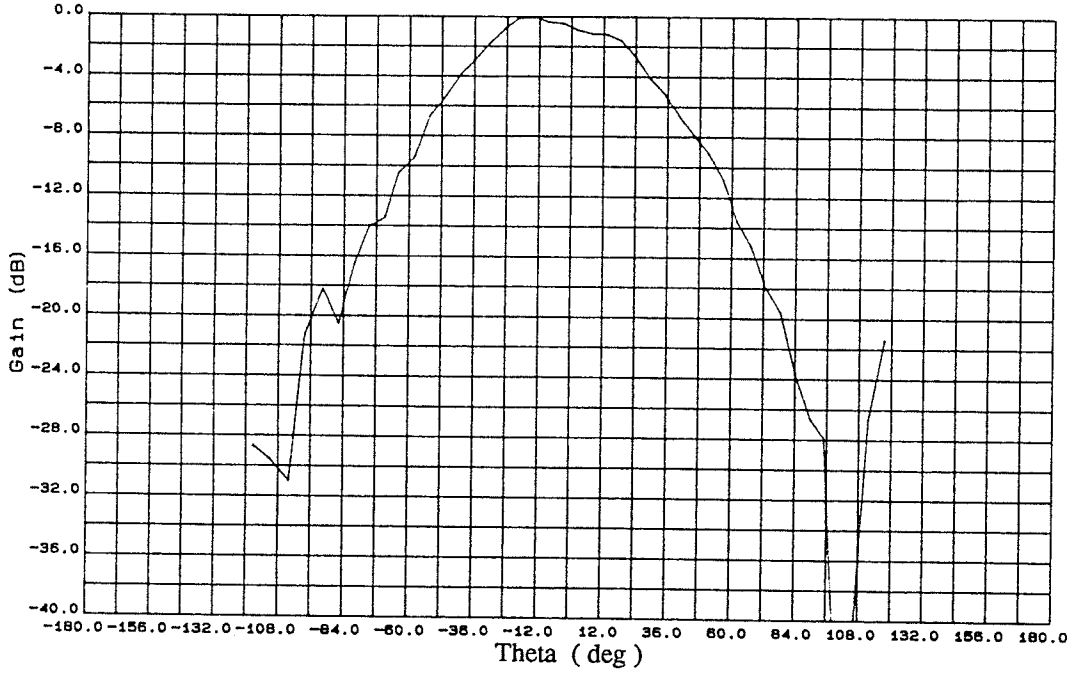

(iv) H-plane, f = 6.93 GHz, Gp = -1.18

Fig. 5.4 (cont.)

Figure 5.4 shows that the magnitude of the ripple increased as the angle of depression increased. Figure 5.2 shows the return loss measurements and for $\alpha = 15^{o}$, another mode is clearly present. The two modes have resonant frequencies at 6.74 GHz and 6.91 GHz at which pattern measurements were taken and are given in figure 5.4 (b). The higher ordered modes after the TM_{11} mode for a circular patch are the TM_{21} and TM_{02} modes which both have a null in the centre of its radiation pattern. A circular patch operating in the TM_{02} mode has a uniform electric field along its circumference as indicated in [31]. Applying a capacitive load to the patch as was done in [45] with an annular ring should indicate if this is one of the two modes present. A capacitive load located at an angle of 90^{o} from the feed point should not effect the TM_{11} or TM_{21} mode as the electric fields are zero at this point. However, this load should lower the resonant frequency of the TM_{02} mode because an electric field is present. A capacitive load was added , and no change was observed with respect to the two resonating frequencies. Thus it is clear that the TM_{02} mode is not present. The pattern measurement at f = 6.78 GHz shows a broadside pattern while the measurement at f = 6.93 GHz shows a definite null in the pattern. Thus it may be concluded that the pattern measurement at f = 6.93 GHz is actually the second order TM_{21} mode in combination with the TM_{11} mode, and vice versa for the pattern measurement at f = 6.78 GHz. Therefore it may be said that as the angle of depression increases, the TM_{21} mode excitation increases and interferes with the desired TM_{11} mode. Information regarding the gain, 3 dB beamwidths and the data previously discussed is presented in Table 5.1.

θ (deg)	$BW_{Z_{in}}$ (%)	3dB Beamwidth (deg)		Gain (dBi)	f_r (GHz)
		E-plane	H-plane		
0	1.6	130	88	4.4	5.65
5	1.9	128	78	2.9	5.94
10	2.1	120	66	2.4	6.16
15	3.8	122	58	1.5	6.78

Table 5.1 : Characteristics of conically depressed circular patches

A change in the 3 dB beamwidth is evident in the H-plane as the beamwidth has decreased by 30^o as α varies from 0^o to 15^o. In addition, there is a decrease in gain. The maximum gain can be determined from equation (4.10) as shown below.

$$G_{max} = \frac{4\pi A_e}{\lambda^2}$$

where Ae is the effective area

$$\lambda = \lambda_{eff} = \frac{\lambda_o}{\sqrt{\varepsilon_{eff}}}, \quad \varepsilon_{eff} = 8.29$$

$$\therefore \; G_{max} = 4.74 \text{ dB}$$

The gain at $\alpha = 0^o$ is close to the maximum calculated gain, thus high efficiency may be deduced. The measured gain is seen to decrease as the angle of depression increases. This is due to the destructive interference of the TM_{21} mode.

The radiation patterns shown in figure 5.4 show a relatively constant pattern shape over the impedance bandwidth, thus the operational bandwidth is limited by BWzin. This is also the case for $\alpha = 5^o$ and 10^o. However, $\alpha = 15^o$ shows a large pattern difference at

f = 6.93 GHz which is within the BW_{Zin}. Thus the operational bandwidth is limited by the pattern bandwidth, hence BW_{op} = 2 % for this particular case.

This type of structure does show an increase in impedance bandwidth with high radiation efficiency. However, fabrication would be quite complex for the mass production process required with MMICs. An alternate structure, similar to this one but easier to fabricate, is the concentrically shorted patch.

5.2 : Concentrically Shorted Circular Microstrip Patch Antenna

A concentrically shorted circular patch as shown in figure 5.5 has been proposed in [44]. This structure was briefly studied as it is similar to the conically depressed patch. It has been determined that as the radius of the shorting rod increases, the bandwidth and resonating frequency increase while high radiation efficiency is maintained. As with the depressed patch, the bandwidth increases due to an increase in the radiation loss, thus lowering Q_T. The increased radiation comes from the contributions of the electric currents on the inner conductor (shorting rod) [44]. The bandwidth and resonating characteristics were verified experimentally. A circular patch with radius of b = 1.634 cm was fabricated on a substrate with ε_r = 2.52 and h = 1.6 mm, ρ_{feed} = b. Starting from the centre and moving outwards, a ring of shorting posts, with radius a, was added to the patch. As each ring was added, the return loss was measured and shown in figure 5.6.

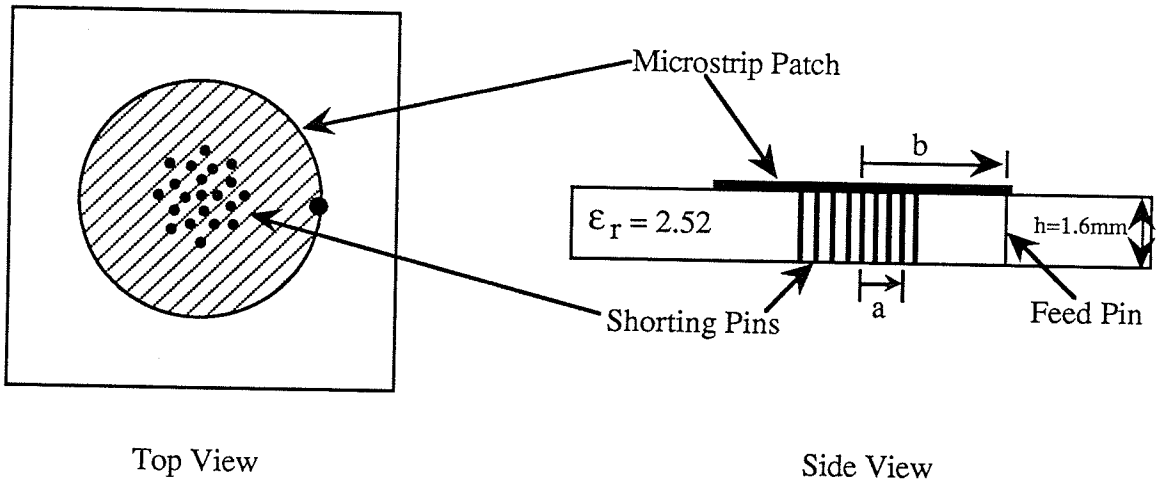

Fig. 5.5 : Concentrically shorted circular patch.

It may be seen that the presence of a shorting rod and a feed point along the circumference excites other modes other than the TM_{11} mode, thus the problem of mode interference may also exist with this structure. The resonant frequencies and bandwidths were obtained from these data and plotted in figures 5.7 (a) and (b). These figures show a comparison between the analytical results in [44] and those experimentally measured. Good agreement is found with respect to the resonant frequencies, and the experimental bandwidth appears larger than the analytical. The measured bandwidth has increased by a factor of 1.6. If this structure were applied to a substrate with a high relative permittivity, lower bandwidths would be observed but an increase would still be noted for structures with larger shorting rods. This structure also appears difficult to fabricate for MMIC / MHMIC applications but probably is easier to fabricate than the conically depressed patch.

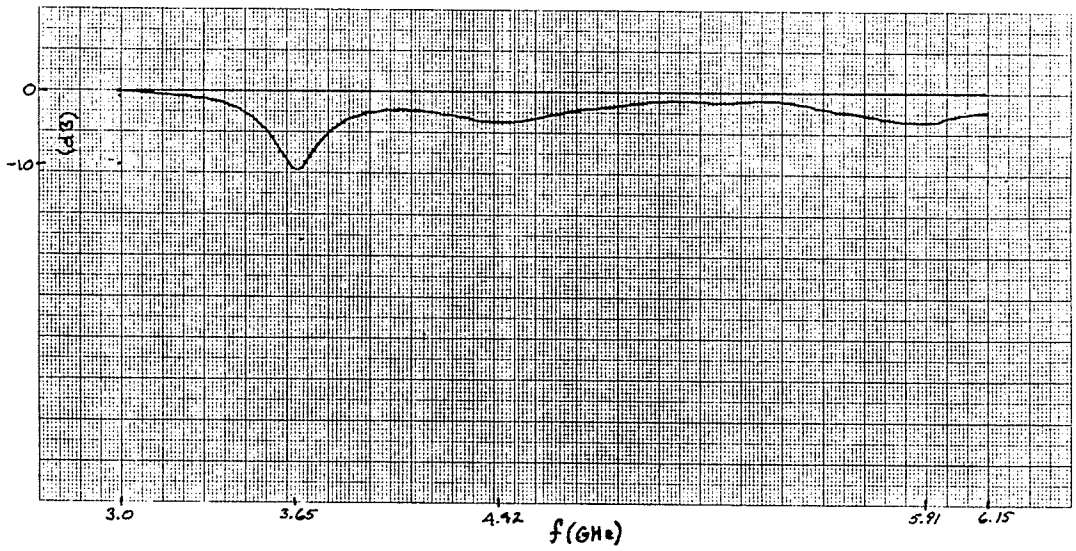

(a) a/b = 0.45

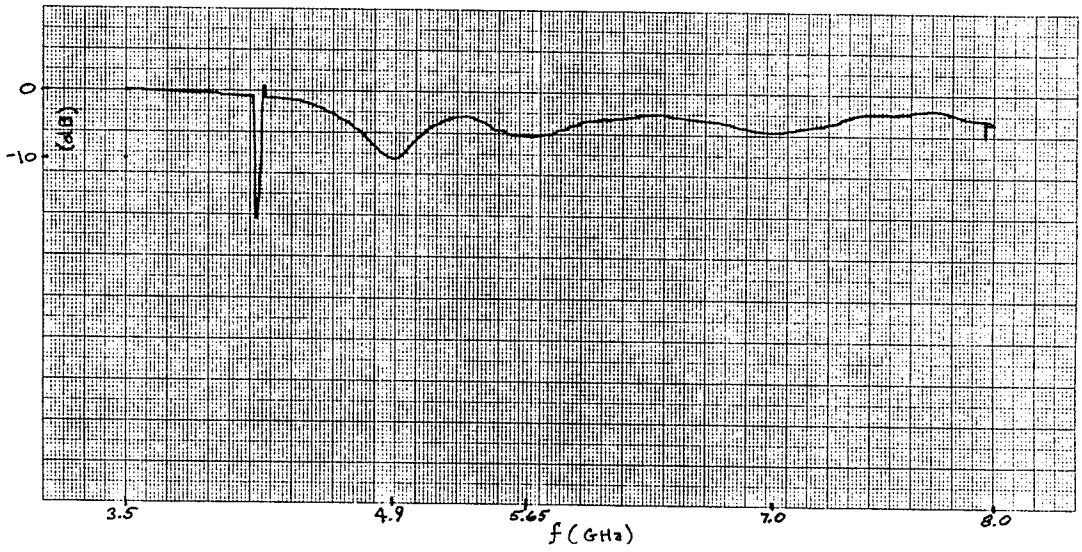

(b) a/b = 0.6

Fig. 5.6 : Return loss measurements for concentrically shorted patches

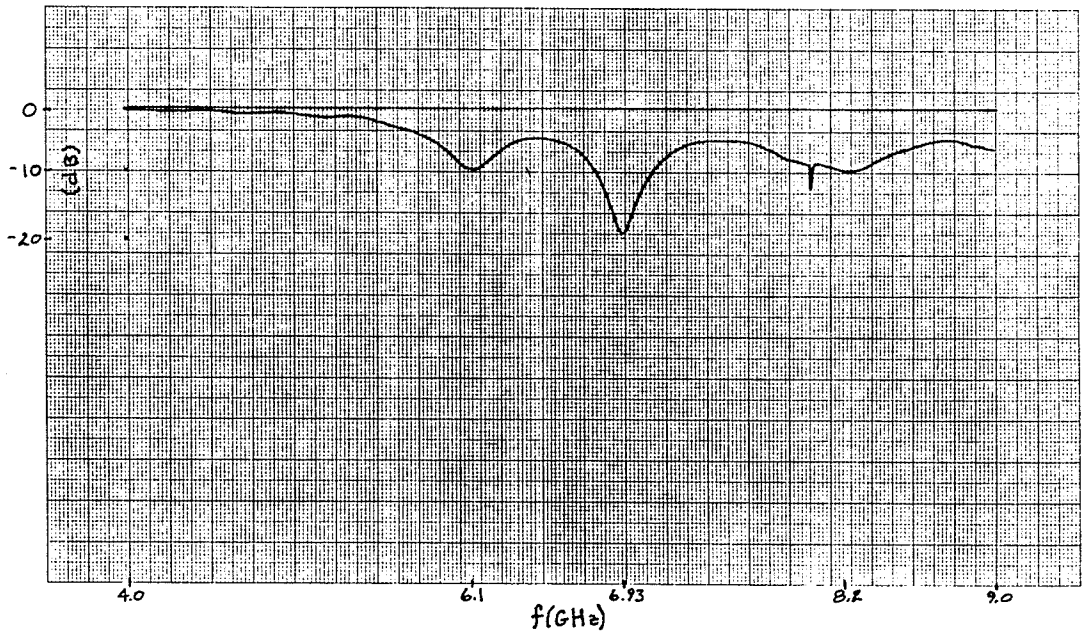

(c) a/b = 0.69

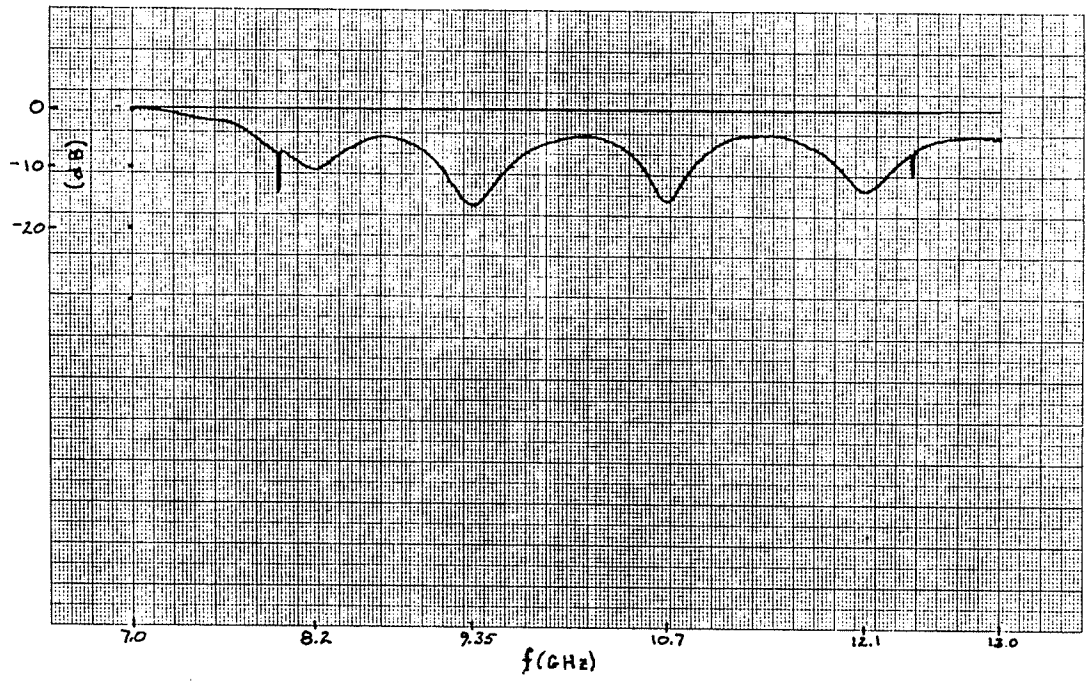

(d) a/b = 0.75

Fig. 5.6 (cont.)

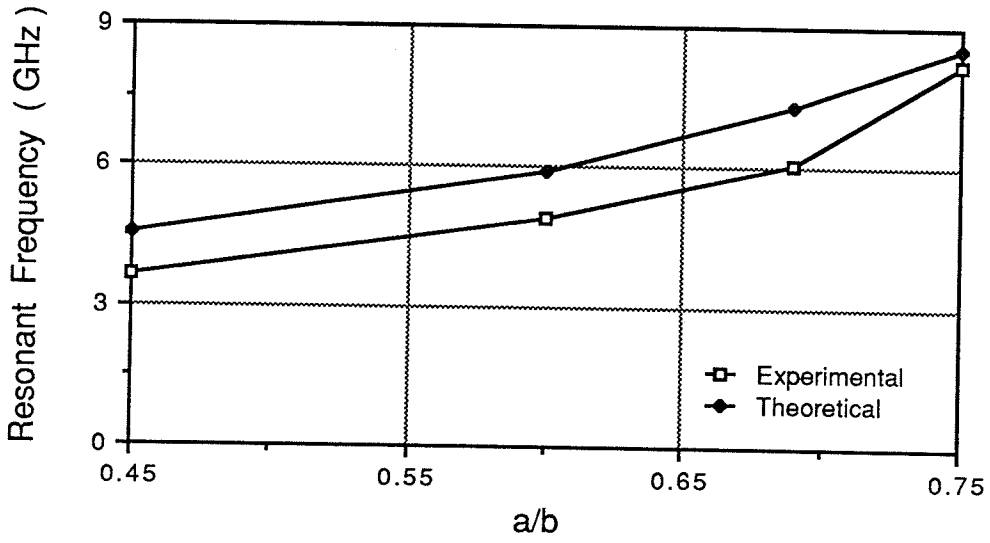

(a) Resonant frequency

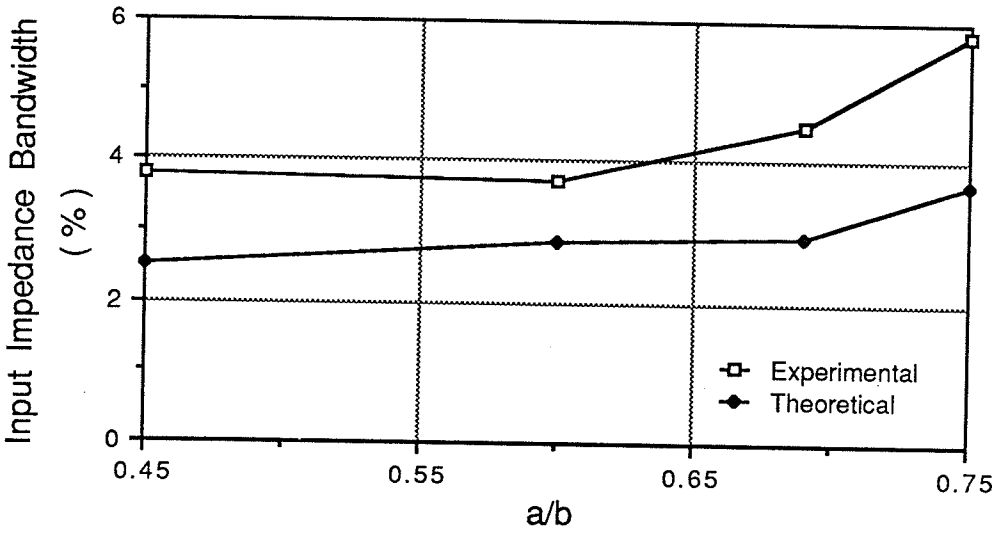

(b) Input impedance bandwidth

Fig. 5.7 : Resonant frequency and bandwidth characteristics.

5.3 Discussion

Two resonating microstrip patch antennas have been studied experimentally. The conically depressed patch shows an increase in the impedance bandwidth as the angle of depression increases. However, this also causes interference in the radiated pattern from the TM_{21} mode reducing the pattern bandwidth substantially. To resolve this problem, it could be possible to determine a feed point in which excitation would result in the TM_{11} being dominate and thus minimizing the destructive contribution of the TM_{21} mode. As indicated in figure 5.2 (d), the feed location creates a dominant TM_{21} mode excitation. If this is possible, then the pattern bandwidth may increase to that of the impedance bandwidth, such that an operational bandwidth of 3.8 % is obtained for an angular depression of 15^{o}. The concentrically shorted patch also shows an increase in the impedance bandwidth when studied on a lower relative permittivity substrate. It appears higher order mode interference could be a problem, but it is not clear as to what will happen when it is placed on a high dielectric substrate.

These structures appear to have a high radiation efficiency with an improved bandwidth. The construction of both antennas would be difficult when applying to an MMIC fabrication process. However, the concentrically shorted patch can be implemented into this process more easily than a conically depressed patch. Thus, these resonating microstrip patches could be used for MMIC / MHMIC applications provided the difficulties in manufacturing are not an overwhelming factor.

CHAPTER 6 : Conclusions and Recommendations

6.1 : Conclusions

The concept of applying MMIC / MHMICs to a phased array antenna presents a number of problems which must be overcome. One problem, which has been addressed in this thesis, is the selection of a suitable radiating element. For a truly monolithic, conformal configuration, the antenna elements should be capable of being constructed within the MMIC batch fabrication process. This means that the ideal antenna element would be deposited on a thin, high relative permittivity substrate which is used in MMIC / MHMICs. Correspondingly, this results in narrow input impedance bandwidths for microstrip patch antennas. These structures already have inherently small bandwidths which are further decreased when placed on an MMIC / MHMIC type substrate. An example presented was the rectangular patch whose impedance bandwidth decreased from 6.6 % to 1.1 % when the substrate relative permittivity was changed from $\varepsilon_r = 2.32$ to $\varepsilon_r = 9.8$. A review of bandwidth improvement techniques has been presented and the results are summarized in Table 6.1. It is evident that limited work has been done on developing radiating elements suitable for high dielectric substrates. The present solution to this problem is to use a multi-layered structure, one layer for circuitry and another layer with low ε_r for the antenna elements.

A traveling wave antenna was studied as a solution to the problem of small impedance bandwidths associated with antenna elements on a thin, high relative permittivity substrate. The structure is a microstrip line with a geometrical orientation such that circular polarization is obtained when terminated with a matched load. The analysis of this antenna showed a fairly large input impedance bandwidth, but a limitation due to the pattern bandwidth. It was also observed that the main beam squinted $\pm 30^{o}$ within this bandwidth.

In addition, short and open circuit termination create a standing wave which produces a broadside , linear polarized pattern. Thus this structure becomes quite versatile since both polarization conditions can be obtained by simply changing the terminating load condition. This structure was fabricated on an alumina substrate and all the above characteristics were observed. The operating bandwidth was limited to the pattern bandwidth of 15 % for the case of circular polarization. Unfortunately, the radiation efficiency of this structure on alumina is quite low and was determined to be 4.1 %. Some modifications to the structure were studied in order to increase the efficiency. An increase to 30 % was obtained, however the gain remained quite low since the radiated energy was adding destructively. Thus, while the studied modifications may not be ideal, it has been shown nevertheless that improvement to the radiation efficiency is possible.

A circularly polarized broadside pattern with an operating bandwidth of 15 % has been produced with a single feed point. For phased array applications, it is conceivable that the squinting within the bandwidth can be eliminated by selective orientation of each element within the array. In addition, this structure provides a location for the circuitry within its perimeter. Therefore this traveling wave antenna may be considered as a suitable element in application to MMIC / MHMICs provided radiation efficiency can be improved upon.

Conically depressed and concentrically shorted circular microstrip patches were also studied experimentally. The conically depressed patch was fabricated on Stycast material with $\varepsilon_r = 10$. It was observed that as the angle of depression increased, the resonant frequency and bandwidth also increased with a high radiation efficiency. The maximum angular depression fabricated was 15^o where an impedance bandwidth of 3.8 % was measured. This is an improvement over the 1.6 % impedance bandwidth for a flat circular

disk. It was also observed that the TM_{21} mode was dominantly excited for this case, and hence the pattern did not remain constant within this bandwidth. Although this mode cannot be completely eliminated, a feed location could be selected such that the TM_{11} mode would be dominantly excited. Hence the radiated pattern would be predominantly TM_{11} with a contribution from the TM_{21} mode as is the case for $\alpha = 0^o, 5^o$, and 10^o.

This structure provides an operating bandwidth of 3.8 % with a high radiation efficiency. However, the fabrication of this antenna would be difficult. Therefore this antenna may be considered as a possible compatible element for MMIC / MHMICs provided the bandwidth is acceptable and the fabrication problems can be overcome. Comparing the conically depressed patch with the traveling wave antenna shows the advantages and disadvantages for one structure are the opposite for the other.

A variation of the conically depressed patch studied was the concentrically shorted patch. This structure was fabricated on a substrate with $\varepsilon_r = 2.32$. An increase in resonant frequency and impedance bandwidth was observed as the shorting rod increased. It is not clear how this structure will perform on a high dielectric substrate, however it would be easier to fabricate then the conically depressed patch.

The circular microstrip patches and the traveling wave antennas studied have also been included in the summary table 6.1 given.

Structure Type	Characteristics of Radiating Element Substrate	Operating Bandwidth	Comments
Rectangular Patch	$\varepsilon_r = 2.32$, $h = 1.59$ mm $f_o = 10$ GHz	6.6 %	- suitable for a one batch process
* Rectangular Patch	$\varepsilon_r = 12.8$, $h = 0.5$ mm $f_o = 10$ GHz	1.7 %	- suitable for a one batch process
* Mesh Rect. Patch	$\varepsilon_r = 12.8$, $h = 0.5$ mm $f_o = 13.5$ GHz	2.1 %	- mesh constructed from air bridges - fabrication requires more time than planar structure
2-layered Rect. Patch	$\varepsilon_{r2} = 2.32$, $h_2 = 2.34$ mm $f_o = 10.6$ GHz	13 %	- circuitry placed on lower layer with $\varepsilon_r = 9.8$ - cannot be fabricated in a one batch process
3-layered Rect. Patch	$\varepsilon_{r3} = 2.32$, $h_3 = 2.34$ mm $f_o = 10.6$ GHz	18 %	- same as 2-layered structure - height has further increased thus reducing conformal properties
2 Rectangular Stacked Patches	$\varepsilon_{r2} = 2.2$, $h_2 = 2.34$ mm $f_o = 8.56$ GHz	24.9 %	- lower radiator placed on substrate with er=10 - cannot be fabricated in a one batch process
5 Rect. Patches Parasitically Coupled	$\varepsilon_r = 2.55$, $h = 3.18$ mm $f_o = 3.16$ GHz	25.8 %	- occupies large area in comparison to a single element
Folded Dipole	$\varepsilon_r = 2.55$, $h = 3.2$ mm $f_o = 8.3$ GHz	7.2 %	- suitable for a one batch process - more applicable to brick architecture
Spiral	$\varepsilon_r = 1.0$, $h = 1.25$ cm $f_o = 6$ GHz	16 %	- ground plane deteriorates axial ratio - radiation efficiency improves by increasing arm lengths
* 4-arm Traveling Wave	$\varepsilon_r = 9.8$, $h = 0.635$ mm $f_o = 3$ GHz	15 %	- circular polarization achieved with one feed - fabrication is simple and applicable to a one batch process - very low efficiency
* 15^o Depressed Conical Patch	$\varepsilon_r = 10.0$, $h = 1.27$ mm $f_o = 6.78$ GHz	3.8 %	- multi-mode excitation resulting in a 3 dB - fabrication is difficult
Concentrically Shorted Circ. Patch	$\varepsilon_r = 2.32$, $h = 1.6$ mm $f_o = 7.8$ GHz	5.8 %	- fabrication is difficult

* indicates structures having radiating elements on substrates with high relative permittivities

Table 6.1 : Summary of antenna structures

6.2 : Recommendations

Of the studied structures, the traveling wave microstrip line antenna would be the ideal element if the radiation efficiency can be increased. Thus determining a technique to increase the radiation efficiency is the first recommendation. Two possible methods are to increase the discontinuities along the radiating aperture and to lower the effective permittivity of the substrate under the radiating segments. These two possibilities are shown in figure 6.1.

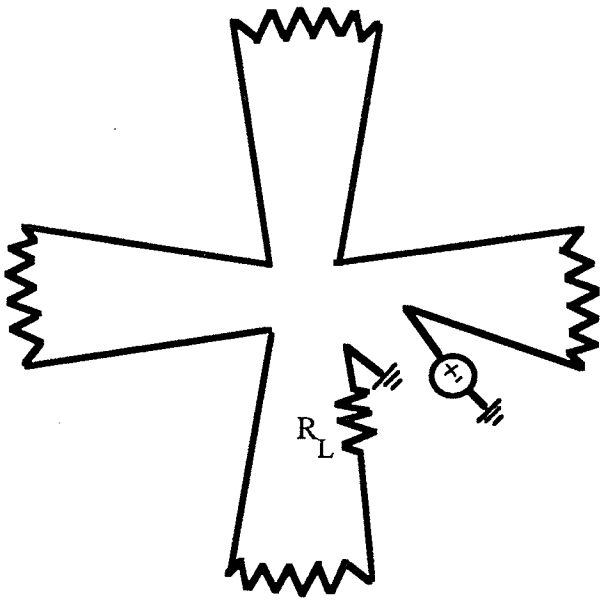

(a)

Fig. 6.1 : Possible schemes for improving radiation efficiency.

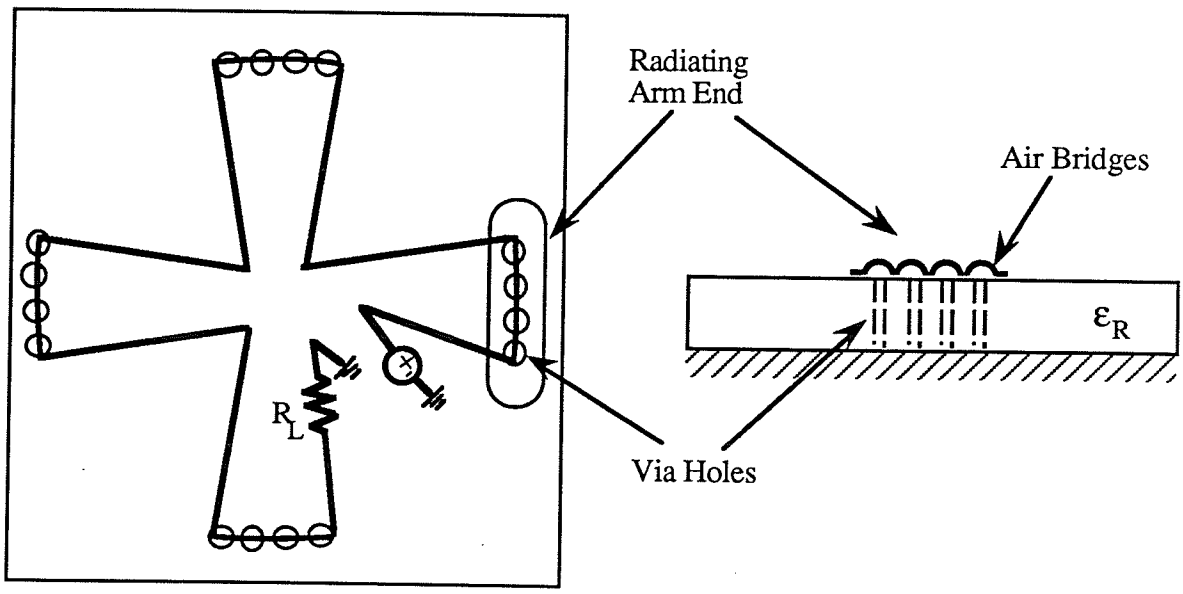

(b)

Fig. 6.1 : Possible schemes for improving radiation efficiency.

The discontinuities in figure 6.1 (a) must be arranged such that the radiated energy will be in-phase thus adding constructively. Figure 6.1 (b) shows that the use of via hole and air bridge technology make it possible to lower ε_{eff} at the radiating segments thus increasing the radiation efficiency.

The study of the concentrically shorted patch on a high relative permittivity substrate is also recommended. This structure would yield a smaller bandwidth than the traveling wave structure. The radiation efficiency would be high however. The fabrication of this structure is more practical then the conically depressed patch. If the fabrication of a conically depressed patch is not deemed to be impractical, then a conically depressed annular ring should be studied. An annular ring operating in the TM_{12} mode would have a higher bandwidth then the circular patch due to the two radiating apertures; hence less stored energy and thus lower Q_T. It should be mentioned that the TM_{12} mode has magnetic

current sources of the same polarity along the inner and outer edges of the ring while the TM_{11} mode has magnetic currents of opposite polarity. Thus the TM_{12} mode has constructive radiation while the TM_{11} mode has destructive radiation, hence it is desirable to operate in the TM_{12} mode.

The final recommendation is to study the parasitic structure on a high dielectric substrate as shown in figure 6.2. This is a rectangular patch composed of coupled microstrip lines of various widths. This structure was studied in [23] and the design was determined experimentally. A solid patch of the same size was fabricated and compared to the parasitic structure. The reported impedance bandwidths were 0.6 % and 6.0 % for the solid and parasitic patches respectively (ε_r = 2.2, h = 0.8 mm, f = 875 MHz). Thus a parasitic structure equivalent in size to a rectangular patch has shown a substantial improvement in the impedance bandwidth. This alleviates the large real estate occupation problem associated with other parasitic structures.

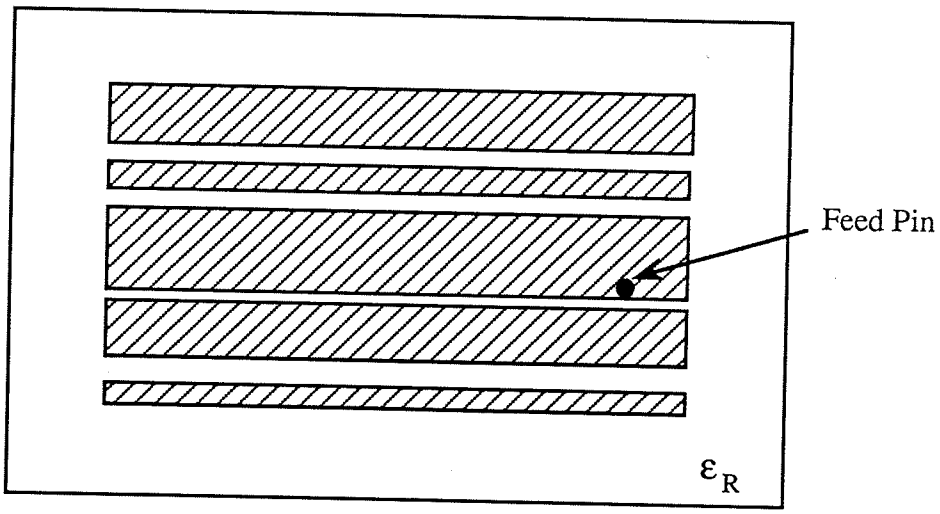

Fig. 6.2 : Parasitic coupled line microstrip antenna.

Appendix A

Polarization

The polarization of an electromagnetic wave is defined in [47] as " that property of a radiated electromagnetic wave describing the time varying direction and relative magnitude of the electric field vector ". This is an important consideration in the design process of an antenna. The desired polarization properties of an antenna are determined by its application.

The electric field at a distant point (far field) comprises two components as shown below

$$E(r,\theta,\phi) = \mathrm{Re}\{ E_\theta \hat{\theta} + E_\phi \hat{\phi} \} \qquad (A.1)$$

where E_θ and E_ϕ are complex

The polarization of the electric field has been well defined in [37] where equation (A.1) was further expanded as follows.

$$\begin{aligned} E_\theta &= [\, a_\theta + j\, b_\theta \,]\, e^{j\omega t} \\ &= a_\theta\, e^{j\omega t} + j\, b_\theta\, e^{j\omega t} \\ &= a_\theta\, (\cos \omega t + j \sin \omega t) + b_\theta\, (\cos(\omega t + \pi/2) + j \sin(\omega t + \pi/2)) \end{aligned}$$

$$\begin{aligned} \mathrm{Re}\{ E_\theta \} &= a_\theta \cos \omega t + b_\theta \cos(\omega t + \pi/2) \\ &= a_\theta \cos \omega t - b_\theta \sin \omega t \end{aligned}$$

Similarly for E_ϕ

$$\mathrm{Re}\{ E_\phi \} = a_\phi \cos \omega t - b_\phi \sin \omega t$$

$$\therefore\ E(r,\theta,\phi,t) = (a_\theta \cos \omega t - b_\theta \sin \omega t)\, \hat{\theta} + (a_\phi \cos \omega t - b_\phi \sin \omega t)\, \hat{\phi}$$

Selecting the origin such that $b_\theta = 0$ yields

$$\therefore\ E(r,\theta,\phi,t) = a_\theta \cos \omega t\, \hat{\theta} + B \cos(\omega t + \beta)\, \hat{\phi} \qquad (A.2)$$

where $B = \sqrt{a_\phi^2 + b_\phi^2}$

$$\beta = \mathrm{Tan}^{-1} \frac{b_\phi}{a_\phi}$$

Equation (A.2) can be used to indicate the various polarizations. If $\beta = 0$, equation (A.2) would reduce to

$$E(r,\theta,\phi,t) = a_\theta \cos \omega t\, \hat{\theta} + B \cos \omega t\, \hat{\phi}$$

The two components will be in-phase resulting in linear polarization. The magnitudes of each component dictate the direction of linear polarization.

If $a_\theta = B$ and $\beta = \pm 90^o$ then equation (A.2) becomes

$$E(r,\theta,\phi,t) = a_\theta (\cos \omega t\, \hat{\theta} \pm \sin \omega t\, \hat{\phi})$$

This results in circular polarization since the magnitude of E is constant and the time varying direction is circular. The direction of circular polarization is either left-handed or right-handed, depending on E_ϕ leading ($\beta = 90^o$) or lagging ($\beta = -90^o$) E_θ respectively. Measurement of this type of wave with a linear source results in only one component being measured at a time. Thus the polarization efficiency will be one half hence it will be necessary to add 3 dB to the measured pattern level.

If $a_\theta \neq B$ and $\beta \neq 0^o$, then the magnitude of E will vary with the two components being out of phase. This results in an elliptical time varying direction known as elliptical polarization.

Appendix B

Derivation of Electric Fields

The far field of a circular loop may be determined from the vector magnetic potential as shown below [31].

$$\overline{E}(r) = -j\omega\overline{A}$$

where $\overline{A}$ is the vector magnetic potential

the far field vector magnetic potential of a circular source is

$$\overline{A} = \frac{\mu}{4\pi}\frac{e^{-jkr}}{r}\int_0^{2\pi}\int_0^{a}\overline{K}(\rho,\phi')\,e^{jk\rho\sin\theta\cos(\phi'-\phi)}\,\rho\,d\rho\,d\phi'$$

where the primed coordinates represent the source

The components of the vector magnetic potential are given in spherical coordinates.

$$A_\theta = \frac{\mu}{4\pi}\frac{e^{-jkr}}{r}a\cos\theta\int_0^{2\pi}\{K_\rho(\rho,\phi')\cos(\phi'-\phi) - K_{\phi'}(\rho,\phi')\sin(\phi'-\phi)\}\,e^{jka\sin\theta\cos(\phi'-\phi)}\,d\phi' \tag{B.1}$$

$$A_\phi = \frac{\mu}{4\pi}\frac{e^{-jkr}}{r}a\int_0^{2\pi}\{K_\rho(\rho,\phi')\sin(\phi'-\phi) + K_{\phi'}(\rho,\phi')\cos(\phi'-\phi)\}\,e^{jka\sin\theta\cos(\phi'-\phi)}\,d\phi' \tag{B.2}$$

The current on the loop is given by

$$I_n = a_n\cos n\phi' + \sin n\phi'\,\hat{\phi}$$

Thus the magnetic potential components reduce to

$$A_\theta = \frac{-\mu}{4\pi}\frac{e^{-jkr}}{r}\,a\cos\theta \int_0^{2\pi} (a_n \cos n\phi' + b_n \sin n\phi')\sin(\phi' - \phi)\, e^{jka\sin\theta\cos(\phi' - \phi)}\, d\phi' \tag{B.3a}$$

$$A_\phi = \frac{\mu}{4\pi}\frac{e^{-jkr}}{r}\,a \int_0^{2\pi} (a_n \cos n\phi' + b_n \sin n\phi')\cos(\phi' - \phi)\, e^{jka\sin\theta\cos(\phi' - \phi)}\, d\phi' \tag{B.3b}$$

Once these components have been determined, the electric field components may be determined by substituting (B.3a) and (B.3b) into equations (B.4a) and (B.4b) given.

$$E_\theta = -j\omega A_\theta \tag{B.4a}$$

$$E_\phi = -j\omega A_\phi \tag{B.4b}$$

Solving for A_θ :

Let $B = \frac{-\mu}{4\pi}\frac{e^{-jkr}}{r}\,a\cos\theta$ and $A = ka\sin\theta$, $\therefore$ equation (B.3a) becomes

$$A_\theta = B\left\{\int_0^{2\pi} a_n \cos n\phi' \sin(\phi' - \phi)\, e^{jA\cos(\phi' - \phi)}\, d\phi' + \int_0^{2\pi} b_n \sin n\phi' \sin(\phi' - \phi)\, e^{jA\cos(\phi' - \phi)}\, d\phi'\right\} \tag{B.5}$$

$$= B\{\boxed{I} + \boxed{II}\} \tag{B.5a}$$

$$\boxed{I} = -\int_0^{2\pi} a_n \cos n\phi' \frac{d}{d\phi'} \cos(\phi'-\phi)\, e^{jA\cos(\phi'-\phi)}\, d\phi'$$

$$= \frac{-1}{jA}\int_0^{2\pi} a_n \cos n\phi' \frac{d}{d\phi'} e^{jA\cos(\phi'-\phi)}\, d\phi'$$

Let $u = \cos n\phi'$ $\qquad dv = \frac{d}{d\phi'} e^{jA\cos(\phi'-\phi)}$

$du = -n \sin n\phi'\, d\phi'$ $\qquad v = e^{jA\cos(\phi'-\phi)}$

$$= \frac{a_n}{jA}\int_0^{2\pi} n \sin n\phi'\, e^{jA\cos(\phi'-\phi)}\, d\phi'$$

Let $\alpha = \phi'-\phi \Rightarrow d\alpha = d\phi'$

$\phi' = \alpha+\phi$

$$\therefore \quad = \frac{a_n}{jA}\int_0^{2\pi} n \sin n(\alpha+\phi)\, e^{jA\cos\alpha}\, d\alpha$$

Expanding $\sin n(\alpha+\phi)$ yields

$$= \frac{a_n n}{jA}\left\{\int_0^{2\pi} \cos n\phi \sin n\alpha\, e^{jA\cos\alpha}\, d\alpha + \int_0^{2\pi} \sin n\phi \cos n\alpha\, e^{jA\cos\alpha}\, d\alpha\right\} \quad \text{(B.5b)}$$

but $$J_n(A) = \frac{j^n}{2\pi}\int_0^{2\pi} e^{jA\cos\alpha} e^{jn\alpha}\, d\alpha$$

$$\therefore \frac{2\pi J_n(A)}{j^n} = \int_0^{2\pi} (\cos n\alpha + j \sin n\alpha) e^{jA\cos\alpha}\, d\alpha \qquad , n > 0 \qquad \text{(B.6a)}$$

$$\frac{2\pi J_{-n}(A)}{j^{-n}} = \int_0^{2\pi} (\cos n\alpha - j \sin n\alpha) e^{jA\cos\alpha}\, d\alpha \qquad , n < 0 \qquad \text{(B.6b)}$$

Summing (B.6a) and (B.6b) yields

$$\int_0^{2\pi} \cos n\alpha \, e^{jA\cos\alpha} \, d\alpha = \pi\left[\frac{J_n(A)}{j^n} + \frac{J_{-n}(A)}{j^{-n}}\right]$$

Subtracting (B.6a) and (B.6b) yields

$$\int_0^{2\pi} \sin n\alpha \, e^{jA\cos\alpha} \, d\alpha = \frac{\pi}{j}\left[\frac{J_n(A)}{j^n} - \frac{J_{-n}(A)}{j^{-n}}\right] = 0$$

Substituting these identities into (B.5b) yields

$$\boxed{I} = \frac{-a_n}{jA}\pi j^n 2n J_n(A) \sin n\phi$$

Similarily

$$\boxed{II} = \frac{b_n}{jA}\pi j^n 2n J_n(A) \cos n\phi$$

Substituting $\boxed{I}$ and $\boxed{II}$ into equation (B.5a) and applying the identity

$$\frac{2n J_n(A)}{A} = J_{n+1}(A) + J_{n-1}(A)$$

yields

$$A_\theta = B\left\{j^n \frac{\pi}{j}\left(J_{n+1}(A) + J_{n-1}(A)\right)\left[a_n \sin n\phi - b_n \cos n\phi\right]\right\}$$

Substituting the quantities for A and B yield

$$A_\theta = \frac{\mu}{4}\frac{e^{-jkr}}{r} a\cos\theta\left\{j^n \frac{1}{j}\left(J_{n+1}(k a \sin\theta) + J_{n-1}(k a \sin\theta)\right)\left[a_n \sin n\phi - b_n \cos n\phi\right]\right\} \quad \text{(B.7)}$$

The corresponding electric field component can now be determined by substituting equation (B.7) into equation (B.4a).

$$E_\theta = -j\omega\frac{\mu}{4}\frac{e^{-jkr}}{r}a\cos\theta\left\{j^n\frac{1}{j}\left(J_{n+1}(ka\sin\theta)+J_{n-1}(ka\sin\theta)\right)\left[a_n\sin n\phi - b_n\cos n\phi\right]\right\}$$

$$\therefore\ E_\theta = f_n(\theta)\left[a_n\sin n\phi - b_n\cos n\phi\right] \qquad (B.8)$$

where $$f_n(\theta) = -\frac{\omega\mu a}{4}\frac{e^{-jkr}}{r}j^n\cos\theta\left[J_{n+1}(ka\sin\theta)+J_{n-1}(ka\sin\theta)\right]$$

Solving for A_ϕ :

Let $B = \frac{\mu}{4\pi}\frac{e^{-jkr}a\cos\theta}{r}$ and $A = ka\sin\theta$, $\therefore$ equation (B.3b) becomes

$$A_\theta = B\left\{\int_0^{2\pi} a_n\cos n\phi'\cos(\phi'-\phi)e^{jA\cos(\phi'-\phi)}d\phi' + \int_0^{2\pi} b_n\sin n\phi'\cos(\phi'-\phi)e^{jA\cos(\phi'-\phi)}d\phi'\right\} \qquad (B.9)$$

$$= B\left\{\boxed{III} + \boxed{IV}\right\} \qquad (B.9a)$$

$$\boxed{III} = \int_0^{2\pi} a_n\cos n\phi'\cos(\phi'-\phi)e^{jA\cos(\phi'-\phi)}d\phi'$$

Let $u = \cos(\phi'-\phi)\, e^{jA\cos(\phi'-\phi)}$

$$du = -\sin(\phi'-\phi)\, e^{jA\cos(\phi'-\phi)} + \cos(\phi'-\phi)\, e^{jA\cos(\phi'-\phi)} \frac{d}{d\phi'} jA\cos(\phi'-\phi)\, d\phi'$$

$$dv = \cos n\phi'$$

$$v = \frac{1}{n}\sin n\phi'$$

$$\boxed{\text{III}} = -\frac{a_n}{n}\int_0^{2\pi} \sin n\phi' \left[-\sin(\phi'-\phi)\, e^{jA\cos(\phi'-\phi)} + \cos(\phi'-\phi)\, e^{jA\cos(\phi'-\phi)} \frac{d}{d\phi'} jA\cos(\phi'-\phi) \right] d\phi'$$

$$= \frac{a_n}{n}\left[\frac{\pi j^n 2n J_n(A)\cos n\phi}{jA} + \boxed{\text{V}} \right] \qquad \text{(B.10)}$$

$$\boxed{\text{V}} = \int_0^{2\pi} \sin n\phi' \cos(\phi'-\phi)\, e^{jA\cos(\phi'-\phi)} \frac{d}{d\phi'} jA\cos(\phi'-\phi) \right] d\phi'$$

But $\sin n\phi' \cos(\phi'-\phi) = \frac{1}{2}\sin[(n+1)\phi' - \phi] + \frac{1}{2}\sin[(n-1)\phi' + \phi]$

$$\therefore = \frac{1}{2}\int_0^{2\pi} \sin[(n+1)\phi' - \phi]\, e^{jA\cos(\phi'-\phi)} \frac{d}{d\phi'} jA\cos(\phi'-\phi) \right] d\phi'$$

$$+ \frac{1}{2}\int_0^{2\pi} \sin[(n-1)\phi' + \phi]\, e^{jA\cos(\phi'-\phi)} \frac{d}{d\phi'} jA\cos(\phi'-\phi) \right] d\phi'$$

$$= \boxed{\text{VI}} + \boxed{\text{VII}} \qquad \text{(B.11)}$$

$$\boxed{\text{VI}} = \frac{1}{2}\int_0^{2\pi} \sin[(n+1)\phi' - \phi]\, e^{jA\cos(\phi'-\phi)} \frac{d}{d\phi'} jA\cos(\phi'-\phi) \right] d\phi'$$

Let $u = \sin[(n+1)\phi' - \phi]$ $\qquad dv = e^{jA\cos(\phi'-\phi)} \frac{d}{d\phi'} jA\cos(\phi'-\phi)]\, d\phi'$

$du = (n+1)\cos[(n+1)\phi' - \phi]\, d\phi'$ $\qquad v = e^{jA\cos(\phi'-\phi)}$

$$\therefore \boxed{VI} = -\frac{1}{2}\int_0^{2\pi} (n+1)\cos[(n+1)\phi' - \phi]\, e^{jA\cos(\phi'-\phi)}\, d\phi'$$

Let $\alpha = \phi' - \phi \quad \Rightarrow \quad (n+1)\phi' - \phi = (n+1)\alpha + (n+1)\phi - \phi$

$\phi' = \alpha + \phi \qquad\qquad = (n+1)\alpha + n\phi$

$$\therefore = -\frac{1}{2}\int_0^{2\pi} (n+1)\cos[(n+1)\alpha + n\phi]\, e^{jA\cos\alpha}\, d\alpha$$

Expanding $\cos[(n+1)\alpha + n\phi]$ and applying the previously defined Bessel identities yields

$$\boxed{VI} = -\frac{(n+1)}{2}\pi\, 2\, J_{n+1}(A)\, j^{-(n+1)}\cos n\phi$$

Similarily

$$\boxed{VII} = -\frac{(n-1)}{2}\pi\, 2\, J_{n-1}(A)\, j^{-(n-1)}\cos n\phi$$

Substituting $\boxed{VI}$ and $\boxed{VII}$ into equation (B.11) yields

$$\boxed{V} = \pi\cos n\phi\,[-(n+1)\, J_{n+1}(A)\, j^{-(n+1)} - (n-1)\, J_{n-1}(A)\, j^{-(n-1)}]$$

Substituting $\boxed{V}$ into equation (B.10) yields

$$\boxed{\text{III}} = \frac{a_n \pi \cos n\phi}{n}\left[\frac{j^{-n}\, 2\, n\, J_n(A)}{j\, A} - (n+1)\, J_{n+1}(A)\, j^{-(n+1)} - (n-1)\, J_{n-1}(A)\, j^{-(n-1)}\right]$$

Expanding the above equation and applying the Bessel identity

$$\frac{2\, n\, J_n(A)}{A} = J_{n+1}(A) + J_{n-1}(A)$$

yields

$$\boxed{\text{III}} = \pi\, a_n \cos n\phi\, j^n \frac{1}{j}\left(J_{n+1}(A) - J_{n-1}(A)\right)$$

In a similar manner, $\boxed{\text{IV}}$ in equation (B.9a) may be determined to be

$$\boxed{\text{IV}} = \pi\, b_n \sin n\phi\, j^n \frac{1}{j}\left(J_{n+1}(A) - J_{n-1}(A)\right)$$

Substituting $\boxed{\text{III}}$ and $\boxed{\text{IV}}$ into equation (B.9a) yields

$$A_\phi = B\left[\pi\, a_n \cos n\phi\, j^n \frac{1}{j}\left(J_{n+1}(A) - J_{n-1}(A)\right) + \pi\, b_n \sin n\phi\, j^n \frac{1}{j}\left(J_{n+1}(A) - J_{n-1}(A)\right)\right]$$

Replacing B and A with their corresponding quantities reduces A_ϕ to

$$A_\phi = \frac{\mu\, a}{4}\frac{e^{-j k r}}{r}\, j^n \frac{1}{j}\left(J_{n+1}(k\, a \sin\theta) - J_{n-1}(k\, a \sin\theta)\right)\left[a_n \cos n\phi + b_n \sin n\phi\right] \tag{B.12}$$

The corresponding electric field component can now be determined by substituting equation (B.12) into equation (B.4b).

$$E_\phi = -j\omega\frac{\mu}{4}\frac{e^{-jkr}}{r}a\left\{j^n \frac{1}{j}\left(J_{n+1}(k\, a \sin\theta) - J_{n-1}(k\, a \sin\theta)\right)\left[a_n \cos n\phi + b_n \sin n\phi\right]\right\}$$

$$\therefore \quad E_\phi = g_n(\theta) \left[a_n \cos n\phi + b_n \sin n\phi \right] \tag{B.13}$$

where $$g_n(\theta) = - \frac{\omega \mu a}{4} \frac{e^{-jkr}}{r} j^n \left[J_{n+1}(k a \sin \theta) - J_{n-1} (k a \sin \theta) \right]$$

References

[1] Harrington, R.F., " *Time Harmonic Electromagnetic Fields* ", McGraw-Hill Book Company, Inc., 1961.

[2] Pucel, R. A., "*Design Considerations for Monolithic Microwave Circuits*", IEEE Transaction on Microwave Theory and Technology., vol. MTT. 29, pp. 513 - 534, June 1981.

[3] Pengelly, R.S., "*GaAs monolithic microwave circuits for phased-array applications*", IEE Proc., Vol. 127, pp. 301 - 311, August 1980.

[4] Belohoubek, E.F., "*Miniature Hybrid IC's versus MMIC's for Phased Array Radars*", Confrence Proc. Military Microwaves 1986, June 1986

[5] Wisseman, W. et al, "*GaAs Microwave Devices and Circuits with Submicron Electron-Beam Defined Features*", Proc. IEEE, pp. 667 - 675, May 1983.

[6] Douville, R. and M.A. Stubbs, "*MIC technology for Phased Arrays*", Microwave Journal, pp. 143 - 163, March 1988.

[7] McIlvenna, John F., "*Monolithic Phased Arrays for EHF Communications Terminals*", Microwave Journal, pp 143 - 163, March 1988.

[8] Potukuchi, J.R., Gupta R.K., et al, "*MMIC Modules for Active Phased-Array Applications in Communications Satellites*", Microwave System News, pp 20 - 27, vol. 18, no. 11, November 1988.

[9] Kinzel, J.A., Edward, J.B. and Daniel Ross, "*V-Band, Space-Based Phased Arrays*", Microwave Journal, pp 89 - 100, January 1987.

[10] Tang, R. and R. Brown, "*Cost Reduction Techniques for Phased Arrays*", Microwave Journal, pp 139 - 146, January 1987.

[12] Pozar, D.M. and D.H. Schaubert, "*Comparison of Architectures for Monolithic Phased Array Antennas*", pp 93 - 109, Microwave Journal, March 1986.

[13] Stutzman, Warren, L. and Gary A. Thielf, "*Antenna Theory and Design*", (Toronto: John Wiley and Sons, Inc., 1987).

[14] Mailloux, Robert, J., "*Phased Array Theory and Technology*", pp 246 - 291, Proceedings of the IEEE, Vol. 70, No. 3, March 1982.

[15] Rao, Sudhahar and Ingar Karlson, "*Low Sidelobe Design Considerations of Large Linear Array Antennas with Contiguous Subarrays*", IEEE Transactions on Antennas and Propogation, Vol. AP-35, No. 4, pp 361 - 366, April 1987.

[16] Gupta, K.C., "*Broadbanding Techniques for Microstrip Patch Antennas - A Review*", Proceedings of the 1988 Antenna Applications Symposium, University of Illinois, September 1988.

[17] Pues, H.F. and A.R. Van de Capelle, "*Wideband Impedance-Matched Microstrip Resonator Antennas*", IEE Second Inter. Conf. on antennas and Propagation, Pt. 1, pp 402 - 405, 1981.

[18] Conti, R. et al, "*The Wire Grid Microstrip Antenna*", IEEE Transactions on Antennas and Propagation, Vol. AP- 29, No. 1, pp 157 - 166, January 1981.

[19] Private Communication, Elim Chan, Department of Components and Subsytems, Communications Research Centre, Ottawa, Ontario, April 1989.

[20] Staker, M.R. et al, "*Synthesis of In-Line Parasitically Coupled Rectangular Microstrip Patch Antenna Sub-arrays*", 18th European Microwave Conference, pp 1069 - 1073, Sept. 1988.

[21] Jones, J.R., A. Henderson, and P.S. Hall, "*Microstrip Antenna Performance is Determined by Substrate Constraints*", Microwave System News, pp 73 - 84, August 1982.

[22] Cock, R.T. and C.G. Christodoulou, "*Design of a two-layer, Capacitivey Coupled, Microstrip Patch Antenna Element for Broadband Applications*", APS.URSI Meeting, IEEE A.P. Society, pp 936 - 939, 1987.

[23] Aanauden, C.K. and K.G. Nair, "*Compact broadband microstrip antennas* ", Electronics Letters, vol. 22, no. 20, pp. 1064 - 1065, 1986.

[24] Lee, R.Q. and K.F. Lee, "*Gain Enhancement of Microstrip Antennas with overlaying Parasitic Directors*", Electronics Letters, Vol. 24, No. 11, pp 656 - 658, May 1988.

[25] Carver, K.R. and J.W. Mink, "*Microstrip Antenna Technology*", IEEE Transactions on Antennas and Propagation, Vol. AP-29, No. 1, pp. 2-24, January 1981.

[26] Pozar, David, M., "*Considerations for Millimeter Wave Printed Antennas*", IEEE Transactions on Antennas and Propogations, Vol. AP-31, No. 5, September 1983.

[27] Hall, P.S., C. Wood and C. Garrett, "*Wide Bandwidth Microstrip Antennas for Circuit Integration*", Electronics Letters, Vol. 15, No. 15, pp 458 - 460, July 1979.

[28] Jackson, David, R. and Nicolaos G. Alexopoulus, "*Gain Enhancement Methods for Printed Circuit Antennas*", IEEE Transactions on Antennas and Propagation, Vol. AP-33, No. 9, pp. 976-987, September 1985.

[29] Bhattacharyya, A. and T. Tralman, "*Effects of Dielectric Superstrate on Patch Antennas*", Electronics Letters, Vol. 24, No. 6, pp 356 - 358, March 1988.

[30] Nakano, H. "*Research on Spiral and Helical Antennas at Hosei University*", IEEE Antennas andPropagation Society News letter, pp 19-27, June 1988.

[31] Bhal, I.J. and P. Bhartia, "*Microstrip Antennas*", Arlech House Inc., 1980.

[32] Kaiser, J.A., "*The Archimedean Two-Wire Spiral Antenna*", IRE Transactions on Antennas and Propogation, AP-8, pp. 313 - 323, May 1960

[33] Nakano, H. et al, "*Round Spiral Antennas on a Grounded Dielectric Substrate with a Single Surface Wave Mode*", IEEE Transactions on Antennas and Propogation, pp 692 - 695, June 1988.

[34] Nakano,H. et al, "*A Spiral Antenna Backed by a Conducting Plane Reflector*", IEEE Transactions on Antennas and Propogation, vol AP-34, No. 6, June 1986.

[35] James, J.R., P.S. Hall and C. Wood, "*Microstrip Antenna, Theory and Design*", 1981, Peter Perqrinus Ltd., The Institute of Electrical Engineers, London and New York.

[36] Walter, C.H., "*Traveling Wave Antennas*", 1965, General Publishing Company Ltd.

[37] Elliott, R.S. "*Antenna Theory and Design*" 1981 by Prentice-Hall, Inc., Englewood Cliffs, N.J.

[38] Shafai, L and K. Antoszkiewicz, "*Circular Polarized Antennas Employing Linearly Polarized Radiations*", Department of Electrical Engineering, University of Manitoba, Winnipeg, Manitoba, R3T 2N2.

[39] Wood, C., "*Curved microstrip lines as compact wideband circulary polarized antennas*", Microwaves, Optics and Acoustics, Vol. 3, No. 1, pp 5-13, January 1979.

[40] Lee, K.F., "*Principles of Antenna Theory*", 1984 by John Wiley and Sons Ltd. pg. 275.

[41] Shafai, L. and A.A. Sebak, "*Radiation Characteristics and Polarization of undulated microstrip line antennas*", IEE Proceedings, Vol. 132, Pt. H. No. 7, pp. 433 - 439, December 1985.

[42] Compton, Richard and David Ruttedge, "*PUFF, Computer Aided Design for Microwave Integrated Circuits*", 1987, California Institute of Technology, Pasedena, California, pp 12 - 13.

[43] Das, N. et al, "*Conically depressed microstrip patch antennas*", IEE Proceedings-H, Vol.. 130, Part H, No. 3, April 1983

[44] Lin, Yiyu and L. Shafai, "*Characteristics of Concentrically Shorted Circular Patch Microstrip Antennas and their comparison with annular ring data.*" Department of Electrical Engineering, University of Manitoba, Winnipeg, Manitoba, R3T 2N2.

[45] Bhattacharyya, A.K., and L. Shafai, "*Method of reducing mode-degeneracy problem in annular-ring patch antennas*", IEE Proceedings, Vol. 134, Pt.H., No.6, pp 550 - 556, December 1987.

[46] Chow, W.C., "*A Broad-Band Annular-Ring Microstrip Antenna*", IEEE Trans. on Antennas and Propogation, Vol. AP - 30, No. 5, pp 918 - 922, Sept. 1982.

[47] Balanis, Constantine A., " *Antenna Theory Analysis and Design* ", 1982 by Harper & Row, Publishers, Inc.